UNIVERSITÀ DEGLI STUDI MILANO - BICOCCA

Facoltà di Scienze MM. FF. e NN.
Dipartimento di Fisica G. Occhialini
Doctorate School in PHYSICS

GFP Photo Switchable Mutants for Intensity Modulation Imaging

Ph.D. Thesis

by

Stefano C. Daglio

Code Number: 055211

Advisor: Prof. Giuseppe Chirico

May 2012

Io mi intossico talmente a contatto del mio prossimo che ogni tanto sono costretto a ritirarmi in campagna per disintossicarmi. Se non che a quel punto, non avendo piú gente intorno, mi prende la paura che il mio odio per l'umanitá sia diminuito. Allora ritorno in cittá... e mi incazzo... Vado in campagna e mi ritiro... e mi ritiro... Mi incazzo... mi ritiro... mi incazzo... mi ritiro...
Insomma, non riesco a risolvere quella assurda contraddizione che si potrebbe chiamare mania di solitudine e di mondo.

- Giorgio Gaber [Io Se Fossi Gaber, 1985]

Because at least in prison and at least in death, you know, I wouldn't be in fuckin' Bruges...

- Ray [In Bruges, 2008]

There can't be a crisis next week. My schedule is already full.

- Henry A. Kissinger

Hurry up, before we come to our senses!

- King Julien [Madagascar 2, 2008]

Quando il cielo non bastava,
non bastava la brigata,
eri solo da incontrare,
ma tu ci sei sempre stata.

- Ligabue

Università degli Studi Milano - Bicocca

Abstract

Facoltà di Scienze MM. FF. e NN.
Dipartimento di Fisica G. Occhialini
Doctorate School in PHYSICS

GFP Photo Switchable Mutants for Intensity Modulation Imaging

Ph.D. Thesis

by Stefano C. Daglio

Photo-switchable chromophores are fluorescent inorganic dyes or proteins characterized by the tunability of their emission depending on the properties of the exciting radiation such as wavelength or intensity. The opportunities offered by this kind of markers in the field of fluorescence microscopy, range from super-resolution imaging to molecular intracellular sensing of pH, calcium or second messengers.

In this thesis I have studied the properties of two photo switchable GFP Mut2 mutants (E222Q and Mut2GQ) and their possible applications to biological fluorescence pump and probe imaging.

From a strictly biological point of view the choice of a biological marker such as GFPs is very convenient since the fluorescent label can be engineered to be naturally expressed by the cell under study. The risk of compromising or altering the cell cycle is reduced and, at the same time, labeling affect the parent as well the daughter cells. These two mutants offer the possibility to investigate the role of the proton network around the GFP chromophore (in the case of the E222Q mutant) and the external protonation (in the case of the Mut2GQ mutant) of the GFP chromophore on the photo-switching.
From the physical point of view, GFP Mut2 mutants, when excited by a less energetic pump wavelength, are characterized by long-lived non-fluorescent states whose depopulation can be triggered by irradiation with a more energetic probe beam. The first effect of the photo-induced depopulation of the long-lived state is the enhancement of the fluorescence signal due to the fact that the molecules are no more prevented to be excited to the high quantum yield singlet excited state.

I have been able not only to characterize the fluorescence enhancement ratio of the GFP-Mut2 mutants, but also the characteristics relaxation times of the population and depopulation processes of the dark state.
These parameters have a dependence on physical properties of their surroundings such as pH and viscosity, that could be exploited in imaging and sensing applications.

Basing on this characterization I reasoned that the fluorescence enhancement (called in the thesis Enhancement Ratio) and the related relaxation time (Photoswitching Time) characteristic of these GFP mutants and other photoswitchable proteins, could be the basis for a new functional imaging technique. With this new protocol for image acquisition (called Beating Mode) it is possible to acquire images in which the contrast agent is not only the fluorescence intensity, but also the Enhancement Ratio or the Photoswitching Times.

This imaging protocol can be easily extended to other photo-switchable proteins and by further characterizing their photo-switching properties as a function of pH or viscosity, it will offer the possibility to map biological functions in the samples.
Here I outline and test the algorithms to perform what I called Intensity Modulation Beating Mode Imaging. However it must be noted that in order to reach the ultimate application of this technique, namely to perform intra-cellular sensing experiments via the detection of the photoswithcing parameters, the GFP mutants should be further engineered to allow cell transfection or membrane adhesion. This molecular biology step goes beyond the aim of my thesis.

In this work, after the first introductory theoretical Chapters, I present a theoretical introduction to photo switchable GFP mutants in terms of physical and conformational properties (Chapter 3) [1].
In Chapter 4 we present the characterization of the behavior of the photo switching properties of the two mutants under study as a function of physical characteristics of the surroundings such as pH and viscosity [2]. In the same Chapter we also present a joined theoretical-simulative model in order to analyze, in terms of FCS analysis, the coupling of the fluorescence properties with the long lived dark state conformational dynamics [3].
In Chapter 5, we describe the new image acquisition protocol developed in this work and called Beating Mode, both in terms of its potentialities and limitations, with a particular interest in the rationalization of the best operative condition and the applicability to biological sample.
In Chapter 6 the applications of the Beating Mode protocol are finally outlined.

Contents

List of Figures

List of Tables

Abbreviations

ACF	**A**uto**C**orrelation **F**unction
APD	**A**valanche**P**hoto **D**iode
BD	**B**rownian **D**ynamics
BM	**B**eating **M**ode
CCD	**C**harge-**C**oupled **D**evice
CW	**C**ontinuous **W**ave
FCS	**F**luorescence **C**orrelation **S**pectroscopy
FTV	**F**luorescence **T**ime **V**ector
G3D	**3**-**D**imensional **G**aussian
GFP	**G**reen **F**luorescent **P**rotein
MC	**M**onte **C**arlo
MPE	**M**ulti-**P**hoton **E**xcitation
OL	**O**ptical-**L**abel
OPE	**O**ne-**P**hoton **E**xcitation
PD	**P**hoto **D**ynamics
PMT	**P**hoto **M**ultiplier **T**ube
PSF	**P**oint **S**pread **F**unction
QY	**Q**uantum **Y**ield
TPE	**T**wo-**P**hoton **E**xcitation
UV	**U**ltra **V**iolet

To Kira, my first love...

Part I

Theoretical Introduction

Chapter 1

The Physics Behind BioSpectroscopy

1.1 An Introduction to the Interaction Between Radiation and Matter

Let us consider, in an atom or a molecule, two electronic levels n and m, with energies E_n and E_m where $E_n < E_m$ (Figure 1.1).

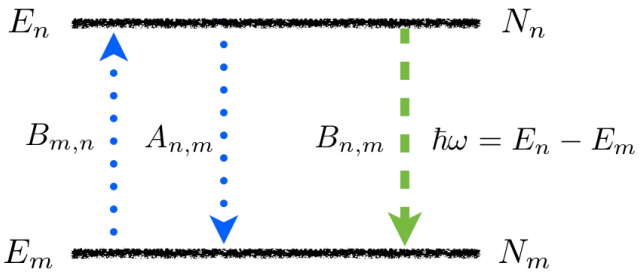

FIGURE 1.1: Energy diagram of an atomic two-level system. Energies E_m and E_n are measured with reference to some lower level

According to Einstein's theory, three different processes can take place during the interaction of light with matter:

- **Absorption** In this process one photon from the radiation field disappears and the energy is transferred to an electron as potential energy when it changes from state

E_m to E_n. The probability for an electron to undergo the absorption transition is $B_{m,n}$.

- **Spontaneous emission** As a consequence of the absorption, when in an excited state E_n, an electron in an atom has a probability A_{nm} to spontaneously fall to the lower state E_m. The loss of potential energy gives rise to the simultaneous emission of a photon with energy $\hbar\omega = E_n - E_m$. If the sample is not a crystal the direction, phase and polarization of the photon are random quantities.

- **Stimulated emission** This contribution to the light emission only occurs under the influence of an electromagnetic wave. When a photon with energy $\hbar\omega$ passes by an excited atom it may stimulate the emission of a twin photon by this atom, with a probability $B_{n,m}$. The emitted twin photon has the same energy, the same direction of propagation, the same polarization state and its associated wave has the same phase as the original inducing photon. In an elementary stimulated emission process the net optical gain is two; this is the fundamental process of every laser.

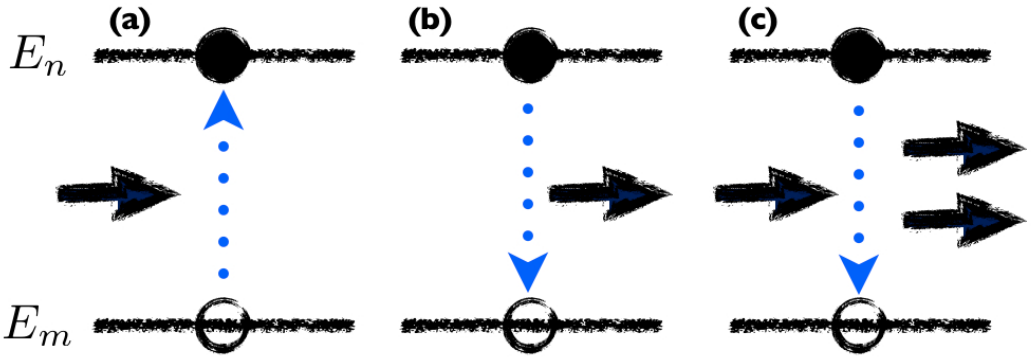

FIGURE 1.2: The three elementary electron-photon interaction processes in atoms: (**a**) absorption,(**b**) spontaneous emission,(**c**) stimulated emission

Let us now consider a set of N atoms, of which N_m are in state m and N_n in state n, and assume that this set is illuminated with a light wave of angular frequency ω with intensity $I(\omega)$ ($\hbar\omega = E_n - E_m$).

At a given temperature T, in a steady state regime, the number of absorbed photons equals the number of emitted photons (equilibrium situation for a black body). The number of photons absorbed (or emitted by stimulated emission) is proportional to the intensity of the radiation field, the number of electrons in the starting level and the probability transition $B_{m,n}$ (or $B_{n,m}$). The contribution of the spontaneous emission does not depend on the intensity but only on the number of electrons in the state n and the transition probability $A_{n,m}$.

This can be simply formalized in:

$$N_m B_{m,n} I(\omega) = N_n B_{n,m} I(\omega) + N_n A_{n,m} \tag{1.1}$$

Boltzmann's law, deduced from the statistical analysis of gases, gives the relative population on the two levels separated by an energy $\hbar\omega$ at a temperature T: $N_n/N_m = \exp(-\hbar\omega/kT)$.
When applied to 1.1 it leads to:

$$B_{m,n} I(\omega) e^{-\hbar\omega/kT} = B_{n,m} I(\omega) + A_{n,m}$$

and

$$I(\omega) = \frac{A_{n,m}}{B_{m,n} e^{-\hbar\omega/kT} - B_{n,m}} \tag{1.2}$$

This yield to the well known Planck's distribution:

$$I(\omega)\, d\omega = \frac{\hbar\omega^3\, d\omega}{\pi^2 c^2 (e^{-\hbar\omega/kT} - 1)} \tag{1.3}$$

Comparison of expression 1.2 and 1.3 shows that $B_{m,n} = B_{n,m}$: for a photon the probability to be absorbed equals the probability to be emitted by stimulation. These two effects are perfectly symmetrical; they both take place when an electromagnetic field is present around the atom.[5]

1.2 Absorption

A molecule hit by a photon carrying an energy $h\nu$ equal to the difference of energy levels in the molecular structure, is said to have absorbed the photon: the molecule is now in an excited state.
This absorption process happens in a very short time scale (10^{-15}s) so that the molecule does not undergo any alteration in its structure.

The equation that correlates the fraction of light absorbed and the concentration of the absorbing sample is known as the Beer-Lambert law:

$$A(\lambda) = \log \frac{I_0}{I} = C\epsilon(\lambda)l \tag{1.4}$$

where A is a dimensionless quantity called the absorbance or sometimes the optical density, I_0 is the intensity of the incident radiation while I is the intensity of the transmitted radiation, C is the molar concentration of the absorber and ϵ its molar extinction coefficient. The last one is defined to be proportional to the one photon absorption cross section of the molecule σ through the following equation:

$$\epsilon = \frac{\sigma N_0}{2.303} = \frac{\pi r^2 P N_0}{2.303} \tag{1.5}$$

$$\epsilon = M^{-1}cm^{-1} = \left(\frac{mol}{l}\right)^{-1} cm^{-1} = \frac{cm^2}{mol} \tag{1.6}$$

where P is the probability for the light impinging on the molecule to be absorbed, r the radius of the molecule and N_0 the Avogadro number.

If the sample is homogeneously constituted by non-interacting molecules, it can be stated that the Beer-Lambert law describes the decay due to the absorption of the radiation propagated through the sample.

One is usually interested in the absorption spectrum of the molecules, that represent the probability for a photon of variable energy to be absorbed by the molecules. It is possible to distinguish three different fundamental kinds of spectrum:

- *Electronic spectrum*: corresponding to the electronic state transition. This absorption process involves energies corresponding to a gap, in term of wavelength, between 200 and 900nm.
- *Vibrational spectrum*: corresponding to the transition between vibrational level inside the same electronic level: these are transitions triggered by IR radiation (700/800nm-2/5μm).

- *Rotational spectrum*: corresponding to transition between rotational state inside the same vibrational state: the energies involved correspond to the wavelength of the microwave($\approx 1mm$-$\approx 1m$).

1.3 Spontaneous Emission and Fluorescence

Once an absorption process occurs one electron of the molecule is on an excited electronic level in the energy level structure. The electron will return to the ground state through processes that can be radiative (photons emission) or non-radiative.
While the time scale characteristic of an absorption process is too short ($10^{-15}s$) to allow conformational changes in the molecular structure during the process, for the de-excitation process ($10^{-9}s - 10^{-3}s$) this does not hold true. The alterations in the molecular structure that take place while the electron is on the excited level, affect the de-excitation process.

In Figure 1.3 a Jablonski energy diagram shows all the possible processes that happen as a consequence of the absorption of a photon by a molecule.

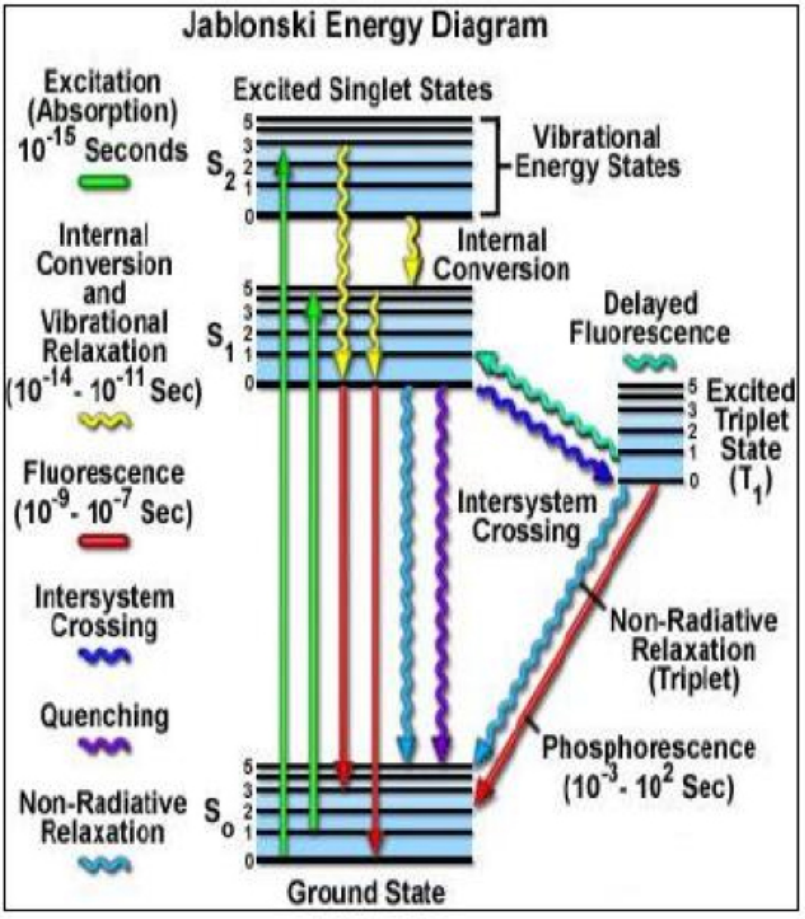

FIGURE 1.3: Jablonsky Energy Diagram for a generic molecule

S_0 and S_1 indicate respectively the ground and the first excited state of the molecule. Both of them are split in different vibrational levels, each of these splits up in several

rotational levels.
At room temperature, the energetic separation between S_0 and S_1 is some 80 Kcal/mol, while it drops to 10 Kcal/mol for the vibrational levels and to 0.6 Kcal/mol for the rotational ones. Since $k_BT \approx 0.6$ Kcal/mol, at room temperature a molecule is in its electronic and vibrational ground state while various rotational levels can be populated.

1.3.1 De-excitation Processes

Once the absorption process occurs, the electron involved in the interaction is found on one of the rotovibrational levels of the electronic level S_1. In a relatively short amount of time ($\approx 10^{-12}$sec) there is a relaxation, due to the conformational changes both in the excited molecule and in the ones nearby, that make the electron fall to the vibrational ground state of S_1. This process is called *Internal Conversion* and always takes place after an absorption, no matter how the molecule relaxes to S_0.

After the first internal conversion various de-excitation processes can participate or compete for the relaxation of the molecular structure. The first division we can make is between the non radiative and the radiative processes.

1.3.1.1 Non-Radiative Processes

These are the processes that bring the molecular structure back to the ground state without loss of energy due to the emission of photons. Rather than energy loss through photon emissions these processes occur through interaction with environment around the excited molecule.
The principal non-radiative processes are:

- *Quenching*: it is the bimolecular process of de-excitation of the chromophore that happens through collisions, or non-fluorescent aggregate formations, with molecules (the *quenchers*) present in the local environment. The most efficient quenchers are O_2 and I^-. The de-excitation rate for the quenching depends on the nature and the concentration of the molecule that generates the process.

- *Intersystem Crossing*: the process involving a non-radiative transition between the singlet state S_0 and the triplet state T_1. When this transition happens it causes a spin reverse in the excited electron. After an intersystem crossing, the molecule can return to its relaxed structure through another internal conversion or a phosphorescent emission.

- *Energy Transfer*: an event in which there is an energy swap between two chromophores distant no more than some tens Angstrom. The excited chromophore (Donor [D]) transfers energy to the other molecule (Acceptor [A]) This process occurs because of the dipole interaction of the two molecules and only if there is a partial overlap between the emission spectrum of the donor and the absorption spectrum of the acceptor.
- *Internal Conversion*: the same process that happens right after the absorption. It is highly dependent on the temperature of the sample: the more we raise the temperature the more probable internal conversion will be.

1.3.1.2 Radiative Processes

These are processes in which the excited molecule loses energy by the spontaneous emission of photons.
There are two of them: Fluorescence and Phosphorescence.

Fluorescence Fluorescence is the process in which the excited molecule, immediately after the first internal conversion, spontaneously emits a photon of energy $h\nu$ equal to the energy separation of S_0 and S_1 while the excited electron fall back to S_0.
Because the electron can fall in any of the roto-vibrational levels of S_0, there will be a spread in the wavelength of the emitted light.
The fluorescence emission happens on a time scale that ranges from a few to several nanoseconds (10^{-9}sec) Different kinds of chromophores are characterized by different time scales in this range.

Phosphorescence The phosphorescent emission of photons happens as a consequence of an intersystem crossing process. The electron fall down from T_1 to S_0 while a photon of energy $h\nu = \Delta E(T_1, S_0)$ is emitted.
The main difference between phosphorescence and fluorescence is the decay time of the emission; whereas the fluorescence happens within nanoseconds, a phosphorescent decay can range from microseconds (10^{-3}sec) to several hours. This happens because of the reverse spin of the electron from the intersystem crossing transition. As a result, the energy can become trapped in the triplet state with only quantum mechanically "forbidden" transitions available to return to the lower energy state. These transitions, although "forbidden", will still occur but are kinetically unfavored and thus progress at a significantly slower rate.

1.3.2 Characteristics of Fluorescence Emission

All of the processes considered above compete for the relaxation of the molecular structure of the excited chromophore to the ground state S_0.
Fluorescent emission will be more intense the more limited the other competitive processes are.

The principal characteristic of fluorescence emission are:

1. *Stokes' Shift*: looking at the Jablonsky diagram (Figure 1.3) it appears evident that between absorption and fluorescence emission there is a loss of energy due both to the relaxation to a lower vibrational state of S_1 and to the relaxation from the higher vibrational level of S_0 more often involved in the transition. As a result, emission of light takes place at lower energy (higher wavelength) with respect to excitation. This phenomenon was first observed by Sir George Gabriel Stokes in 1852 (Stokes[6]).

2. *Kasha's Rule*[7]: the emission spectra are independent from the excitation wavelength; after absorption the fluorophores rapidly relax to the lowest vibrational state of S_1 from which any transition to S_0 starts.

3. *Mirror's Rule*: a rule of thumb stating that absorption and emission spectrum are symmetric because they involve the same levels (see Figure 1.4).

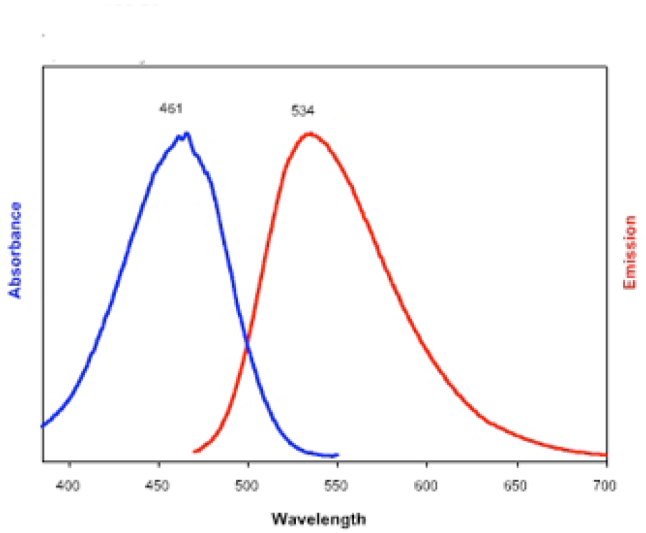

FIGURE 1.4: Example of absorption and emission spectrum for a fluorescent sample

In fluorescence spectroscopy there are two main parameters worth noting: the mean decay time τ and the quantum yield ϕ. Both of them will be defined in the next section.

1.3.3 Mathematical Description of the Fluorescence Process

From a mathematical stand point, the joint process of excitation and return to the ground state between two levels S_0 and S_1 of a molecular structure, can be described by the following system of equations:

$$\begin{cases} \frac{dS_1}{dt} = -K_T \cdot S_1 + K_{EXC} \cdot S_0 \\ \frac{dS_0}{dt} = +K_T \cdot S_1 - K_{EXC} \cdot S_0 \end{cases} \tag{1.7}$$

K_T is a constant taking in consideration the rates of all the possible relaxation processes; meaning:

$$K_T = K_F + K_{I.C.} + K_{IS} + K_Q \tag{1.8}$$

where K_F, $K_{I.C.}$, K_{IS}, K_Q are respectively the rates for the processes of fluorescence, internal conversion, intersystem crossing and quenching[1].

The pure de-excitation process, triggered by a previous event of excitation of the sample, is controlled, once the excitation light is turn off, by the following differential equation:

$$\frac{dS_1}{dt} = -(K_F + K_{I.C.} + K_{IS} + K_Q) \cdot S_1 \tag{1.9}$$

This equation has the following solution:

$$S_1(t) = S_1(0) \cdot e^{-\frac{t}{\tau_T}} + \widetilde{S_1} \tag{1.10}$$

where $\tau_T = (K_F + K_{I.C.} + K_{IS} + K_Q)^{-1}$ is the **decay time** and $\widetilde{S_1}$ is the population of the state S_1 due to the thermal energy of the sample at the laboratory temperature.

The ratio between the radiative decay time $\tau_F = 1/K_F$ and the total decay time τ_T (from all decay processes) defines the **quantum yield** of the radiative relaxation process:

$$\phi_F = \frac{\tau_T}{\tau_F} \tag{1.11}$$

Quantum yield depends both on the molecular structure of the fluorophore and on the type of excitation technique used, and can also be physically understood as the ratio between the number of emitted photons and the number of the absorbed ones.

[1] The rate for the phosphorescent process can be disregarded for the majority of the dyes.

Chapter 2

Experimental Basis

In this chapter will be given a brief introduction to optical microscopy particularly focused on single-photon excitation and of the Fluorescence Correlation technique (FCS) widely used to obtain information of the mechanical and photo dynamical characteristics of the fluorescent dyes.

2.1 Brief Introduction to Optical Fluorescence Microscopy

Optical microscopy is the technique that allows microscopic investigation of samples using electro-magnetic radiation in the visible range of wavelength.
Light microscopy is unique in its ability to allow the examination of biological specimens in a hydrated state, in living samples or under conditions that closely approximate the living state.
Fluorescence Microscopy adds to the fundamental power of light microscopy the ability to examine the spatial distribution of specific cellular components. The availability of pH-dependent fluorescent proteins, as well as biologically targeting chemical dyes, allow details of cellular organization and functions to be probed and mapped with a precision previously unknown Agard et al. [8].

2.1.1 Principles and Various Excitation Setup

In optical fluorescence microscopy, a light source (usually a LASER), tuned on the chromophore excitation wavelength is focused on the sample via a microscope objective. If the sample contains, in the microscope focal spot, a concentration of the fluorophore, a florescent emission is obtained (see Section 1.3), with an intensity proportional both to the intensity of the excitation light and the concentration of the chromophore itself.

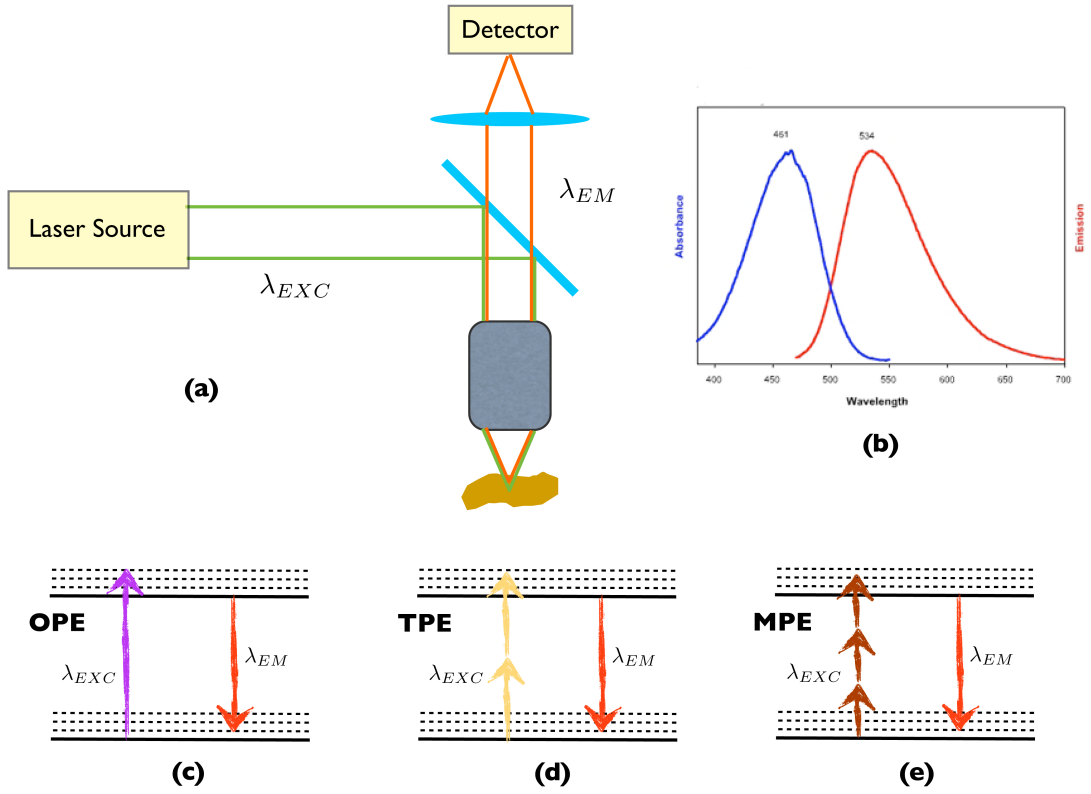

FIGURE 2.1: **(a)**: Schematic of a fluorescence microscope. A dichroic mirror permits the separation of the excitation and emission wavelength, thus allowing the detection of the fluorescence signal; **(b)**: exemplification of Absorption and Emission Spectra for a general chromophore. Intuitively the chosen excitation wavelength should be as close al possible to the peak of the blue line and the fluorescence signal should be detected near the peak of the red line; Jablonsky Diagram for: **(c)** One Photon Excitation, **(d)** Two-Photon Excitation, **(e)** Multi-Photon Excitation.

From a quantum mechanics point of view what happens is, as described in Section 1.2, the excitation of the chromophore molecule to an excited singlet state triggered by the absorption of photons from the light source. The de-excitation of the molecule following the absorption process may follow various routes (see Section 1.3), one of those is the spontaneous emission of a single photon with wavelength *redder* than the excitation one: this phenomenon, known as *Stoke's Shift*, is fully described in Section 1.3.2 (Figure 2.1**(b)**)[6]. This difference in the excitation and fluorescence emission wavelength allows a separation, via a dichroic mirror (Figure 2.1**(a)**), of the sample signal that can be, therefore, directed to a photodetector such as a PMD or an APD, depending of the experimental setup and necessity.

The energy gap between the S_0 and S_1 state (corresponding to the E_m and E_n states in Figure1.1) can be filled in various ways. In 1939, Maria Goppert Mayer theorized the actual possibility for a molecule to absorb simultaneously more than one photon.

The limitation, of course, is that the absorption of multiple photons has to occurs *simultaneously* ($\approx 10^{-16}$), i.e. the two, or more, photons have to occupy the molecule's volume at the same time. This, of course, requires an extremely high photon spatial density ($0.1 - 10$ MW/cm^2) in the excitation light beam (see Diaspro et al.[9]). The development and commercialization of mode locked pulsed lasers, availing higher and higher power to be focused on the sample, opens the way to new excitation modalities [10], Denk et al. 1990, [11].

In particular we can differentiate:

OPE The standard One-Photon Excitation (Figure 2.1**(c)**) is the simplest and first excitation mode. A single photon is absorbed and a single is emitted. The main disadvantage of this technique is a strong limitation in the optical sectioning particularly in the z axis (as it will be shown in the following Sections); this has the holdback of a higher impact of the photobleaching and photo toxicity of the exciting beam in the sample

TPE In Two-Photon Excitation (Figure 2.1**(d)**) even if the average power is higher the photobleaching is less dangerous on the sample, partly because of the better confinement of the focal spot [12], [13], [14] [15], and partly thanks to the lower dangerousness or IR light radiation [10], [9]. Moreover another advantage is the effect of spectra broadening for all the chromophores: the same IR radiation can be used to excite different dyes at the same time. In this way it is possible to obtain an higher information-density picture of the sample simply exciting, with a single laser beam, fluorophores, emitting at different wavelength, labeling various zone of the sample. See Bestvater et al. 2002, [16].

MPE Multi-Photon Excitation (Figure 2.1**(e)**) can be suitable for extra *in-deep* microscopy on *in-vivo* biological, or necessary to excite chromophore whose fluorescence absorption spectra lies in the UV, deep UV range. See Masters et al. Masters et al., [17], [18] and [19]

Of course, once a chromophore is chosen, no matter the excitation technique, the fluorescence wavelength is always the same

2.1.2 Limitation of the Resolution: PSF

From the classical physics, it's known that it is possible to resolve objects whose dimensions are higher than the wavelength of the radiation used for the detection. The same principle, of course, holds for optical microscopy: in this case the limit in the resolution of a optical setup is formalized by the calculation of the PSF .

Point Spread Function The **Point Spread Function (PSF)** describes the response of an imaging system to a point source or point object. PSF is an intrinsic characteristic of any focused optical system and comes out from the convolution of the contribution of every single lens: being the basic elements, the contribute of a single convergent lens also known as the *Airy Function*.
The PSF represents the image (i.e. the intensity distribution), in the spatial domain, of the electromagnetic radiation emitted by a point source. The degree of spreading (blurring) of this point object is a measure for the quality of an imaging system[1]. In optical microscopy the PSF is measurable, acquiring images of a under-solved chromophore, *fluorescent beads*[2], through the optical setup to be characterized.

In fluorescence microscopy the image formation is a linear process: the imaging of two objects will be the superposition of the images of the two objects as observed alone. For this reason, the PSF can be considered the basic plug on which the image is built: in the acquisition of N point objects, the resulting image will be composed by the sum of N PSF-shaped, non interacting, contributes.

More generally, the image of any object can be constructed by dividing the object itself in sub-risolved area each with a defined intensity[3] and by summing all the intensity-normalized PSF contributes.

Therefore, defined $I(x, y)$ e $O(x, y)$ the intensity in the image-space and in the object space respectively, we can write for a generic point (x_0, y_0) the relation:

$$I(x_0, y_0) = \int\int O(x', y')PSF(x_0 - x', y_0 - y')dx'dy' \tag{2.1}$$

meaning

$$I(x, y) = O(x, y) \otimes PSF(x, y) \tag{2.2}$$

[1] The PSF of a microscope or of a more complex optical setup represent in fact the resolution power of the microscope or optical setup itself

[2] For the sake of simplicity in this kind of measurements, 100μm beads incapsulating an high chromophores concentration are usually employed.

[3] representing its actual luminosity

From a mathematical point of view what's done here is a *convolution* between the real object and the PSF of the optical system used for the imaging process Hecht 1998 (see Figure 2.2).

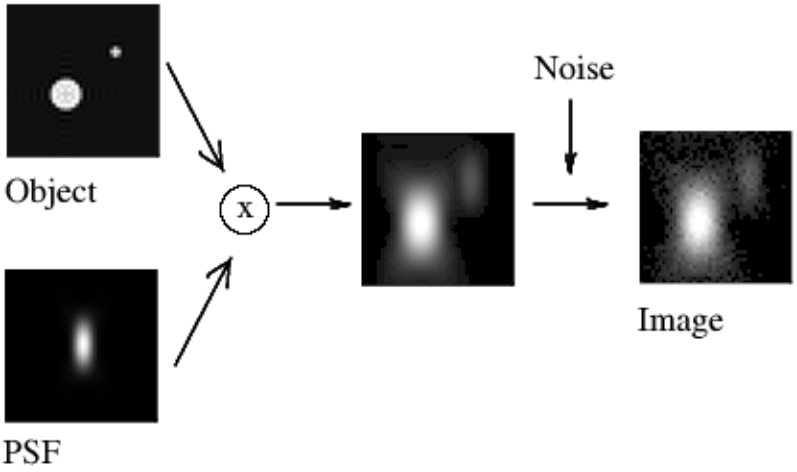

FIGURE 2.2: The relationship between an object, f, and its image, k, lays on the convolution with the optical setup PSF, h: $k = f \star h$. Actually, in the real cases, the photon noise must be taken into account, so the equation stating the relationship is:
$$k = f \star h + \epsilon$$

For application in microscopy it is consequently possible, by knowing the PSF of the optical setup, to deconvolute the image in order to obtain the real shape and dimension of the observed object.

Airy Patterns and Airy Disc As stated in the previous Paragraph the basic element in the composition of the PSF of a complex optical setup is described by the *Airy Patterns*, cylindrical symmetric functions that represents the PSF of a single convergent lens. These functions are the results of the Fraunhofer diffraction via a circular hole: in the case of a perfect optical system the patterns are represented by a central maximum intensity peak enclosed by secondary peaks parted by zero intensity circle (see Figure 2.3).
With the term *Airy Disc*, we refer to the region of the *Airy Patterns* restrained by the first minimum, representing the 0^{th}-order peak that integrates the 84% of all the intensity distribution of the Patterns.

In a microscope general case, using a light with wavelength λ, the intensity distribution, in the focal plane, for an objective with aperture number

$$NA = sin\alpha$$

is described by the relation:

$$I(u,v) = 2\left|\int_0^1 J_0(v,\rho)e^{iu\rho^2/2}\rho d\rho\right|^2 \tag{2.3}$$

where $u = 4k\sin^2(\alpha/2)z$ and $v = k\sin(\alpha)r$, whereas J_0 is the 0^{th}-order Bessel function. The argument of this function is extremely important since it determines the dimensions of the Airy Disc on the objective focal plane; it depends by the wave-number $k = 2\pi/\lambda$ and the aperture number of the objective $N.A.$ ($\approx \sin\alpha$). In particular the greater $N.A.$ is, the more reduced the Airy Disc dimension will be, the better will be the focusing of the objective and hence its resolution power.

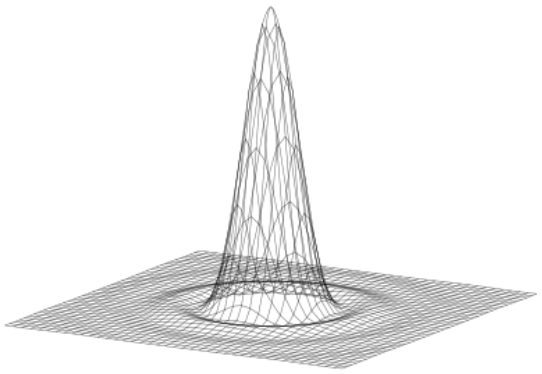

FIGURE 2.3: Airy function

2.1.2.1 Resolution of an Optical System

As mentioned before, the resolution power of a microscope depends on the dimensional parameters of its PSF.
If we consider, as an example, the image of two object as acquired by a simple convergent lens, from the principle of linearity in the image acquisition process, we obtain, as a resulting image, the sum of the two object's Airy Disc. The characteristics of the image is of course dependent on the distance between the two objects, translated in the distance between the two intensity peaks. If the objects are *sufficiently* separated the intensity variation between the two peaks is maximized: moving from a peak to another we encounter a zero-intensity space. When the distance between the objects reduces the intensity distribution begin to overlap, until the two object cannot be distinguished any longer.
From this example we get two important consideration:

- We need to define a criterium in terms of intensity distribution overlap that allows us to tell two separated resoluble objects and two undistinguished ones.
- As already mentioned the shape factor of the Airy Disk is key in the PSF characteristics: assuming the criterium is kept constant, an optical system with a thinner PSF will be able to resolve closer objects.

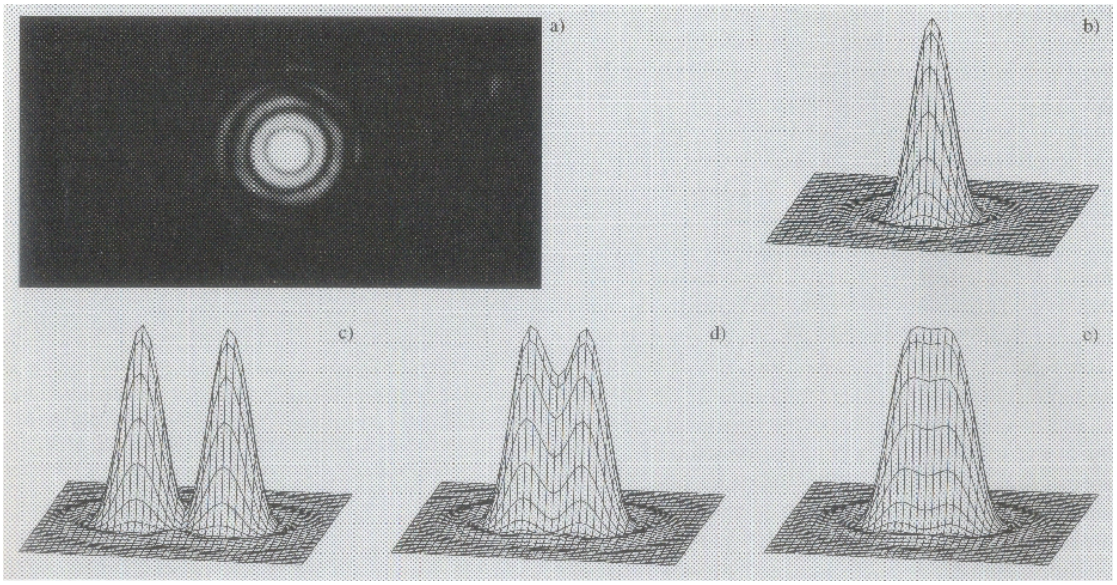

FIGURE 2.4: Rayleigh's criterium in resolution limits: image of a point object **(a)** and it contour plot **(b)**. In **(c)** two separate and resolved point object, whereas in **(d)** the image of two point objects at the limit of their resolution and in **(e)** two unresolved point objects.

Rayleigh's Criterium Once we define the resolution limit as the minimum distance between two objects at which we can distinguish one from the other, it is necessary to define a criterium able to formally put a threshold between the resolved and the undistinguished situations.

The **Rayleigh's Criterium** states that two point objects are resolved when one of the Airy Disc minimum is aligned to the maximum of the other Disc. Thinking in terms of *contrast*[4] the resolution limit is the distance at which the contrast is 26,4%.

Lateral and Axial Resolution Taking into account the previous argumentation, the definition of the *lateral resolution*[5] is the distance between the central maximum

[4]defined as the ratio between the maximum intensity of the brightest of the two object and the minimum found between the objects.

[5]the resolution on the focal plane

and the first minimum of the Airy Disc. For a conventional fluorescence microscopy, the theoretical limit for this distance is given by [15]:

$$r_{xy} = \frac{1,22\lambda_{em}}{2NA} \approx \frac{0,6\lambda_{em}}{NA} \tag{2.4}$$

In theory then, this equation allows the calculation of the resolution power of any microscope, granting a good contrast. In the real scenario though, the measurement of the intensity minimum makes experimentally complicated the application of this criterium. For this reason it is more common the measurements of FWHM (Full Width at Half Maximum) in order to measure the PSF of a microscope. In OPE microscopy, the output values of the FWHM calculation criterium are approximately 17% smaller than the value calculated by means of the Rayleigh's Criterium.

For TPE microscopy, the FWHM of the PSF is, on the opposite, larger of 15% [15]:

$$r_{xy,two-photon} \approx \frac{0,7\lambda_{em}}{NA} \tag{2.5}$$

.

In the general case then it is possible to state that the **lateral** resolution is directly proportional to the wavelength and inversely proportional to the objective's aperture number.

For point objects is of course possible to apply the same principles to calculate the *axial resolution*[6]. For a standard confocal fluorescence microscope this value is given by the relation:

$$r_z = \frac{2\lambda_{em}n}{(NA)^2} \tag{2.6}$$

whereas for two photon microscopy we have:

$$r_{z,two-photon} \approx \frac{2.3\lambda_{em}n}{(NA)^2} \tag{2.7}$$

. In conclusion, the **axial** resolution is inversely proportional to the objective's aperture number squared.

[6] the resolution along the axis perpendicular to the focal plane.

2.1.3 OPE and Confocal Setup

Confocal microscopy is an optical imaging technique used to increase optical resolution and contrast of an optical microscope, by using a spatial pinhole to eliminate out-of-focus light in thick specimens Pawley and Masters 2008 [21].
This technique enables the reconstruction of three-dimensional structures from the obtained images. This technique has gained popularity in the scientific and industrial communities and typical applications are in life sciences, semiconductor inspection and materials science.

Confocal point sensor principle from Minsky's patent The principle of confocal imaging was patented in 1957 by Marvin Minsky[7] and aims to overcome some limitations of traditional wide-field fluorescence microscopes. In a conventional[8] fluorescence microscope, the entire specimen is flooded evenly with light from a light source. All parts of the specimen in the optical path are excited at the same time and the resulting fluorescence is detected by the microscope's photodetector or camera including a large unfocused background part. In contrast, a confocal microscope uses two important improvement:

- **Point Illumination**: the excitation light is focused on the sample by a microscope objective. In this way the sample is excited by an illumination profile that can be, at the first order, described as a 3D-Gaussian profile $\rho(x, y, z) = A \exp\left((x^2 + y^2)/2\omega_0^2\right) \exp z^2/2z_0^2$. In the case of OPE $\omega_0 \approx \lambda NA/2$ whereas $z_0 \approx 5 \times \omega_0$, so the illumination confinement in the axial direction is very poor, spreading away form the focal plane. This of course is a problem since the fluorescence signal arising from the sample is a convolution between the PSF and the illumination profile, so in a setup like that, the good resolution in the $x - y$ direction is strongly penalized by all the out-of-focus fluorescence contributes.
- **Pinhole**: in order to solve this last problem a pinhole is positioned before the detection device, in the focal point of the collection lens (see Figure 2.5). In this way it is possible to filtrate the out of focus contributes that are focused by the lens at a distance from the focal point proportional to the depth in the sample it came from (see Figure 2.5).

However, since much of the light from sample fluorescence is blocked at the pinhole, this method can and does increase the resolution but at the cost of decreased signal intensity:

[7] Patent filed in 1957 and granted 1961. *US 3013467*
[8] i.e., wide-field

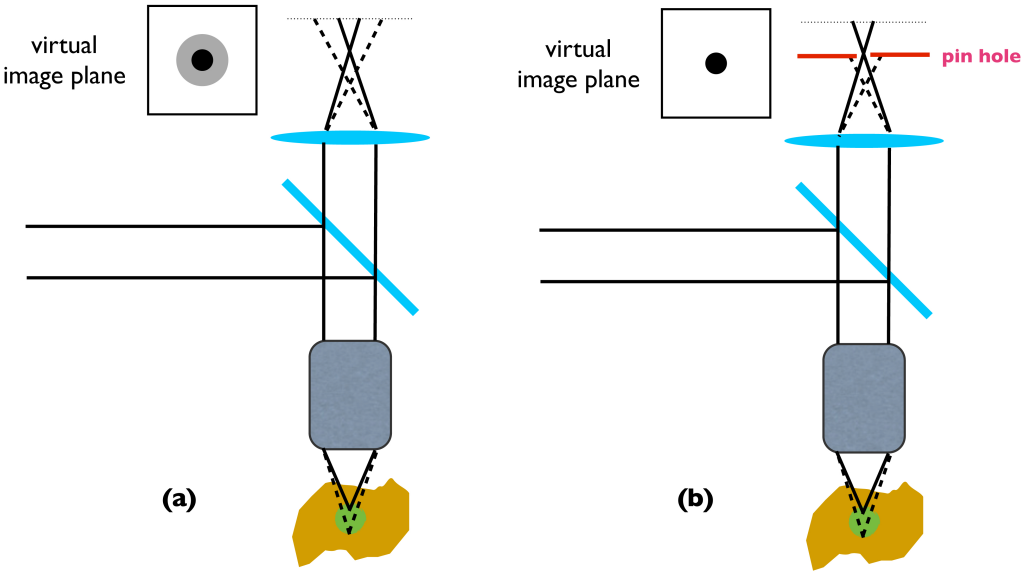

FIGURE 2.5: Confocal microscopy basics: in **(a)** the out of focus fluorescence contributes arrive to the detector causing a lowering of the image quality, whereas in **(b)** a pin-hole stops this contributes and only the light arising from the focal plane hits the detector.

longer exposures are so often required. Furthermore, the point spread function of the pinhole is an ellipsoid, several times as long as it is wide. This limits the axial resolution of the microscope.

As only one point in the sample is illuminated at a time, 2D or 3D imaging requires scanning over a regular raster[9] in the specimen. The achievable thickness of the focal plane is defined mostly by the wavelength of the used light divided by the numerical aperture of the objective lens, but also by the optical properties of the sample (see Figure 2.6).

[9] i.e. a rectangular pattern of parallel scanning lines

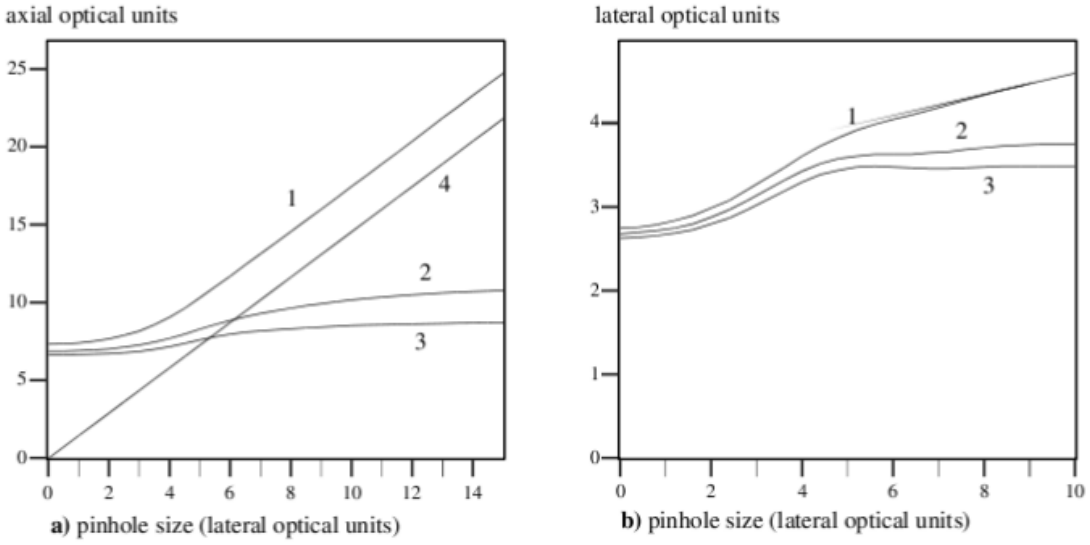

FIGURE 2.6: FWHM as a function of the pinhole radius in the case of a plane (curve 1), line (curve 2) and point (curve 3) objects. **(a)**: axial resolution (horizontally oriented objects), curve 4: axial FWHM for horizontal planes as calculated from geometrical optics. **(b)**: lateral FWHM (vertical printed objects).

2.2 Fluorescence Correlation Spectroscopy

Fluorescence Correlation Spectroscopy is an analysis method that allows the measurement of molecular properties by studying the dynamics of spontaneous fluorescence fluctuations, due to microscopic concentration fluctuations of the different photoactive state. The fluctuations may be due to different physical phenomena, like: rotational and translational diffusion, directional flow, photodynamics, photobleaching and chemical reactions occurring in the solution. In order to derive physical parameters from these fluctuations, a statistical analysis is required. In FCS, the analysis performed is a correlative one giving direct informations on, for example, diffusion time, bound/free ratio of molecules, triplet life-time and triplet fraction. The correlation function also carry important indirect informations about parameters like concentration, binding constants and on/off constants of the photoactive species in solution. In order for the fluctuation to be significant the number of average observed molecules have to be small. A small molecule number is usually obtained by a small volume of observation generated by a Gaussian laser beam on a confocal microscopy setup (see Section 2.1.3). The pin-hole guaranties the high signal-to-noise ratio necessary to perform the measurements. The principle theory behind the FCS has been derived in the early 70s by Magde et al. [22] and Ehrenberg and Rigler [23].

2.2.1 The Correlation Function

The correlation function is a synthetic way to express the correlation grades between two dynamic properties along a time period. Lets begin considering a property A of an open system which depends for example on the particles positions and the number of particles in the system (which is actually the case of fluorescence intensity in FCS). As the particles undergo motions, the positions and the number of the particles will change in time and so will do the property A. The mean value of A, if the system is at equilibrium , will be a temporal average:

$$\bar{A}(t_0, T) = \frac{1}{T} \int_{t_0}^{t_0+t} A(t)\, dt \tag{2.8}$$

Where t_0 is the instant in which the measurement of A begin and T is the measurement period. If the property A is stationary and T is long in respect of the fluctuation time of A, then

$$\langle A \rangle = \lim_{T\to\infty} \frac{1}{T} \int_0^T A(t)\, dt \tag{2.9}$$

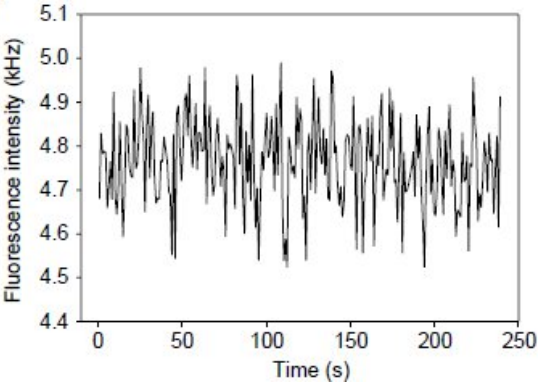

FIGURE 2.7: Fluctuating property $A(t)$

Being the signal $A(t)$ (reported in Figure 2.7) fluctuating, $A(t) \neq A(t+\tau)$. Yet, if τ is short compared to the characteristic fluctuation time of A, $A(t+\tau)$ will approach $A(t)$. For growing τ the probability for $A(t+\tau)$ to be considerably different from $A(t)$ will increase. So we can say that for short τ, $A(t+\tau)$ is correlated with $A(t)$ and that the correlation is lost at long τ. A quantitative expression for this correlation is given by the autocorrelation of the property A defined by:

$$\langle A(0)A(\tau) \rangle = \lim_{T\to\infty} \frac{1}{T} \int_0^T A(t)A(t+\tau)\, dt \tag{2.10}$$

If we now discretize the time in intervals of length Δt, and express $t = j\Delta t$, $\tau = n\Delta t$, $T = N\Delta t$ and $t + \tau = (j + n)\Delta t$; if A is almost constant during the interval Δt the expression above can be approximated by:

$$\langle A \rangle \approx \lim_{N\to\infty} \frac{1}{N} \sum_{j=1}^{N} A_j \tag{2.11}$$

and

$$\langle A(0)A(\tau) \rangle \approx \lim_{N\to\infty} \frac{1}{N} \sum_{j=1}^{N} A_j A_{j+n} \tag{2.12}$$

Where A_j is the value of $A(t)$ at the beginning of the j^{th} time interval.
Now if we consider $\langle A(0)A(0) \rangle$ the sum reduces to $\sum_{j=1}^{N} AjAj = \sum_{j=1}^{N} A_j^2$. From the Schwartz inequality follows that:

$$\sum_{j=1}^{N} A_j^2 \geq \sum_{j=1}^{N} A_j A_{j+n} \tag{2.13}$$

or alternatively

$$\langle A^2(0) \rangle \geq \langle A(0)A(\tau) \rangle \tag{2.14}$$

This means that the autocorrelation function may either remain constant (which is what happens if A is a constant of motion), or decay from a maximum initial value. So, calculating the autocorrelation function of a property A being non-constant and non-periodic, for τs long enough compared to the characteristic time of a fluctuation of A, $A(t)$ and $A(t + \tau)$ should be completely uncorrelated, so:

$$\lim_{\tau\to\infty} \langle A(0)A(\tau) \rangle = \langle A(0) \rangle \langle A(\tau) \rangle = \langle A \rangle \tag{2.15}$$

So the autocorrelation function decays from $\langle A^2 \rangle$ to $\langle A \rangle^2$ at increasing τ. In a lot of cases the decay is exponential, and so:

$$\langle A(0)A(\tau) \rangle = \langle A \rangle^2 + [\langle A^2 \rangle - \langle A \rangle^2] e^{-t/\tau_R} \tag{2.16}$$

where τ_R is called relaxation time or correlation time of the property A. If we now define the instantaneous deviation from the averaged value:

$$\delta A(t) \equiv A(t) - \langle A \rangle \tag{2.17}$$

It is easy to show that:

$$\langle \delta A(0)\delta A(\tau)\rangle = \langle A(0)A(\tau)\rangle - \langle A\rangle^2\langle \delta A^2\rangle = \langle \delta A(0)\delta A(\tau)\rangle = [\langle A^2\rangle - \langle A\rangle^2] \tag{2.18}$$

So that

$$\langle \delta A(0)\delta A(\tau)\rangle = \langle \delta A^2\rangle e^{-t/\tau_R} \tag{2.19}$$

As can be seen from Equation 2.19, the fluctuation autocorrelation function has a simpler functional form compared to the signal autocorrelation function, having erased the temporal invariant $\langle A\rangle^2$. Not every fluctuation has an exponential decay (such as the one in Figure 2.8), to have a parameter that characterize the correlation life-time, a time τ_C has to be defined.

$$\tau_C \equiv \int_0^\infty \frac{\langle \delta A(0)\delta A(\tau)\rangle}{\langle \delta A^2\rangle} d\tau \tag{2.20}$$

For an exponential decay $\tau_C = \tau_R$, in general the correlation time will be a complicate function of the process that contributes to the decay of δA.

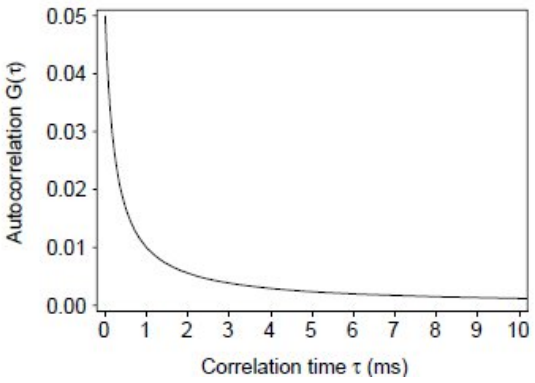

FIGURE 2.8: Exponential decay of a generic autocorrelation function

2.2.2 Operating Principle

In order to provide a qualitative explanation of FCS principles, let's consider the small confocal volume of observation filled with a laser light of appropriate wavelength to excite the chromophore (Figure 2.9). At a defined instant t_0 the fluorescent molecules, present in the volume, will be excited by the laser light and emit a fluorescence signal[10]. During the recording time of the fluorescence signal, the signal itself will undergo fluctuation due

[10] in this contest, of course, the definition of instant is of a time interval long enough compared with the spontaneous emission dynamics of the chromophore, i.e. 10^{-9}sec.

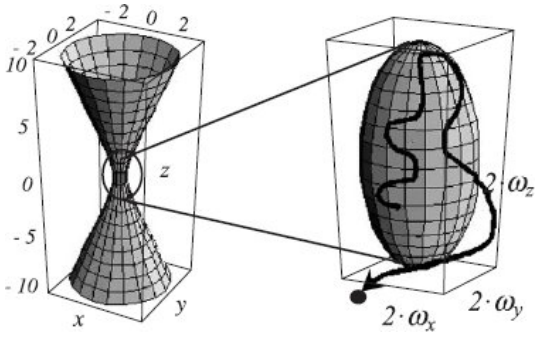

FIGURE 2.9: Detection volume (taken from CITAZIONE NUMERO DUE DI BANTERLE

to the entrance in- or the exit from the observed volume of various fluorescent molecules. In first approximation this dynamics is only due to the brownian motion[11].
The permanence time inside the observation volume, as the number of emitted photons, will depend on the random path of any single molecule and will contribute to the signal fluctuation. Averaging these on various molecular path and along a fairly long time, it is easy to understand that both the averaged permanence time and the average number of emitted photons depend on the diffusion coefficient D of the chromophore in the solution. So, the fluctuation in time δI (due to the single molecules behavior) will be distributed around a mean signal $\langle I \rangle$ (due to the ensemble behavior of the system and proportional to macroscopic constant).

The randomized behavior of the single molecules influences the autocorrelation function decay (see Equation 2.8). A typical fluctuations autocorrelation function[12] has an high amplitude for short time range (100ns) and decays until it has a null amplitude value for long time scale ($>$ 1ms). The decay, which depends also on the application and on the shape of the excitation volume is usually of the form $1/(1+x)$ or exponential.
From the macroscopic ensemble point of view, the $\tau = 0$ amplitude of the autocorrelation function is inversely proportional to the average number of molecules in the detection volume, whereas the characteristic time of the decay depends on the molecules average diffusion time. The normalized form of the autocorrelation function of the fluorescence fluctuation signal is usually used, and it is reported in Eq. .

$$g(\tau) = 1 + \frac{\langle \delta F(0) \delta F(t+\tau) \rangle}{\langle F \rangle^2} \tag{2.21}$$

[11] This (*ideal solution approximation* holds very good, in the actual measured cases, for chromophore concentration up to $\approx$ 100nM. For more concentrated solution a second order approximation has to be taken into account considering both the mechanical and the electrostatic interactions of the fluorescent molecules

[12] for the case of brownian molecules diffusion in solution

To analyze the experimental fluorescence fluctuation autocorrelation functions different analytical expressions and simulations have been built for the different applications and processes under study. In the next sections a brief overview of FCS applications to biological systems will be given.

2.2.3 Experimental Studies in FCS

2.2.3.1 Translational and Rotational Diffusion

In the experimental case in which the fluctuation of the fluorescence is only due to Brownian diffusion, in a 3D-Gaussian observation volume, the autocorrelation function can be analytically evaluated and results in [24]:

$$g(\tau) = 1 - \frac{1}{N}\left(1 + \frac{\tau}{\tau_D}\right)^{-1}\left(1 + \frac{\tau}{R^2\tau_D}\right)^{-1/2} \tag{2.22}$$

Where N is the average number of molecules in the excitation volume and τ_D is the diffusion time. By measuring and fitting the experimental autocorrelation function it is then possible to extrapolate both the concentration of the solution and the diffusion time of the solute. For example in 1978, Fahey and Webb [24], using FCS technique, measured the translational diffusion coefficient of the lipid, intercalating dye DiI molecules within lipid bilayer membranes ($DMPC$) at different temperatures. The study showed a dramatic reduction in the diffusion coefficient from $10^{-8}\text{cm}^2\text{s}^{-1}$ to less then $10^{-10}\text{cm}^2\text{s}^{-1}$ (see Figure 2.10). This jump was the confirmation of a phase transition between gel-like and liquid crystalline in these artificial membranes.

Another cause of the fluorescence signal fluctuation is the rotational motion of the chromophores. In fact, since the probability for a molecule to be excited by incoming light depends on the angle between the excitation dipole moment of the chromophore and the incident light polarization vector: if the dye is freely rotating its excitation rate will fluctuate.
The effect of the rotational motion can be expressed as an exponential term added to the standard autocorrelation function:

$$g_r(\tau) = g_T(\tau)(1 + e^{-\tau}\tau_R) \tag{2.23}$$

where $g_T(\tau)$ is the translational diffusion autocorrelation and τ_R is the time scale of rotational diffusion. As an example, Widengren et al. [4] measured the characteristic rotational time of the Green Fluorescent Protein to be around 20ns (see Figure 2.11).

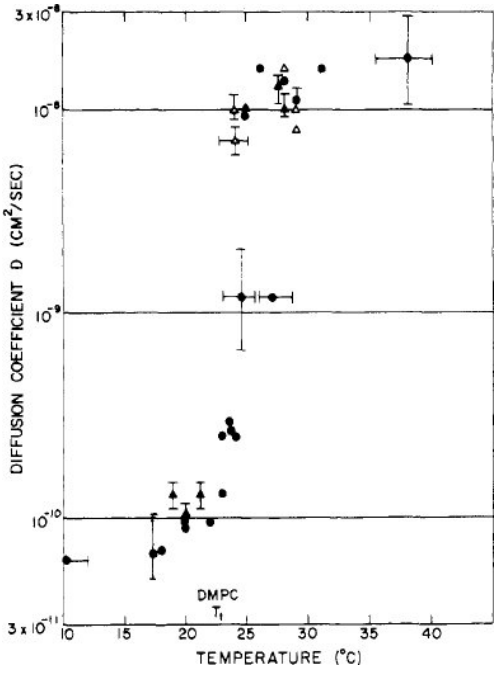

FIGURE 2.10: Diffusion coefficient of *DiI* in bilipid membranes as a function of temperature [24]

2.2.3.2 Photodynamical Properties of Fluorescent Dyes

The photo-physical properties of the chromophores and, as a consequence, of the fluorescently labelled proteins results to be of great importance for various applications in the field of fluorescence spectroscopy since they can limit or enhance[13] the performance and sensitivity of single molecule measurements.
Since, thephotodynamic processes influence the autocorrelation function in a complex way, depending on the energy level scheme [4] [25], FCS is the best technique to measure and characterize the photo-physical properties of a particular chromophore.

Under some particular assumptions [4], if just a triplet state is present (see Figure 2.13), the system can be simply treated as a two-state system and the fluctuations arise from the transition between a light-emitting state (S_0 ,S_1) and a triplet state (T).
In this case the autocorrelation function results in:

$$g(\tau) = 1 - \frac{1}{N}\left(1 + \frac{\tau}{\tau_D}\right)^{-1}\left(1 + \frac{\tau}{(\omega_0/z_0)^2 2\tau_D}\right)^{-1/2}\left(1 + \frac{T}{1-T}e^{-\tau/\tau_T}\right) \tag{2.24}$$

Where T is the fraction of molecules in the triplet state and τ_T is the characteristic lifetime of the triplet state (which is related to the rate constants as described in section and in Section 3.2 [4].

[13] in relation of the energy diagram involved and the experimental technique employed.

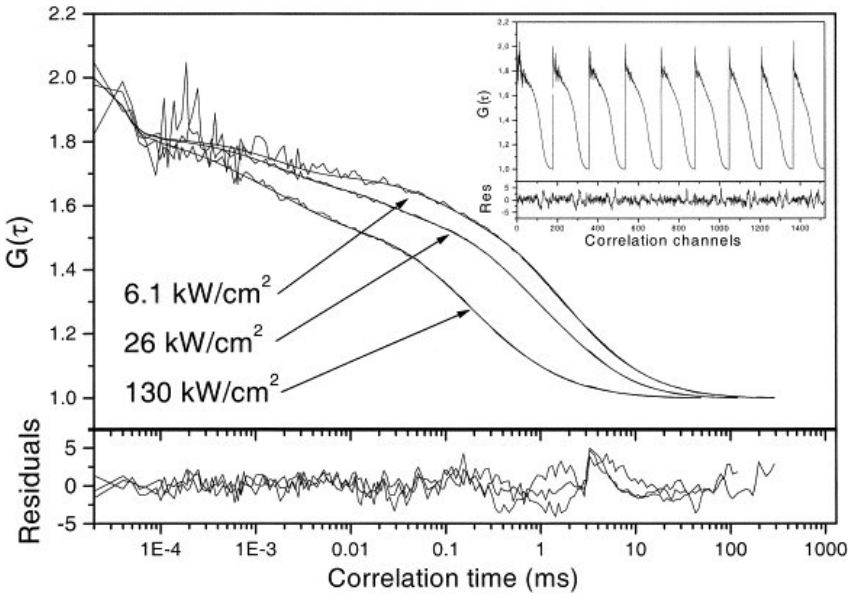

FIGURE 2.11: Autocorrelation function of BioST GFP measured at different excitation intensities [4]

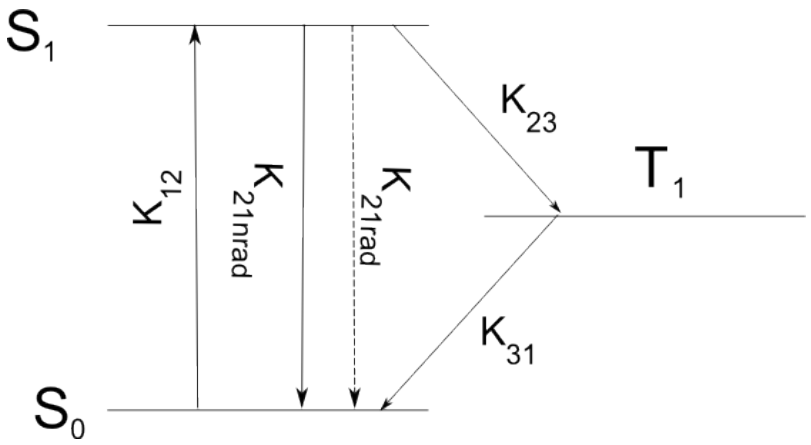

FIGURE 2.12: Energy level scheme for a simple triplet dynamics

A variety of fluorophores have been investigated by FCS methods in organic dyes as much as in GFP [26].

2.2.3.3 FCS as a binding assay

An extremely frequent application for FCS consists in characterizing molecular interaction (binding and de-binding reactions). If a labeled particle binds to another molecular object (better a bigger one) than the effect will be a slowdown in the diffusion, visible in the autocorrelation function as a contribute of a new species diffusing with a different

characteristic time. If two species are present the translational autocorrelation function becomes:

$$g(\tau) = \frac{Q_1 N_1}{(Q_1 N_1 + Q_2 N_2)^2}\left(1+\frac{\tau}{\tau_D}\right)^{-1}\left(1+\frac{\tau}{R^2\tau_{D1}}\right)^{-1/2} + \frac{Q_2 N_2}{(Q_1 N_1 + Q_2 N_2)^2}\left(1+\frac{\tau}{\tau_D}\right)^{-1}\left(1+\frac{\tau}{R^2\tau_{D2}}\right)^{-1/2} \tag{2.25}$$

Where Q_i and N_i are respectively the quantum yield and the average number of molecule in the observation volume, for the$i$-th species.
If τ_{D1} and τ_{D2} are sufficiently separated, the two components of the autocorrelation function can be analytically resolved by the function fitting tools and the concentration for the bound and unbound species can be obtained. Obtaining the chemical rate constants is, then, straightforward.
The best results are obtained if the diffusion coefficient of the free compounds has been previously measured.

With this methods a great variety of studies have been performed: proteins binding other proteins, polynucleic acids (DNA and RNA) binding other DNA and RNA, proteins binding polynucleic acids. To illustrate the principle, Bulseco and Wolf [25] showed the changes in autocorrelation function due to the binding of $Rh - Fab$ to IgG. The formation of a large $Rh - Fab/IgG$ complex results in the appearance of a slow diffusing component in the autocorrelation function. Figure **??** shows that the slow-diffusing fraction is increased at higher IgG concentrations and saturates when IgG is greater than 1 mM.

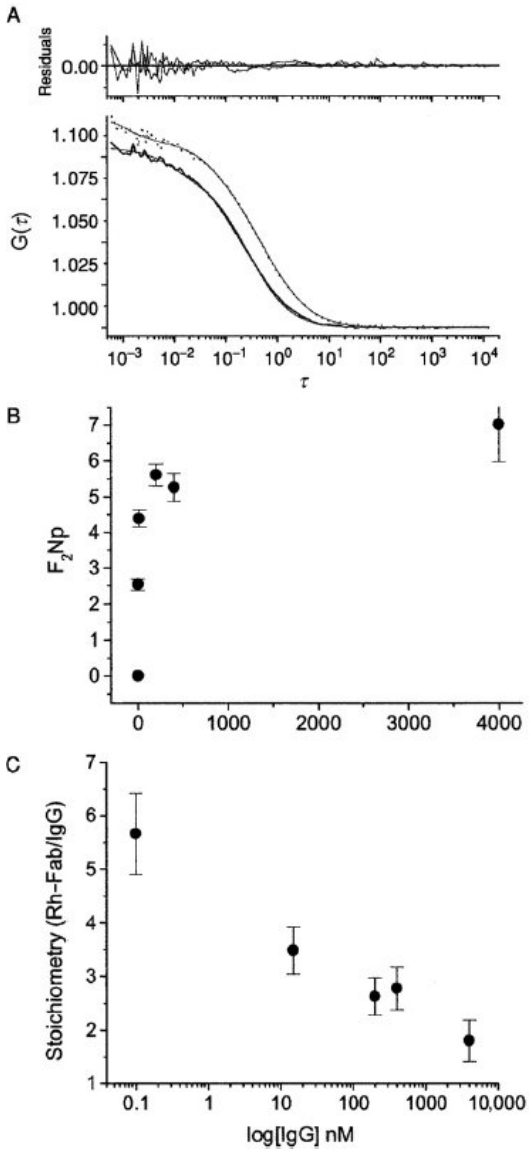

FIGURE 2.13: **A** Rh-Fab alone (solid line) and with 4-mM IgG (dotted line). **B** Fraction of slow-diffusing particles saturates as IgG concentration is increased. **C** Stoichiometry of $Rh - Fab$ binding to IgG in solution [25].

2.3 Introduction to the Laboratory Setup

The main requirement for the experimental applications to be presented in the following chapter is to have two laser beam (Pump and Probe) focused by the microscope in the very same region of a sample. The setup about to be described has been assembled specifically for this purpose.

The setup (as it is schematically represented in Figure C.3) is basically composed in three stages:

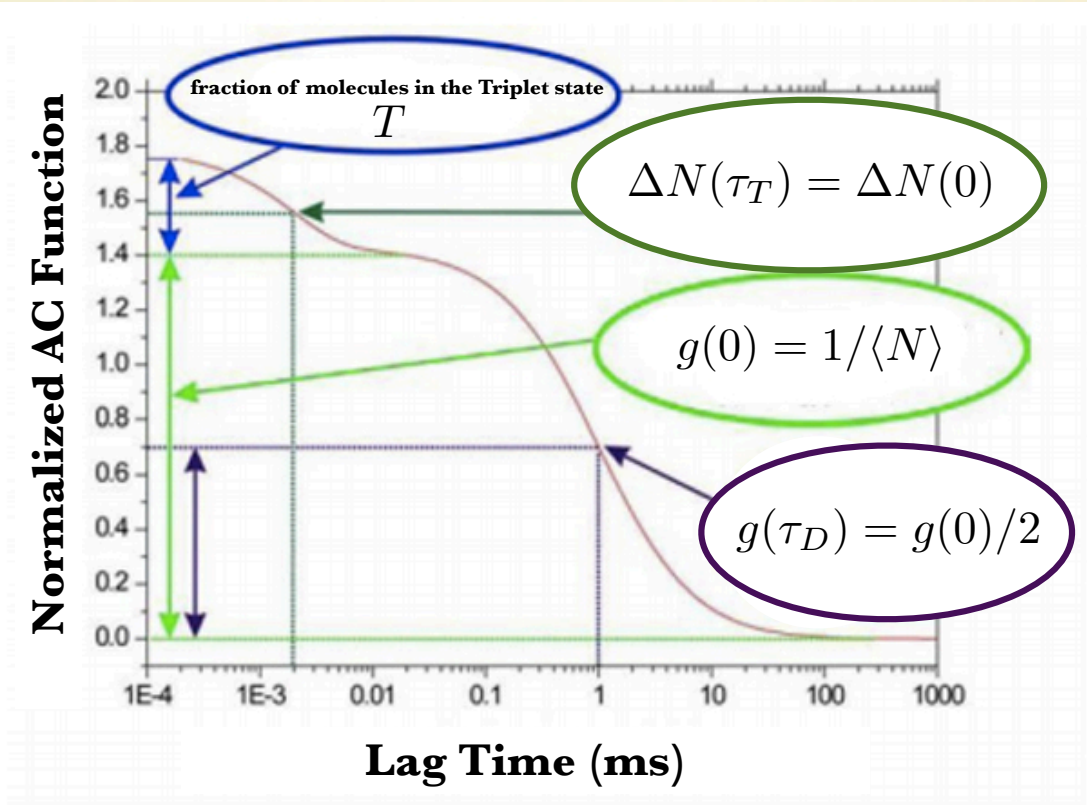

FIGURE 2.14: How to *read* an autocorrelation function. In green the amplitude of the $g(0)$ in the case of no triplet state activity. Since the average number of particle in the observation volume is $\langle N \rangle = 1/g(0)$, $\langle N \rangle = 1/1.4 = 0.7$. The lag time for which the amplitude of the $g(0)$ halves is the τ_D characteristic of the brownian diffusion(in violet): $g(1\text{ms}) = 0.7$, hence $\tau_D = 1\text{ms}$. In blue, the rising of the $g(0)$ due to the triplet activity represents the average fraction of molecules in the triplet state: $T = (1.75 - 1.4)/1.75 = 20\%$; the lag time at which this increment decreases to $1/e$ of it's original value is the τ_T characteristic life-time of the triplet state: $\tau_T = 2\mu\text{s}$.

- **Excitation Stage**: Whereas the pump beam is produced directly by a CW *Ar* gas laser source at the required 488nm, the probe beam is produced at 840nm by a pulsed resonant cavity and then passes through a frequency doubler in order to reach the required wavelength.
- **Focusing Stage**: The Nikon TE300 microscope in an epifluorescence setup both focus the exciting light and collect the emission radiation.
- **Signal/Image Acquisition Stage**: The signal detection is performed via a APD, a PMT of a CCD camera in relation to the specific measurement or application.

The pump and the probe beams are put together by means of a dichroic mirror reflecting the *violet* wavelengths and transmitting the *green* ones.
Alignment, in order to have the two beams focused on the same spot, is of course a critical requirements. After the merging dichroic elements the beams have to follow the

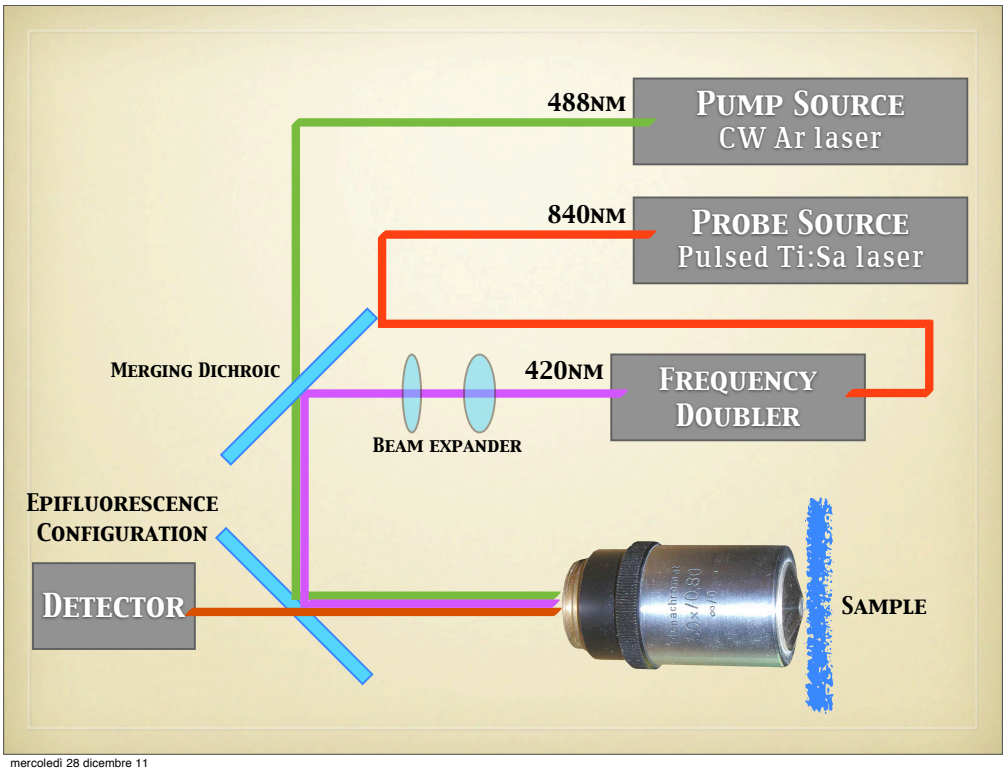

FIGURE 2.15: Experimental setup as it has been built to perform the measurements, described in details in Appendix **??**

very same path all the way to the microscope optics. A couple of mirrors for each beam, positioned before the dichroic allows the fine regulation of the beams alignment.

Since not only space localization but also the dimension of the focal volume are critical, a two-lens beam expander is placed on the probe-beam path in order to stretch it to the dimension of the pump-beam.

Chapter 3

GFP-Based PhotoSwitching Chromophores

In this Chapter an introduction on Green Fluorescence Proteins will be given.
Starting from the reasons of the GFP wide implementation in biological and biophysical study, we will discuss the fundamental photodynamics of the standard GFP in order to get in the specific details of the GFPMut2 class. As will be shown, this mutant class has a particular energy structure that can be exploited in order to obtain spectroscopic output parameters that are dependent on the pH, as well as other physical parameters, of the protein surrounding.

3.1 Brief Introduction to GFP

Green Fluorescent Protein was discovered by Shimomura et al. [27] while trying to elucidate the bioluminescence mechanism of the Aequorea jellyfish.
In 1962 the active component of the bioluminescence process was identified in a protein: the aequorin. Yet the acqueorin emission spectrum was peaked in the blue part of the visible spectrum, while the Aequora bioluminescence was distinctly green. A possible responsible of the green emission was identified in a protein *giving solutions that look slightly greenish in sunlight, though only yellowish under tungsten lights, and exhibiting a very bright, greenish fluorescence in the ultraviolet of a Mineralite*[27]: this was the first description of the GFP.
The GFP emission spectrum was soon published by the same group, showing a peak at 508 nm, near to the Aequorea tissue emission peak. After some studies, Morin and Hastings [28] found the same color shift in the Coelenterates Obelia (a hydroid) and Renilla (a sea pansy) thus suggesting a radiationless energy transfer as the mechanism

for exciting GFPs *in vivo*.

As reported by Tsien [29] different studies on GFP properties has been performed since its discovery, but the crucial breakthroughs came with the discovery of a the stunning property of the chromophore that is indeed responsible for its fluorescence when cloned. As demonstrated by Chalfie et al. [30] the expression of the GFP gene in other organisms is a sufficient condition for fluorescence. Therefore the gene contains in itself all the information necessary for the post-translational synthesis of the chromophore, and no jellyfish-specific enzymes are needed.

This chromophore is formed spontaneously from a tripeptide motif in the primary structure of GFP, so that its fluorescence is automatically turned on in every organism where it is expressed, moreover the integration of the chromophore inside the protein structure does not alter the protein function or localization. These are the unique properties that have enabled researchers to use GFP (and the successively developed mutant) in living system and have led to a widespread use in biophysical, biological and biomedical research, often been termed as a revolution.

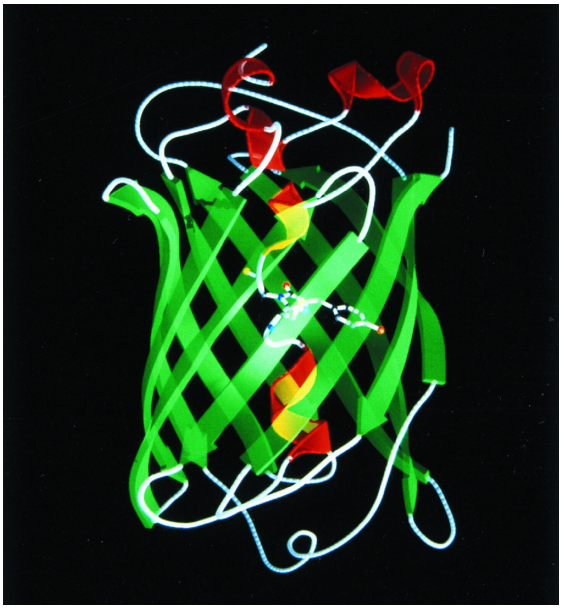

FIGURE 3.1: GFP ribbon diagram: Theα-helices are shown in red, the β-sheets are shown in green, and the chromophore is shown as a ball-and-stick model [29]

The GFP 3D Structure (see Figure 3.1, is composed by a series of β-sheet structure forming a cylinder through which is diagonally threaded an α-helix bearing the chromophore. The β-barrel is made up by 11 sheets, forming a cylinder shape with a diameter of 2.4nm and a height of 4.2nm that protects the chromophore. Various polar groups and structured water molecules are situated adjacent to the chromophore; among these, of particular importance are Gln69, Arg96, His148, Thr203, Ser205, and Glu222 [29].

3.2 GFP Photodynamics

As anticipated in the introductory Section, from a biophysical point of view, Green Fluorescence Protein appeal in biomedical studies is due to its possibility to absorb UV-blue light and emit green light with relatively high efficiency. Moreover the various possible mutations have an impressive effect not only on the excitation and emission wavelength but also on the fluorescence quantum yield: for example the wild type GFP shows ϕ=0.8 while the Y66H mutants have quantum yields as low as 0.2 (see for example [31], [32], [33] and [34]).
The use of GFP can be limited by several photodynamic mechanisms, particularly photobleaching[35],[36], blinking (or flickering)[37], photo-activation[38] and photoswitching or photochromicity[35], [39], [40], [41]. Most of these properties, when coupled to the sensitivity of the protein chromophore to the external environment (pH, chlorine ions etc.) can also be exploited to obtain molecular sensors[42],[43] and to enhance the image resolution by single molecule photo-activation[44]. The Beating Mode image acquisition protocol that will be presented in the following Chapters bases its principles exactly on this concept.

Blinking and bleaching affect indeed the fluorescence signal by reducing the (effective) quantum yield[31] and by inducing fluorescence fluctuations with characteristic times in the range of microseconds to seconds[45],[46],[47],[48],[49] and [50].
The most limiting process is **photobleaching**. This mechanism[1] is recognized in the single molecule experiments as a permanent loss of fluorescence of the observed molecule and in FCS as a shortening of the apparent diffusion time τ_D, as a change of the autocorrelation amplitude and shape, and as a decrease of the maximum achievable brightness[47] and [53].

The protein spontaneous blinking processes have been ascribed to transitions to dark (neutral or zwitterionic) states reached through tiny conformational changes (cis-trans transitions[35]) coupled to changes in the protonation state of the chromophore ([45],[33] and [48]) that involves also the rearrangement of the proton network within the chromophore pocket [48],[54]. The blinking efficiency of the particular GFP protein depends on the specific mutations [37] and on the physical (temperature) [55] and chemical (pH and metal ions) [43],[56] parameters of the solution. The dependence of blinking on the pH has been investigated extensively by FCS experiments in solution [45],[50] and [57] and it has also led to devise intracellular sensors of pH or ions based on GFPs [35],[58] and [59].

[1] Photobleaching can have different origin depending on the excitation mode (OPE [51], TPE[36],[47] and [52])

The photo-switching of GFP fluorescence has led to the concept of RESOLFT as a reconstruction imaging technique to enhance the spatial resolution [44].

The focus of this work is to develop alternative ways to exploit photo-induced fluorescence fluctuations in order to implement advanced cell imaging aimed at enhancing the information content of the image. The proteins that have been used in this work are derived from the parent GFPMut2 protein that carries the mutations S65A, V68L, S72A [60]. Photo-switching properties (i.e. the emission wavelength shift upon irradiation with UV-blue light) are induced in this mutant by the mutation of glutamate 222 into glutamine, that is believed to be the key mutation for the induction of stable (i.e. slowly, thermally relaxed) photo-activation in several other mutants [31],[35].
The E222Q mutation of GFPMut2, resulting in a protein called here Mut2Q, is characterized by a millisecond recovery of the fluorescence after photoactivation. The spectroscopic properties of these mutants under OP and TP excitation have been largely reported in the literature (see for example Quercioli et al. [2], [48] and [61]) and a summary is reported for discussion purposes in Figure 3.2.

3.3 GFP Mut2 Photoactive Mutants

3.3.1 GFPMut2 Single Beam Photodynamics

Photoactivation and photoswitching of GFP involve the use of two laser beams that may conventionally be indicated as **pump** and **probe** beams, that respectively induce the ground-excited state transition and photo-induces a change in the fluorescence emission. Obviously, for applications of the photoswitching process, as it is our focus here, it is essential to have first a detailed knowledge of the fluorescence dynamics that is induced by a single (pump) beam. As already mentioned in the previous Chapter the fluorescence dynamics can be studied in solutions by means of FCS. The autocorrelation function (ACF) of the fluorescence intensity (see Section 2.2) can be analyzed in terms of a superposition of the diffusive (hyperbolic) and the photodynamics (exponential) components:

$$G(t) = G_{D,OPE}(t) \times \prod_j \left[1 + \frac{A_j}{1 - A_j} \exp\left(-t/\tau_j\right)\right] \tag{3.1}$$

$$G_{D,OPE}(t) = \frac{\gamma_{OPE}}{\langle N \rangle} \left(1 + \frac{t}{\tau_{XY}}\right)^{-1} \left(1 + \frac{t}{\tau_Z}\right)^{-1/2}$$

where $\langle N \rangle$ is the average number of molecules in the excitation volume, $\gamma_{OPE} \cong 0.35$ and the diffusion time, τ_{XY}, is related to the diffusion coefficient and to the beam waist,

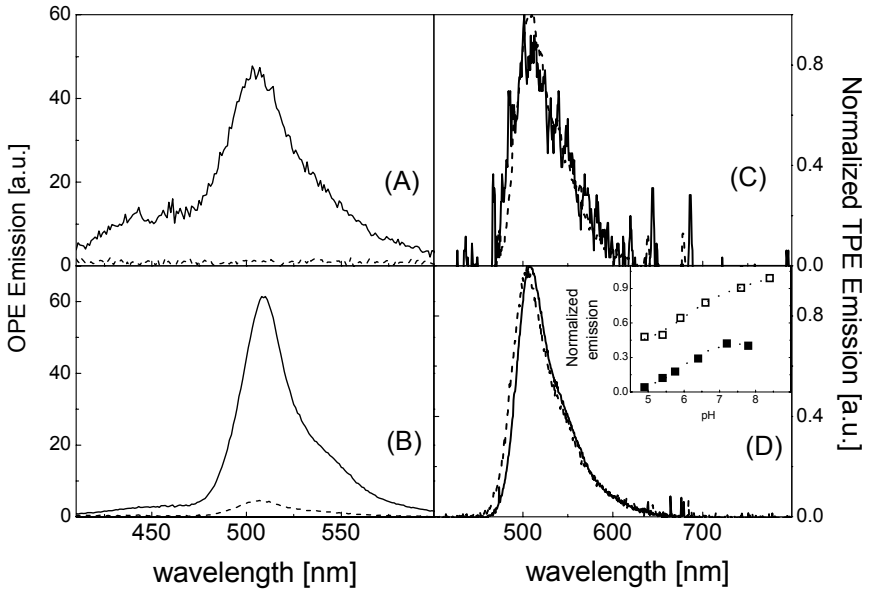

FIGURE 3.2: **GFP standard photodynamic properties**: one-photon primed (?exc =395nm) fluorescence emission of the GFPMut2 (solid line) and Mut2Q (dotted line) mutants in acidic (pH=5; panel **A**) and basic (pH=8.5; panel **B**) conditions. The buffer was citrate-phosphate (10-100 mM), protein concentration 0.1 ?M. Panels **C** and **D** report the normalized emission spectra at pH=5 **(C)** and at pH=8.5 **(D)** under TPE excitation at 890 nm. Protein concentration was 10-30 nM, laser intensity was ? 11 MW/cm2 (the data were Fourier smoothed over 5 points). The inset of panel D reports the pH titration of fluorescence at 510 nm. Open and filled squares refer to GFPMut2 and Mut2Q, respectively. The solid lines are the best fit of these data to the single acid-base equilibrium (sigmoidal) function, $A/(1+10^{(pH?pK)/\delta}$), with $pK = 6.20.1$ (GFPMut2) and $pK = 6.00.1$(Mut2Q) [1].

ω_0 as $\tau_{XY} = \omega_0^2/4D$. The value for the relaxation time for motions along the optical axis is typically assumed $\tau_Z \cong 5 \cdot \tau_{X,Y}$.

The photodynamics components, typically two in the range 1-300 μs for most of the GFP mutants, may show dependence both in the relaxation times and in the fluctuation amplitudes, on pH, on temperature and on excitation intensity. The two main components correspond to the protonation dynamics ($j = P$ in Equation 3.1) and to cis-trans isomerizations or other photo-induced chromophore structure changes ($j = L$ in Equation 3.1).

The characterization for each particular mutant, of the dependence of the photodynamics parameters on the chemical and physical properties of the environment, is evidently of paramount importance for future applications in cells, where the pH may vary substantially and where the temperature is typically around 37 Celsius degrees. This characterization for the GFPMut2 mutants used in this work will be presented in Chapter 4 As an example, the mutation of the histidine 148 of GFPMut2 into a glycine does not

affect appreciably the molecular brightness and the relaxation rates of the single beam photodynamics [48] while it induces a destabilization of the protein in terms of unfolding kinetics and as a shift of the chromophore pK to values higher than $\cong 6$, typical of most GFP mutants (see [48], Figure 3.2 and [61]). On the other hand the **E222Q** mutation induces a marked decrease in the chromophore brightness (Figure 3.2) particularly under OPE (Figure 3.2 inset). A similar finding has been reported by Jung and coworkers for a set of GFP mutants (see Table 3.1) encompassing a.a. 203, 65 and 222. This fact makes the mutation E222Q potentially useful to obtain a large photo-induced enhancement of the fluorescence emission.

Concerning the relaxation rates, the mutants of GFPMut2 under single beam excitation display values in the range 5-60 kHz depending on the excitation intensity and on pH [48]. As can be seen in Figure 3.3 and Table 3.1, a marked contribution of the photodynamics to the fluorescence correlation curves is evident at acidic pH values.

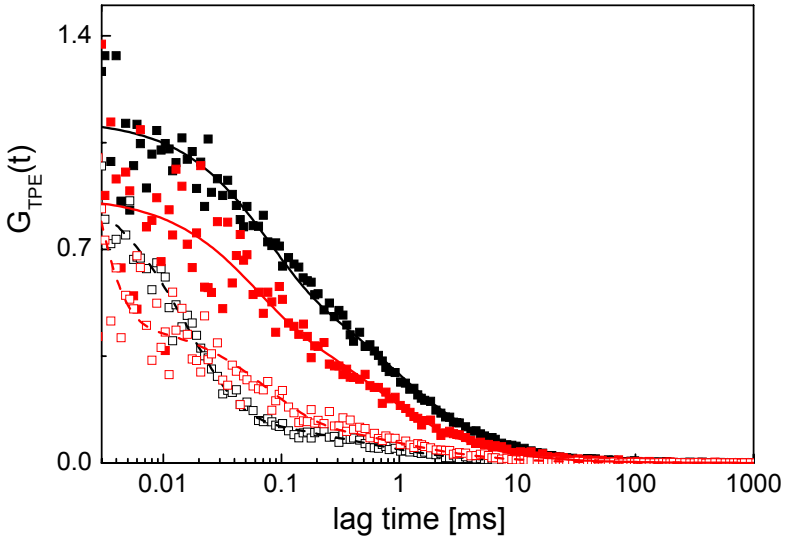

FIGURE 3.3: Normalized ACFs of the fluorescence fluctuations measured on solutions of GPFmut2 (black) and Mut2Q (red) for pH=5 (open symbols) and pH=8.6 (filled symbols) by TPE at $\lambda = 890$ nm. The solid lines are the best fit to Eq. 1 (TPE). The best fit parameters are reported in Table 3.1 [1].

	τ_D [μs]	A_L	τ_D [μs]	A_P	τ_P [μs]
GFPmut2 (8.4)	900 ± 60	0.45 ± 0.02	73 ± 7		
GFPmut2 (4.9)	529 ± 60	0.25 ± 0.38	76 ± 20	0.86 ± 0.02	16 ± 2
Mut2Q (8)	622 ± 248	0.44 ± 0.1	57 ± 20		
Mut2Q (5)	1200 ± 300	0.72 ± 0.02	84 ± 20	0.95 ± 0.02	1.53 ± 0.1

TABLE 3.1: Best fit parameters of the ACFs reported in Figure 3.3 for two GFPMut2 mutants: The number in round parentheses in the first column indicate the pH of the solution

3.3.2 GFPMut2 Dual Beam Photodynamics: FCS analysis

The mutation that appears to confer to the GFP mutants photochromic properties is the E222Q, as delineated in the literature (for example [35]). A recently proposed scheme for the chromophore photodynamics takes into account protonation of the cis- and trans-forms and a photoinduced isomerization process which is much faster than the thermally driven trans-cis isomerization.

The photoinduced isomerization and the neutral-anionic transitions are relatively fast

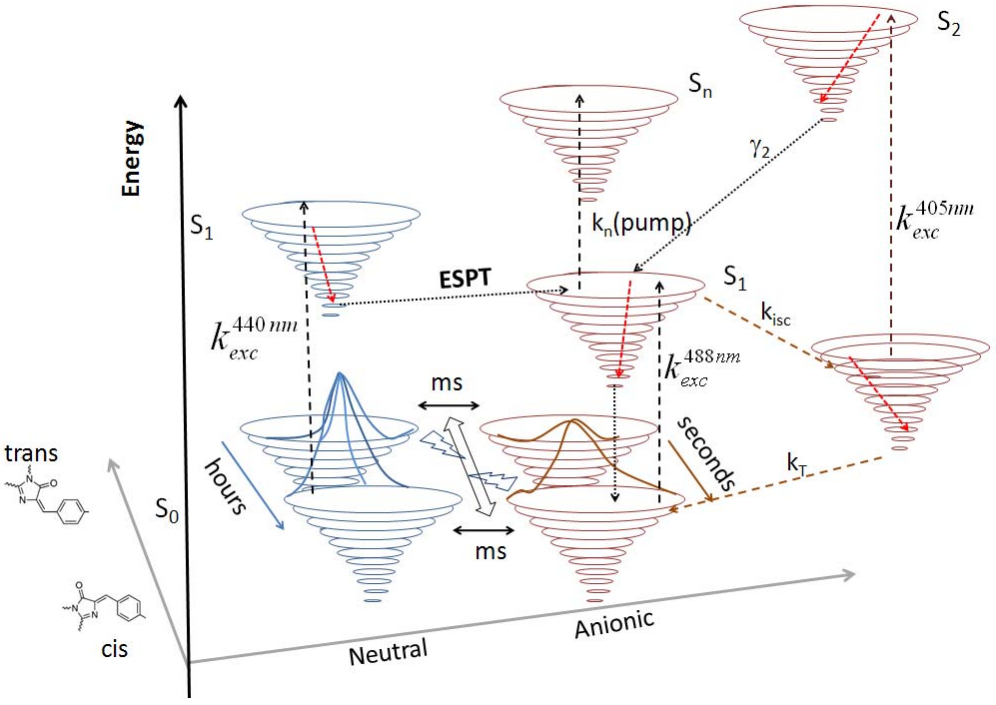

FIGURE 3.4: The circles represent the vibrational sub-levels in the electronic states. Only the most relevant energetic barriers are indicated in the scheme. The trans configuration of the neutral chromophore represents the dark state of the GFP[35]. The solid lines corresponds to thermally activated transitions between the ground states (the activation barriers are depicted as possible routes through the activation state). The open double arrow indicate the photo-conversion cis-trans mechanism. The dashed lines represent the photo-induced transitions and correspond to the 490 nm absorption band (S_0 (anionic) $\rightarrow S_1$ (anionic)), to the 440 nm absorption band (S_0 (neutral) $\rightarrow S_1$ (neutral)) and to the photoactivated recovery of the fluorescence by depletion of the Dark Trap (T) state by the (405nm) probe beam ($T \rightarrow S_2$; [37]). The ESPT mechanism between S_1(neutral) and S_1(anionic) is also indicated in the scheme as a dotted arrow. Emission transitions are not indicated for sake of simplicity.

processes lying in the range of ms [46],[40]. The thermal recovery of the cis-form of the chromophore at the ground state occurs instead over long times, from tens of seconds to hours [35],[40]. These properties can be exploited successfully for cell tracking, bleaching

and FRAP experiments, by carrying out sequential on-off photocycles. It is noteworthy that the photoactivation has a marked but slow (tens of seconds) thermal recovery.

Recent experiments, reported by our group (see Quercioli et al. [2], Chirico et al. [1] and [46]) and in this work on the Mut2Q mutant, may provide an additional point of view of photo-activation.
In fact, most of the work presented on GFP photochromicity has exploited the slow relaxation between ground electronic states [35], [45]. However there is the possibility to exploit the photo-induced transitions between excited states of the chromophore. One of these transitions is the so called ESPT (Excited State Electron Transfer) and involves directly the E222 residue and is the origin of the large Stokes shift observed in many GFP mutants [62], [63] and [64]. A possible outline of this complex scenario is given in Figure 3.4.

Photoswitching events have been observed under single laser beam excitation both on immobilized GFP proteins [65] and in diluted solutions [45], under two laser beams excitation as more recently reported [35], [46], [66] and [67]. Under single beam excitation the photoswitching event can be rationalized basing on the inter-system crossing transition from S_1 to D (Figure 3.4). This leads to single molecule blinking and to an exponential decay superimposed to the diffusive component of the fluorescence fluctuations correlation function (Equation 3.1).
Under two laser beams excitation, the photoswitching effect is observed when a protein solution is shined continuously with a 488 nm laser beam, that primes the emission of the anionic form of the chromophore, and a second laser beam, tuned in the range 405-420 nm, impinges on the sample. This *Probe* beam induces a depletion of the dark state D through the transitions to higher energy states S_2, S_n (see Figure 3.4).
We can more easily gain information on the photoactivation efficiency and dynamics (the experimental characterization of the mutants used in this work will be reported in Chapter 5) by modulating the probe (or the pump) beam at a frequency ν in the proper range. In Figure 3.5 are reported fluorescence traces collected under pump + modulated probe excitation; from these it is possible to identify the two main features of the photoactivation process:

- the increase in the fluorescence emission of the protein under dual beam excitation, referred in the following Chapters as **Enhancement Ratio** $\Delta F/F_0$;
- the delayed response of the fluorescence signal to the change in the excitation mode/intensity, referred in the text also as **Activation/Deactivation Times** referring to the physical response of the D level population to the on/off switch of the probe beam.

The Mut2 E.R. is of limited extent, when compared to other photoactivable proteins such as PA-GFP, Dronpa, Kaede, etc. However, it is of the same order of magnitude of the photoactivation found in wt-GFP [38], [68] and the limited bleaching induced by the probe beam in this mutant makes it potentially amenable to cell applications [46].

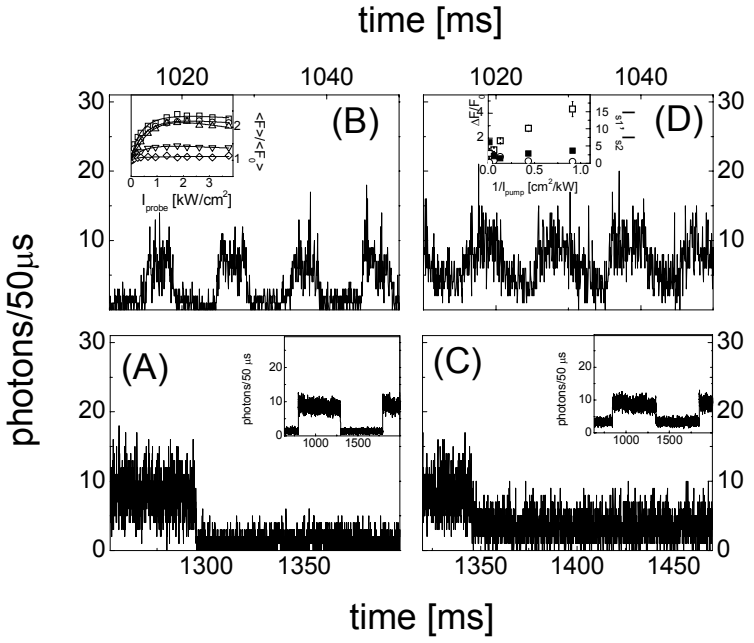

FIGURE 3.5: Fluorescence traces collected from dilute solutions (20 nM) of GFPMut2 (left panels) and Mut2Q (right panels) under the action of the pump (488 nm, continuously irradiating) and probe (405 nm, modulated) beams. The solution pH was 8.6. The probe beam was alternated on the sample by means of an electro-mechanical shutter at $\nu = 1$Hz (panels **A** and **C**) and $\nu = 100$Hz (panels **B** and **D**). The insets in panels **A** and **C** report a longer stretch of the traces (smoothed by adjacent averaging over 5 points). The inset in panel **B** reports the increase of the fluorescence primed at 488 nm under the action of the 405 nm probe beam at increasing pump beam intensities (1.1, squares; 2.3, circles; 7.7, triangles; 16.3, down triangles; 78 kW/cm2, diamonds). The solid lines are best fit curves as described in the text, and the best fit parameters are reported as a function of $1/I_{pump}$ in the inset of panel **D**: $\Delta F/F_0$ (left axis, open squares), I_{S1} (in kW/cm2 right axis, open circles) and I_{S2} (in kW/cm2 right axis, filled squares) Chirico et al. [1].

The activation of the fluorescence by the blue probe laser is peculiar of the E222Q mutation since the parent protein GFPMut2 does show only a minor bleaching induced by the 405nm irradiation but no enhancement or delayed emission. The Mut2Q mutant displays also a peculiarly slow (millisecond) kinetic response to changes in the blue excitation light intensity. The fluorescence traces reported in Figure 3.5 show indeed a rounded transition of the signal when the probe beam is switched on or off. This effect, which is visible only for the Mut2Q mutant, is more pronounced under high modulation

frequencies, $\nu \cong 100 - 300$Hz, but also at modulation frequencies as low as $\nu = 1$Hz it is possible to note that the on-off (or off-on) transitions are not as sharp, at the 50μs time resolution, as can be observed for the GFPMut2 parent protein (Figure 3.5C).
The maximum relative enhancement $\Delta F/F_0$ can be obtained by fitting the fluorescence emission as a function of I_{probe}, at selected values of I_{pump}, to the trial function

$$\langle F \rangle = F_0 + \Delta F \cdot I_{probe}(I_{S1} + I_{probe} + (I_{probe}/I_{S2})^2)^{-1}$$

where I_{S1} and I_{S1} are saturation intensities that account for the dark state population and for the excited singlet to higher energy states transitions [46]. From the best fit of the data (Figure 3.5B, inset) it is possible to estimate a maximum value of the E.R. $\cong 4$ (see Figure 3.5D, inset).

3.3.2.1 Mathematical and Physical Analysis of the Process

The light-triggered enhancement process outlined above and represented by the data reported in Figure 3.5 can be analyzed by means of FCS in condition of **modulated excitation**. With this techniqueit is possible to estimate the characteristic response time at which the population of the state D follows the change in the excitation condition.
In general, for steady single (pump) beam excitation the fluorescence signal can be written as:

$$F(t,T) \cong k_R T \eta \sigma \langle I_{pump}(t) \rangle \int W(\mathbf{r}) S_1(\mathbf{r},t)\, d\mathbf{r} \tag{3.2}$$

where k_R is the radiative constant, T is the sampling time[2], η is the detection efficiency and σ is the absorption cross section. $W(\mathbf{r})$ is the normalized intensity of the excitation profile[3], $\langle I_{pump} \rangle$ is the average intensity of the steady pump beam and $S_1(\mathbf{r},t)$ is the number at the position $\mathbf{r}$ and time t of the molecules in the excited state S_1.
In this experimental condition, the fluctuations of the fluorescence signal may come from the fluctuations in the number of the molecules residing in the S_1 state, $S_1(\mathbf{r},t)$, or the changes in the pump intensity I_{pump}. The function $S_1(\mathbf{r},t)$ can be written in terms of the product of the number, $N(\mathbf{r},t)$, of molecules found at time t in position $\mathbf{r}$, times the probability, $P_1(\mathbf{r},t)$, of being excited to the state S_1.

Let us first consider the most simple case: no photodynamics exists in the time range explored by the FCS ACFs, and the modulation frequency of the pump excitation falls in

[2]For obvious reasons the sampling time must to be much smaller than the characteristic fluorescence fluctuation time

[3]The intensity excitation profile can be considered, as discussed in Appendix B as a 3D Gaussian or as a Gaussian-Lorentian profile. In the latter case a correction to the ACF fitting form can be introduced to improve the results of the fit.

ranges where no coupling with the photodynamics exists. Equation 3.2 hence becomes:

$$F_{NP}(t,T) \cong k_R \eta \sigma T \cdot I_{pump} \int W(\mathbf{r}) N(\mathbf{r},t)\, d\mathbf{r} \tag{3.3}$$

The fluorescence ACF can be described by:

$$\begin{aligned} g(\tau) &= \frac{\langle \delta F_{NP}(t+\tau,T)\delta F_{NP}(t,T)\rangle_t}{\langle F(t,T)\rangle_t^2} \\ &\cong \frac{\langle N(t+\tau)N(t)\rangle_t}{\langle N\cdot I_{pump}\rangle_t^2}\langle \delta I_{pump}(t+\tau)\delta I_{pump}(t)\rangle_t + \\ &\quad \frac{\langle I_{pump}(t+\tau)I_{pump}(t)\rangle_t}{\langle N\cdot I_{pump}\rangle_t^2}\langle \delta N(t+\tau)\delta N(t)\rangle_t \end{aligned} \tag{3.4}$$

where

$$N(t) = \int W(\mathbf{r}) N(\mathbf{r},t) d\mathbf{r}$$

and

$$\delta N(t) = \int W(\mathbf{r}) \delta N(\mathbf{r},t) dr$$

If we now define:

$$D_N(\tau) = \frac{\left\langle \int \langle W(\mathbf{r})\delta N(\mathbf{r},t) W(\mathbf{r}')\delta N(\mathbf{r}',t+\tau)\rangle d\mathbf{r} d\mathbf{r}' \right\rangle}{\left\langle N \right\rangle^2} \tag{3.5}$$

$$D_I(\tau) = \frac{\left\langle \delta I_{pump}(t+\tau)\delta I_{pump}(t) \right\rangle}{\left\langle I_{pump} \right\rangle_t^2} \tag{3.6}$$

It is then possible to rearrange terms in Equation 3.4 so that:

$$g(\tau) = D_I(\tau) + D_N(\tau)(1 + 4\cdot D_I(\tau)) \tag{3.7}$$

From this expression it is easy to identify two limiting behaviors.
In the study of highly diluted solutions, **under modulated excitation** (of either the pump or the probe beam), the fluorescence fluctuations correlation function is dominated by the number fluctuations (i.e. $D_N(\tau)$) and the ACF is well approximated by the form:

$$g_{N\to 0}(\tau) \cong D_N(\tau)(1 + 4\cdot D_I(\tau)) \tag{3.8}$$

On the other hand, for relatively concentrated solutions the limiting behavior is:

$$g_{N\to\infty}(\tau) \cong D_I(\tau) \tag{3.9}$$

Similar results are obtained if we take into account the protein photodynamics whose characteristic times are assumed to be much smaller than the typical modulation time of the pump beam intensity. In this case the $D_N(\tau)$ function should be simply replaced with the whole ACF decay. In the specific case where we are interested in studying the effect of the beam intensity modulation on the protein photodynamics, we should then measure at $\langle N \rangle \cong$ 20-40 molecules per excitation volume.
However, if the internal photodynamics contains relaxation times of the order of the pump beam intensity modulation, we must consider a direct coupling between the photodynamics and the pump beam modulation that brings us to reconsider the parameters entering Equation 3.3. In this case the variable over which to compute the $D_I(\tau)$ correlation function changes from I_{pump} to $\int_{-\infty}^{t} I_{pump}(x) P_1(\mathbf{r}, t-x; I_{probe})\, dx$, where $P_1(\mathbf{r}, t; I_{probe})$ represent the probability, per unit of excitation intensity, to find a molecule that sits at r at the time t in the S1 excited state.
The functional dependence of $P_1(\mathbf{r}, t; I_{probe})$ on I_{probe} can be inferred from the analysis[4] of the linear system of equations that describe the evolution of the energy levels populations as reported in Bizzarri et al. [46].

It must be further noticed that by modulating the excitation beam we are sampling the dynamic response of the quantum system. In other words we are performing a Fourier (or Laplace) analysis of the response function, $P_1(\mathbf{r}, t; I_{probe})$ of the quantum system to a pulsed excitation.
In fact if we suppose that the quantum system response is a single exponential with relaxation rate Γ[5] independently of the position within the excitation volume[6], and if we suppose that the excitation (pump only at this stage) changes with time as $I_{pump}(x) = A\cos(\Omega t)$, the intensity over which to compute the fluctuations becomes:

$$\int_{-\infty}^{t} I_{pump}(x) P_1(\mathbf{r}, t; I_{probe})\, dx = \frac{A}{\sqrt{\Omega^2 + \Gamma^2}} \cos\left(\Omega t - \frac{\Omega}{\Gamma}\right) \tag{3.10}$$

Thus, the intensity ACF is then given by:

$$D_I(\tau) = \frac{1}{\Omega^2 + \Gamma^2} \cos^2(\Omega t) = \frac{m^2(\Omega)}{2} \cos(\Omega \tau) \tag{3.11}$$

Therefore, we can measure the relaxation rate from the zero lag time extrapolation of the correlation function, $D_I(0)^{-1} = \Omega^2 + \Gamma^2$.

The above formalism can be applied to the characterization of photo-switching processes, both in solutions and on images. In fact, the same formalism as in Equations 3.10 and

[4] In terms of eigenvalues and eigenvectors
[5] i.e. $P_1(\mathbf{r}, t; I_{probe}) \propto \exp[-\Gamma t]$
[6] Which, as an hypothesis, requires by the way some additional considerations

3.11 can be used when modulating the probe beam, if we exploit the hypothesis that the $P_1(\mathbf{r}, t; I_{probe})$ function can be expanded in series of eigenvalues that depend linearly on I_{probe}, at least for $I_{probe} < I_{S_1}$ (condition that is physically consistent with the reality as shown in Figure 3.5, inset, [46].

Any relaxation component will then provide a demodulation of the zero lag time correlation function as that reported in Equation 3.11. If we employ an average of 40 molecules per excitation volume the correlation function is given by Equations 3.9 and 3.11 and the dependence of the zero lag time extrapolation, $g(0)$, on the modulation frequency can be analyzed accordingly, as shown, for example, in Figure 3.6.
In real experiments the situation is more complex due to the presence of a background (with average value $\langle B \rangle$), and the demodulation factor changes to the form:

$$D_I(\tau) = A^2 \frac{m^2(\Omega)}{2} \frac{\langle F^2 \rangle}{\langle F^2 \rangle + \langle B^2 \rangle} \cos^2(\Omega\tau) \tag{3.12}$$

Moreover, if more than one relaxation component, with number fractions f_i in the range accessible to FCS (relaxation rates $<$ 1MHz), the intensity correlation function becomes:

$$\begin{aligned} D_I(\tau) \quad = \quad & \frac{A^2}{2} \frac{\langle F^2 \rangle}{\langle F^2 \rangle + \langle B^2 \rangle} \times \\ & \times \left[\left(\sum_i f_i m_i^2(\Omega) \right)^2 + \left(\sum_i f_i m_i(\Omega) \sqrt{1 - m_i^2(\Omega)} \right)^2 \right] \cos^2(\Omega\tau) \end{aligned} \tag{3.13}$$

Indeed the comparison of the ACFs (as shown in Figure 3.6) acquired under probe modulated intensity of the Mut2 and the Mut2Q mutants indicates that only the latter mutant photodynamics presents two relaxation components (as could be judged also from Figure 3.5C), while Mut2 does not present any relaxation component in the kHz-Hz range [46]. The two photodynamics components of Mut2Q have relaxation times of the order of few tens of ms that depend, in vitro, on the solution pH, while are not affected appreciably by the solution viscosity and temperature [46].
From the merely theoretical point of view, the function $g(0, \nu)$ fitted as a double time exponential decay will return the value of the average time of the proceed of population and depopulation of the dark state D (as in Figure 3.6B). Anyway, as it will be showed in Chapter 4.1.3.1 in the experimental fit a third time component will be necessary; this component probably represents an additional photodynamic process, not yet taken into account in the model of Figure 3.4 that overlap with the D-state population / depopulation dynamics.

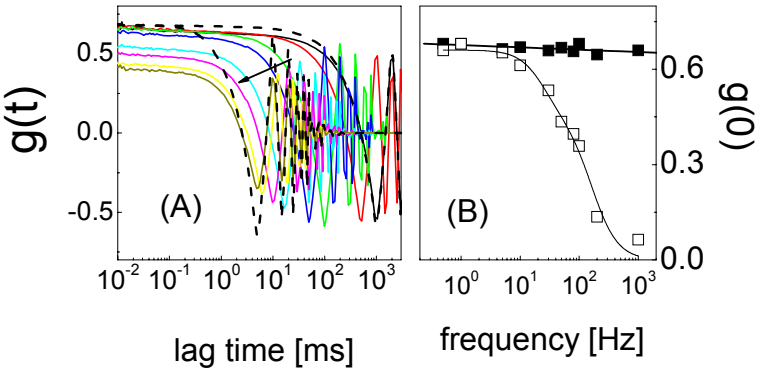

FIGURE 3.6: **Panel A**: ACFs of Mut2Q solutions (40 molecules per excitation volume), under modulated probe beam excitation (λ_{probe} = 420nm) at modulation frequencies varying from 0.5 to 100 Hz (0.5, black; 1, red; 5, green; 10, blue; 30, cyan; 50, magenta; 80, yellow and 100 Hz, dark olive). The dashed black lines report the ACFs of the same solution under pump modulation (0.5 and 100 Hz).
Panel B: zero lag time correlation function, $g(0)$, as a function of the modulation frequency for the cases of probe modulation (open squares) and pump modulation (filled squares). The lines are the best fit to the data of Equation **??**Chirico et al. [1].

Part II

Beating Mode Acquisition Protocol

Chapter 4

Improving Chromophore Knowledge: Joined Experimental and Simulative Approach

In this Chapter, a characterization of the Enhancement Ratio and of the population and de-population time as a function of pH of the chromophore will be presented for both GFPMut2 E222Q and Mut2GQ mutants.
Then it will be outlined a mathematical and simulative approach to uncouple the diffusion and photo activation dynamics in the FCS analysis [3].

4.1 Experimental characterization of the Photodynamics

4.1.1 Energy Level Scheme

Both *E222Q* and *Mut2GQ* are mutants of the GFP proteins of Mut2 class, where the glutamic acid (E) in position *222* is replaced by a glutamine (Q); the *Mut2GQ* also contains the mutation H148G where the histidine (H) in position *148* is replaced by a glycine (G) Bizzarri et al. [69].

Both the mutants present the capability of the conformational change, described in Figure 3.4, that has the effect of inhibit the fluorescence of the GFP molecules as previously described in details in Section 3.3.2, where we called this conformational state a *Trap* Dark state D.
For the sake of photodynamics analysis and experiment the complex of conformational

and energy state pictured in Figure 3.4 can be simplified, for these two GFPMut2 mutants under analysis here. This simplification describes the chromophore energy framework with a 4-level system comprising two long lifetime state (see Figure 4.1). In these diagrams the first long-lifetime level T represents the single (or multiple) triplet state of the proteins[1], whereas the level D represents the neutral conformational state of the mutants which can be characterized, as already explained in Section 3.3.2.1, by an extremely long lifetime (fraction of seconds to hours) Jung et al. [70].
The outgoing photo-induced population dynamics out of the D state, pumped by the probe beam, is represented by an excitation of the neutral state $D \rightarrow D*$ and than the relaxation process can bring the electron both on S_1 or S_0 of the anionic conformational state. The process characteristics rates of these processes have to be much faster than the simple $D \rightarrow S_0$ in order to explain the presence of the probe beam-triggered fluorescence enhancement.

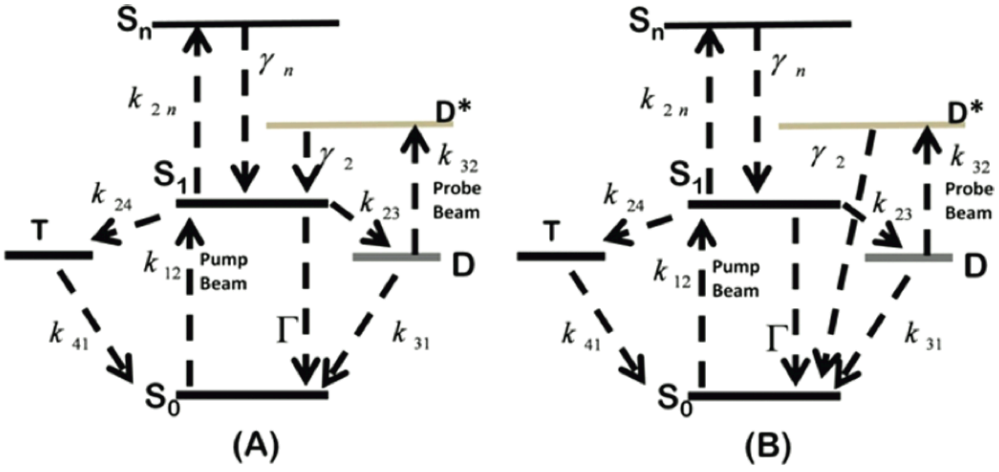

FIGURE 4.1: Examples of two energy diagrams that may describe part of the complex photodynamics in the GFP mutants under study, as already seen in Figure 4.1. S_0, S_1, and S_n are the ground, the first, and the n^{th} excited singlet states. The $S_0 \rightarrow S_1$ transition is primed by the pump laser. T is a triplet state, and D is the neutral trap T also called *dark state*, endowed with a much lower brightness than S_1. The rates k_{23} and k_{31} refer to the population (from S_1) and the spontaneous depopulation (to S_0) of the dark state D. The rates k_{24} and k_41 refer to the population (from S_1) and depopulation (to S_0) of the triplet state T. The two schemes differ for the effect of the second laser beam, called probe laser, that pumps the molecules from the trap state onto a higher-energy one, $D*$, from which the chromophore decays either adiabatically to S_0, through S_1 and possibly a photon emission (panel **A**) or diabatically, directly to S_0 (panel **B**).

Previous study on the GFP E222Q, such as Jung et al. [70], showed that in a bulk solution, already at low intensities of the pump beam, a large fraction of the molecules

[1]The main triplet state, common to all the GFP-class proteins, has a population rate $K_{24} = 3 \times 10^5 s^{-1}$ and a lifetime of $50 \mu s$.

are in the neutral conformational state D and that the GFPMut2 molecules do not show any absorption attributable to the neutral chromophore[2].

Referring to Figure 4.1, it is possible to realize the different Quantum Yield, for the standard GFP (S_0, S_1 and $T1$) and for the mutants object of this study (with the possible transition to the dark state D). These yields can be expressed as:

$$\phi_{GFP-std} = \frac{K_R}{K_R + K_{NR} + K_{T1}} \tag{4.1}$$

$$\phi_{GFPMut2} = \frac{K_R}{K_R + K_{NR} + K_{T1} + K_{DARK}} \tag{4.2}$$

where K_{DARK} takes into account the combination of both K_{23} and K_{31}. From these relations it is possible to realize that the Q.Y. of the GFP mutants is lower than that of native GFP. The longer the lifetime of the D state is, the larger the Q.Y. gap will be.
As mentioned, this gap can be voided via the probe illumination of the sample: pumping a depopulation of the D state the Q.Y of the mutants equals the one of the standard GFPs. That is the origin of the fluorescence enhancement concept already introduced in Section 3.3.2.1, the mutants molecules do not actually have a greater Q.Y., but they are characterized by a probe-light tunability of the fluorescence intensity.

Form the mathematical point of view of the 4-level system just outlined the mutant fluorescence Enhancement Ratio introduced in Section 3.3.2.1, can be calculated as

$$ER = \frac{\phi_{GFP-std}}{\phi_{GFPMut2}} \tag{4.3}$$

whereas the previously called Activation/Deactivation Times (see Section 3.3.2) represents the characteristic lifetime of the population and depopulation of the neutral trap state D.

As already mentioned before there is a dependance of the E.R. on physical properties of the chromophores surrounding such as pH and viscosity.
The explanation of the pH dependency of the E.R. is due to the different population ratio between the neutral and anionic state that can be easily understood as dependent on the electrostatic condition of the solution as well as the medium containing the chromophore molecule. On the other end the dependency on the viscosity can be explained in term of molecule mobility and fluorescence saturation effects.

[2]For future references along this text, referring to a generic GFPMut2 molecule, the terminologies *being in a neutral conformational state* and *being in / populating the dark state* are to be intended as, and are in fact, synonymous!

In the following Sections a characterization of the dependency of both the Enhancement Ratio and the Activation/Deactivation Times will be given for the two mutants under study.

For future references along the text, the standard GFP values of the rates (for the processes not regarding the D state) will be used, particularly in the simulative Section 4.2.1, as known from literature, for example in Jung et al. [71], [72], and shown in Table 4.1.

k_{24}	0.3×10^6 [Hz]
k_{41}	2×10^4 [Hz]
k_{21}^{rad}	0.4×10^9 [Hz]
k_{21}^{nrad}	0.343×10^9 [Hz]

TABLE 4.1: Rate constants for E222Q mutant of GFP.

In the simulation, reported in the next Sections, we have also assumed (Blab et al. [73] and [74]): $\sigma_{TPE} \cong 3 \cdot 10^{-49} cm^4$, $w_{xy} = 0.66\mu$m and $w_z = 1.55\mu$m.

4.1.2 Enhancement Ratio Characterization

As previously described by Eggeling et al. [75], the anionic emission of the GFP mutants under study, increases linearly with excitation intensity and reaches a saturation plateau at high excitation intensity values, both under the pump beam only and *pump and probe* beam irradiation.
This behavior can be described by the function[75]:

$$\langle F \rangle = F_0 + \Delta F \left(\frac{I}{I_{sat} + I} \right) \tag{4.4}$$

where F_0 is the fluorescence measured at excitation intensity $I = 0$ and ΔF is the maximum fluorescence increase observed. A characterization of this behavior for E222Q mutant has already been performed by our group and can be found in Figure 1 of [2].

4.1.2.1 E222Q

The characterization of the E.R. dependency on **pH** has already been performed by Quercioli et al. [2], but, as sanity check, we report here the same measurement repeated in order to validate the new experimental method and optical setup used in this study.
The following measurements have been performed on a 100nM GFPMut2 solution and the fluorescence signal has been acquired and averaged both for pump only and *pump and probe* excitation condition.
From the data reported in Figure 4.2 we can observe the fact that the E.R. is higher for low pump intensity[3] and that the trend E.R. vs. pH is confirmed to be the same reported by Quercioli et al. [2] in Figure 2.

On the E222Q mutant a second characterization has been performed analyzing the trend of the E.R. as a function of the **viscosity** of the solution.
The same measurements have been performed varying the glycerol concentration in the solution in order to obtain a scale of viscosity between 1 and 18 times the water viscosity[4].
This is obtained, as explained in detail by Cheng [76], with a mass concentration of glycerol in solution between 0 and 70%.
The data, reported in Figure 4.3, show an increase of the the ER with the rise of the viscosity in the solution. This fact may be explained by a different probability for the native cis-trans conformational transition of the chromophore: if the neutral state is more populated it is straightforward the reason of an higher E.R.

[3] Whereas is basically not dependent on the probe excitation intensity
[4] This are the classical viscosity condition it is possible to found in a cellular environment

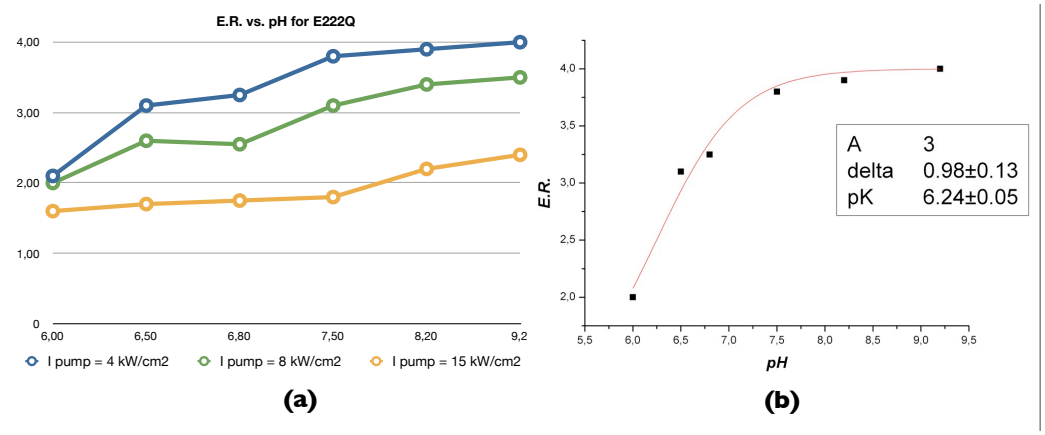

FIGURE 4.2: E.R. vs. pH characterization for E222Q mutant. In Panel **(a)** it is possible to realize the fluorescence saturation effect on the E.R.: the trend vs pH is the same but the enhancement effect lowers increasing the pump power. In Panel **(b)** the curve for $I_{pump} = 4\text{kW/cm}^2$ have been fitted with the sigmoid function[2] $E.R. = 1 + A/(1 + 10^{(-pH+pK)/\delta})$ obtaining fitting value completely comparable with the ones obtained by Quercioli et al.: $pK = 6.24 \pm 0.05$ and $\delta = 0.98 \pm 0.13$ vs. the value reported in the literature of $pK = 6.50 \pm 0.10$ and $\delta = 1.1 \pm 0.13$.

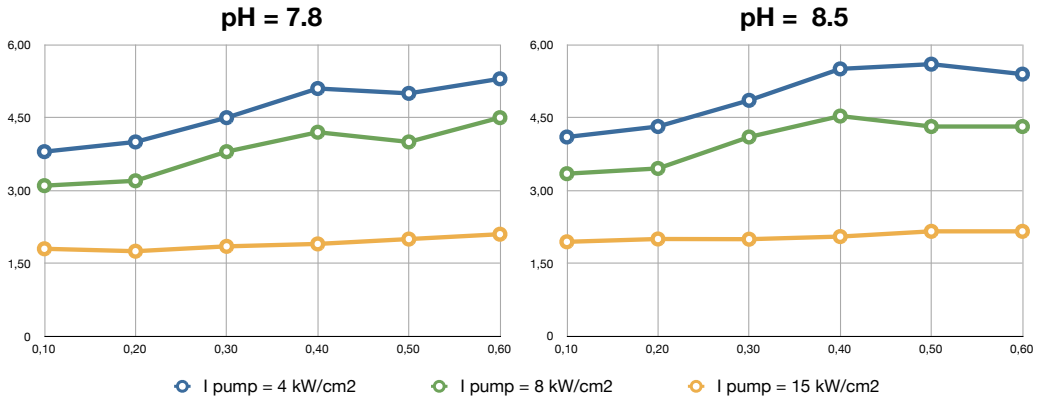

FIGURE 4.3: E.R. vs. viscosity characterization for E222Q mutant. The data, acquired with a $I_{pump} = 4\text{kW/cm}^2$ excitation show that for both pH values there is a sub linear increment of the E.R. with the viscosity of the solution.

4.1.2.2 Mut2GQ

A full characterization of the fluorescence saturation behavior of this new mutant has been done, and the main results are reported in Figure 4.4 and commented in the caption.

The characterization of the E.R. as a function of pH has been carried out on this mutant and the raw data are presented in Figure 4.5. From the results of the characterization, shown in Figure 4.6, it is possible to obtain two important information:

- The E.R. trend as a function of pH for Mut2GQ, is not monotone as in the case of E222Q mutant, but has a peak for neutral pH. E.R. values are also much higher

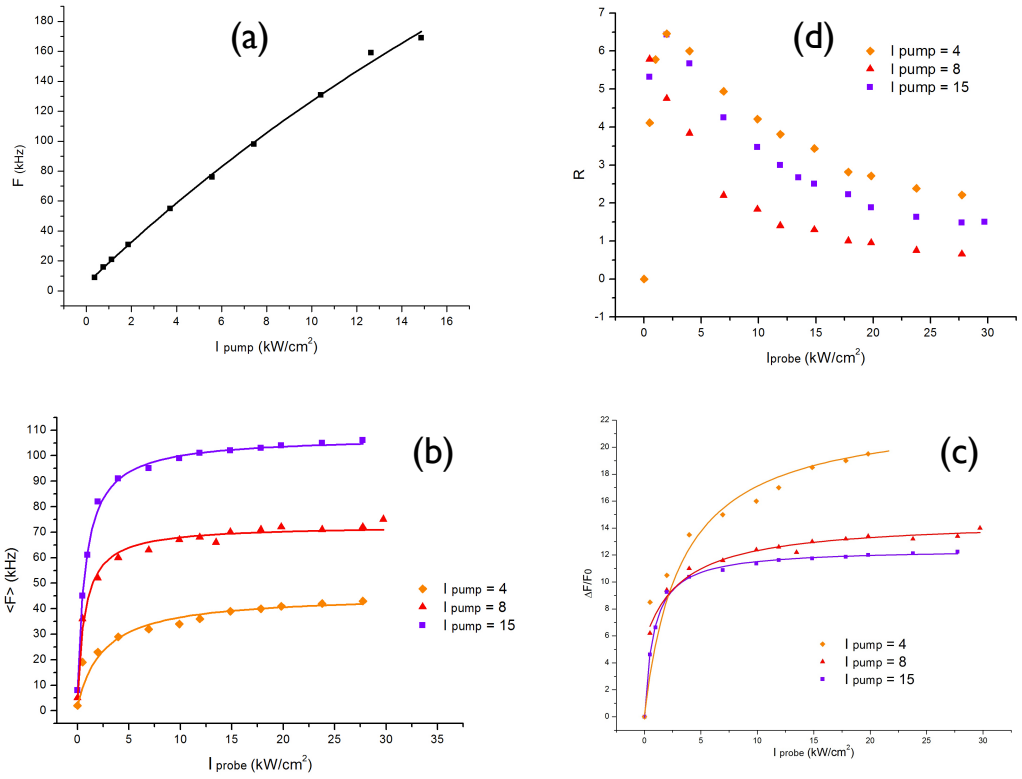

FIGURE 4.4: Mut2GQ fluorescence saturation characterization. In Panel **(a)** the trend of the fluorescence signal is shown as a function of the pump power in the case of no photoinduced fluorescence enhancement: the behavior is similar to that of E222Q mutant [2]. In Panel **(b)**: the saturation curve of the fluorescence emission of Mut2GQ at pH 7.5 versus the probe beam (420 nm) intensity for various excitation power (488nm). Solid line: best fit of Equation 4.4. In Panel **(c)**: the trend of the enhancement ratio as a function of the probe intensity; the trend follows the same of the case of only pump excitation and reach the plateau for the same value of I_{probe}. In Panel **(d)**: relative fluorescence enhancement, $\Delta F/F_0$, versus the probe intensity for various pump intensity ad derived from the data fitting. The intensity in the legends are expressed in kW/cm^2.

than the one obtainable in E222Q mutant: this can be explained in a higher population of the neutra conformational state D at standard condition (Figure 4.6(A)).

- The E.R. for Mut2GQ is practically not dependent on the probe excitation intensity (Figure 4.6(B)), in accord with the E222Q behaviour.

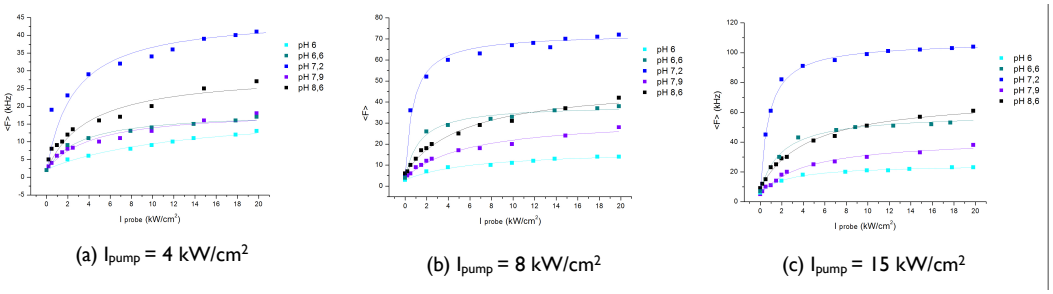

FIGURE 4.5: E.R. vs pH for Mut2GQ mutant: raw data.

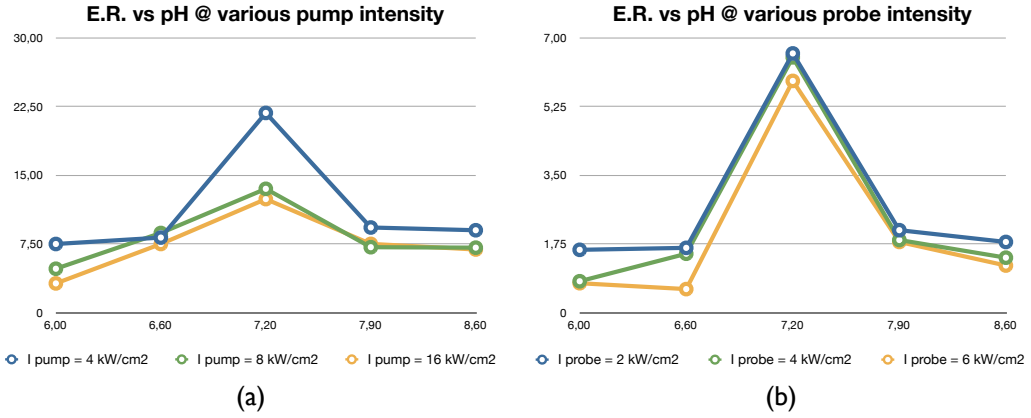

FIGURE 4.6: E.R. vs pH for Mut2GQ mutant. Panel **(a)**: the E.R. of Mut2GQ has higher values with respect to the E222Q mutant, but for this mutant the teend is not monotone and there is a peak of the E.R. at neutral pH. In Panel **(b)** it is possible to realize how the probe excitation intensity does not influences the E.R. (for high pump intensity). Measure taken with $I_{pump} = 20\text{kW/cm}^2$.

4.1.3 FCS Population/De-Population Times Measurements

The Population/De-Population times have been introduced previously in the text (see Section 3.3.2) and as outlined in Section 3.3.2.1 can be measured by FCS measurements with pump + modulated probe excitation.

As mentioned before, theoretically, from such FCS analysis two times should be emerge representing respectively the inverse of the rate of the population and de-population process of the dark state D; this is exactly what has been found on E222Q mutant [2]. On Mut2GQ, though, what as been found (as will be reported in the next Section) is a 3-time dynamics suggesting that there is probably a third process, yet to be investigated, occurring on a faster timescale, that overlaps the standard D-in/D-out dynamics.

For the characterization of these times for E222Q mutant we refer to the work of Quercioli et al. 2010 [2], we hereby only cite the time scale of these lifetimes being between 1-40ms.

4.1.3.1 Mut2GQ

Dependency of I_{pump} The collected data, resumed in Table 4.2 and represented in Figure 4.7, show a increment on the average characteristic time of the photodynamics process, $\langle\tau\rangle$. This can be easily explained by taking into account the saturation effect of the fluorescence phenomena: higher pump power mean more excited molecule that may end in populating the neutral trap state D (see Figure 4.1 for references). Larger population in the D state means longer depopulation times once the probe beam is switched on.

$I_{pump}(kW/cm^2)$	f_1	f_2	f_3	$\langle\tau\rangle(ms)$
4	0,32 ± 0,006	0,16 ± 0,01	0,52 ± 0,02	180 ± 5
8	0,34 ± 0,006	0,33 ± 0,01	0,33 ± 0,02	195 ± 5
15	0,4 ± 0,008	0,38 ± 0,01	0,22 ± 0,02	229 ± 6

TABLE 4.2: Best fit parameters for $G(0,\nu)$ at various I_{pump} for a pH 7,9 solution sample. (see Figure 4.7).

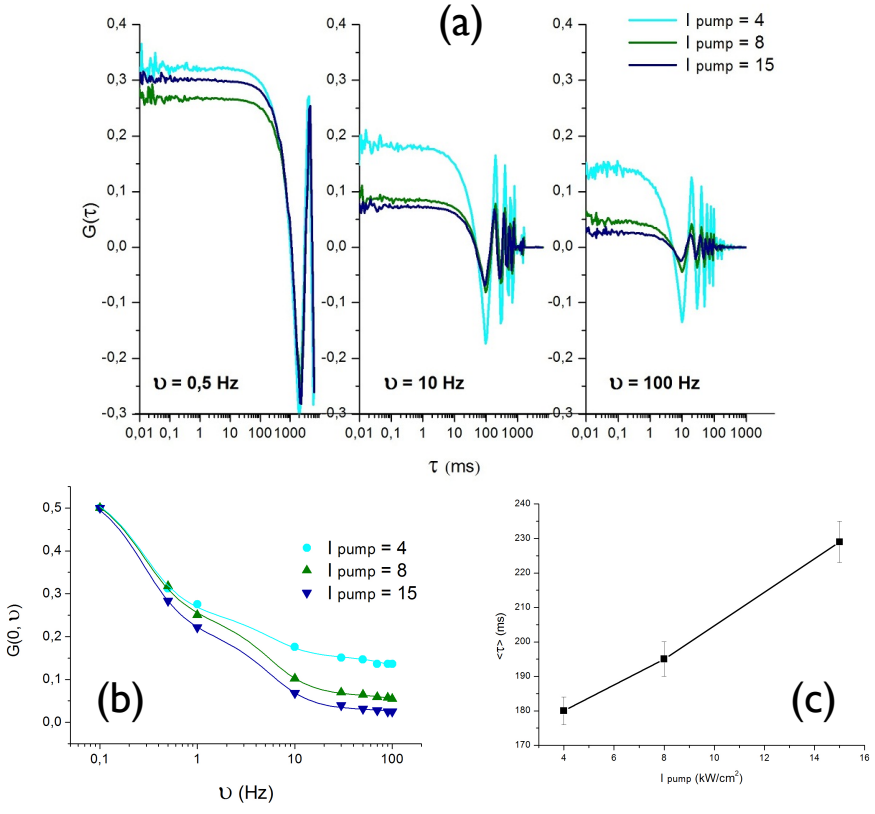

FIGURE 4.7: .

Dependency of I_{probe} Also in this case, the data trend, resumed in Table 4.2 and represented in Figure 4.7, can be easily explained by the observation of the energy level scheme of Figure 4.1. The higher probe beam power, increases the probability for the $D \rightarrow D*$ transitions, thus quickening the depopulation process of the dark state.

$I_{pump}(kW/cm^2)$	f_1	f_2	f_3	$\langle\tau\rangle(ms)$
4	0,44 ± 0,01	0,35 ± 0,01	0,21 ± 0,03	178 ± 5
8	0,42 ± 0,01	0,28 ± 0,01	0,3 ± 0,02	168 ± 6
13	0,31 ± 0,01	0,28 ± 0,01	0,4 ± 0,02	126 ± 6
20	0,25 ± 0,01	0,24 ± 0,01	0,5 ± 0,02	102 ± 6

TABLE 4.3: Best fit parameters for $G(0,\nu)$ at various I_{probe} for a pH 7,9 solution sample. (see Figure 4.8).

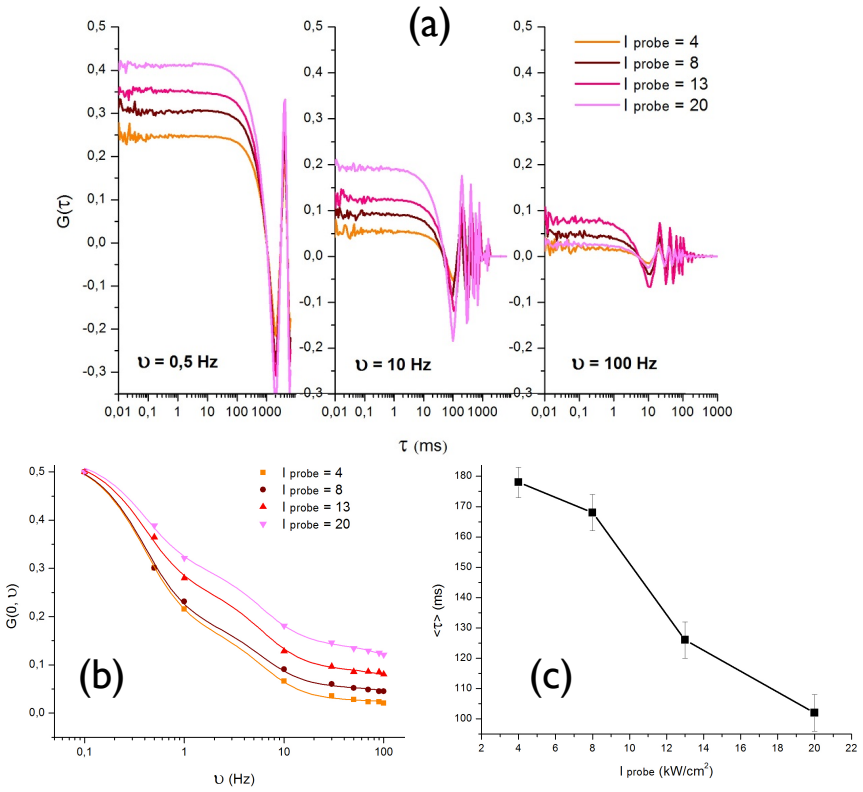

FIGURE 4.8: .

Dependency on pH The data, collected in Table ?? and 4.5 and represented in Figure 4.9, about the dependency of the photoactive times variation as a function of pH show two factors that are worth of been pointed out:

- The behavior of the average time $\langle\tau\rangle$ perfectly mimics the trend for the E.R. showing a maximum for neutral value of the pH.
- On the other end considering the trend of the single time component in the fit, differently with what was observed or the previous case it is possible to identify a monotone trend for one of the times, being an important information on future study of this mutant's dynamics.

pH	$\tau_1(ms)$	f_1	$\tau_2(ms)$	f_2
6	460 ± 156	0,15 ± 0,02	22 ± 4	0,38 ± 0,04
6,6	485 ± 92	0,29 ± 0,02	16 ± 4	0,27 ± 0,04
7,2	611 ± 98	0,28 ± 0,03	53 ± 11	0,3 ± 0,03
7,9	674 ± 171	0,19 ± 0,01	21 ± 4	0,4 ± 0,04
8,6	1000 ± 385	0,08 ± 0,01	21 ± 3	0,36 ± 0,03

TABLE 4.4: Best fit parameters for $G(0,\nu)$ at various pH (1/2). (see Figure 4.9).

pH	$\tau_3(ms)$	f_3	$\langle\tau\rangle(ms)$
6	1,5 ± 0,3	0,47 ± 0,06	79 ± 25
6,6	1,3 ± 0,3	0,44 ± 0,06	146 ± 28
7,2	1,1 ± 0,3	0,41 ± 0,06	189 ± 33
7,9	1,6 ± 0,4	0,43 ± 0,05	136 ± 33
8,6	1,3 ± 0,02	0,55 ± 0,04	94 ± 32

TABLE 4.5: Best fit parameters for $G(0,\nu)$ at various pH (2/2). (see Figure 4.9).

4.1.4 Experimental Results and Limitation

From the experimental characterization of the GFP mutants, carried out by means both of spectroscopic and FCS measurements, we were able to characterize the behavior of photodynamics characteristics of the chromophore as function of physical characteristics of the surrounding of the fluorescent molecules.
In particular the E222Q mutant shows a monotone trend of the E.R. with the increase of both the pH and the viscosity of the solution. The Mut2GQ mutant, on the other hand, shows a peaked trend, with peak value at neutral value for pH, both for the E.R. and the population / de-populations times. Worth noting are also the longer values of the lifetimes for the GQ mutant with respect to the E222Q.

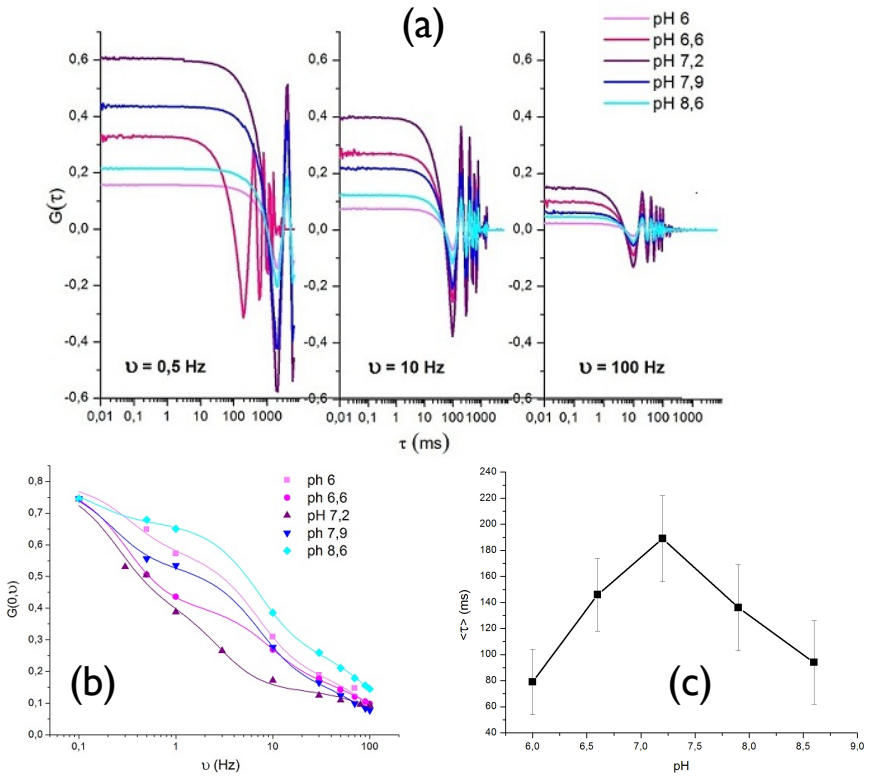

FIGURE 4.9: .

It is, however, vital to point out that the experimental study of such fluorescent dyes is wildly complicated by the coupling, in the FCS AC, of the diffusive component due to the Brownian motion and the *in-and-out* dynamics of the neutral trap state D characteristic of these GFP mutants; this is due to the overlap of the characteristic process times of the two phenomena ($\tau_D \cong \langle\tau\rangle$).

For this reason, a joint mathematical-simulative model has been developed in order to decouple the two physical phenomena and to allow a better knowledge of the process rate for the kind of photoactive chromophores under study here. The model will be describe in the following Sections of this Chapter.

4.2 Decoupling the Brownian Dynamics and the Photodynamics: a Simulative Approach

Presented in this section an analytical and simulative study of the effect of the coupling between the classical brownian diffusion and the photo-triggered fluorescence fluctuations on the FCS ACF, $g(\tau)$.
The analytical study, also compared to the results of Monte Carlo-Brownian Dynamics simulations, indicates that the effect on the retrieved fraction of dark molecules scales as the square root of the ratio between the diffusion and the dark state relaxation times. The numerical simulations and the mathematical model, will be then applied to experimental data collected on the E222Q mutant.

4.2.1 Simulation Algorithm Structure

As discussed in Section 4.1.1, the system simulated here is a dilute solution of globular proteins, each endowed with a chromophore with a complex photodynamics characterized by at least two excited states with different brightness values. The brightest excited state has a lifetime in the nanosecond time scale while the photoactivation process, related to the population/depletion of the dark state D, may occur on a wide time range (fractions of a second). The schemes reported in Figure 4.10(A) and (B) propose two possible model schemes that describe various features of the spectroscopic properties of FPs (see Section 3.3) and can be used for computational purposes for the $\gamma_2 \gg k_{32}$ approximation as in Panel (C) and (D).

In order to simulate the output of the FCS experiment we developed a mixed Brownian dynamics - Monte Carlo algorithm (**Daglio, S.C.** et al. [3]). In this algorithm three steps are taken into account: the molecular brownian diffusion, the photodynamics of the particular chromophore, possibly coupled to the diffusion, and the calculation of the Auto-Correlation Function (ACF) of the fluorescence fluctuations. For this reason the simulation model implemented in the code is organized on three different time scales (as suggested by [77]):

- $dt \cong 20 - 200ns$, being the basic time step associated to the Brownian Diffusion (BD) process;
- $dT \cong 20ns$, the basic time step for the photodynamics (PD);
- $\tau = 200ns$, representing the minimum lag time in the ACF computation.

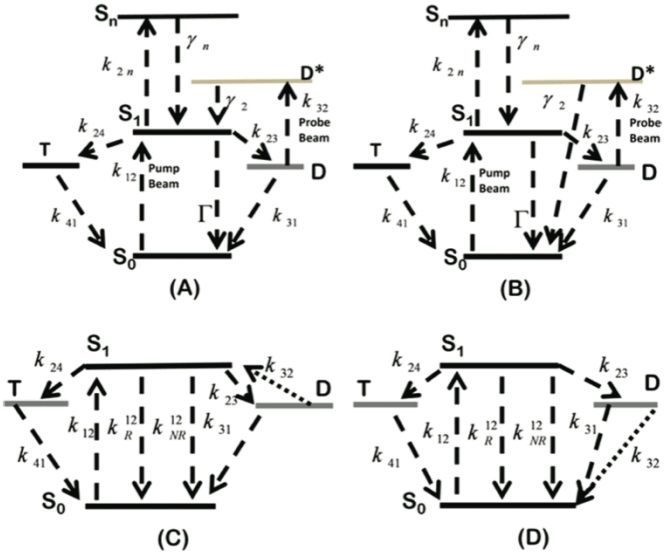

FIGURE 4.10: Examples of two energy diagrams that may describe part of the complex photodynamics in the GFP mutants under study, as already seen in Figure 4.1. S_0, S_1, and S_n are the ground, the first, and the n^{th} excited singlet states. The $S_0 \rightarrow S_1$ transition is primed by the pump laser. T is a triplet state, and D is the neutral *dark state* D also called trap state, endowed with a much lower brightness than S_1. The rates k_{23} and k_{31} refer to the population (from S_1) and the spontaneous depopulation (to S_0) of the dark state D. The rates k_{24} and k_41 refer to the population (from S_1) and depopulation (to S_0) of the triplet state T. The two schemes differ for the effect of the second laser beam, called probe laser, that pumps the molecules from the trap state onto a higher-energy one, $D*$, from which the chromophore decays either adiabatically to S_0, through S_1 and possibly a photon emission (panel **A**) or diabatically, directly to S_0 (panel **B**). The excitation rates of the chromophore under the pump (k_{12}) and probe (k_{32}) beams are related to the corresponding intensities cross sections, σ_{12} and σ_{32}, by $k_{12} = \sigma_{12} I_{pump}$ and $k_{32} = \sigma_{32} Iprobe$.
Panels **C** and **D** report the simplified versions (for $\gamma_2 \gg k_{32}$) of the energy diagrams that are used for the analytical development (as well as the simulation structure): k_R^{21} and k_{NR}^{21} are the radiative and non radiative relaxation rates from the first excited state($\Gamma = k_R^{21} + k_{NR}^{21}$).

The Brownian dynamic propagator, implemented according to [78] and **??**, operates every time-step whose duration is multiple of dt, and the photodynamics algorithm is implemented every dT-multiple steps. The ACF calculation is called at the end of the whole simulation with a lag time that is a multiple of τ.

The proteins are simulated as single spheres whose motion satisfies the Langevin equation (see [79]). The choice of the PD time scale, $dT = 20ns$, much longer than the singlet excited state lifetime, allows to safely assume that in each PD step all the molecules in an excited state, decay to the ground state through one of the possible de-excitation path reported in Figure 4.10.

As pointed out by Ermak and McCammon [80], the BD time step dt must be larger than the relaxation time of the velocity autocorrelation function,

$$dt \gg \frac{m \cdot \Delta}{KT} \tag{4.5}$$

where m and Δ are, respectively the mass and the diffusion coefficient of the Brownian-moving particle. In the case of GFP proteins (m=4.4668$\times 10^{-23}$Kg, $\Delta \cong 100\times 10^{-12}$m^2/sec) the time threshold is at $dt \cong 1$ ps, thus validating our choices of dt.

At the same time, the BD time step should be small enough to avoid changes in the system energy larger than the thermal energy K_BT. This is an issue when inter-particle interactions must be taken into account. In the present case the effect of the hard sphere repulsion between the proteins on the dynamics is expected to negligible due to the very low volume fraction of the solution (ideal solution approximation [5]). Hence, in the present case, the upper limit on the BD simulation step, dt, can then be relaxed[6].

4.2.1.1 Brownian Diffusion

The initial positions for the protein set is generated with an uniform distribution inside the simulation box using the `ran2()` routine[7] from Numerical Recipes[81]. The three dimensional Brownian motion of the particles were implemented using the approximation of the solution of the Langevin equation suggested in[80] [82]. At each time step dt, the three coordinates of all the particles evolve as in the following relation:

$$x_i(t+dt) = x_i(t) + \sqrt{2D \cdot dt}\,\Gamma \tag{4.6}$$

where Γ is a normally distributed (with unitary variance) random number, obtained using `gasdev()` and `ran2()`routines[81].

[5] for molecule molar concentration C = 1 nM and protein radius $\cong$ 2 nm, the volume fraction is $\phi \cong 10^{-8}$

[6] In order to check this hypothesis an alternative routine has been developed that models the same diffusion behavior and that avoids superposition between molecules by performing a double *for* cycle evaluating, for every time step, the relative position of all the molecules and moving again those which overlap until no superposition occurs. Results of test simulations run with this code indicate that for a standard 20 s simulation (10^8 steps, about 100 molecules at a concentration of 2nM) the number of superpositions was typically $\cong$ 0.01%, whereas the CPU run time increased by a factor 10 (due to the N^2-scaling *for* cycle). Hence, the conclusion that the correction for the *ideal solution* approximation was not worth the CPU time required.

[7] The routine is void called 10^6 times before starting to use it inside the simulation: in this way there is a fair certainty of having lost every possible correlation due to the random generator seed.

Periodic Boundary Conditions (PBC),

$$\begin{aligned} x_i^{PBC}(t+dt) &= \left[\left(x_i^{PBC}(t+dt)+\frac{L_x}{2}\right) \quad mod \quad L_x\right] \quad -\frac{L_x}{2} \\ y_i^{PBC}(t+dt) &= \left[\left(y_i^{PBC}(t+dt)+\frac{L_y}{2}\right) \quad mod \quad L_y\right] \quad -\frac{L_y}{2} \\ z_i^{PBC}(t+dt) &= \left[\left(z_i^{PBC}(t+dt)+\frac{L_z}{2}\right) \quad mod \quad L_z\right] \quad -\frac{L_z}{2} \end{aligned} \tag{4.7}$$

were implemented on a volume $L_xL_yL_z$ in order to simulate the bulk solution condition with molar concentration of the order of 1-10 nM. The box extended in the volume $[-L_\alpha/2, L_\alpha/2]$ for $\alpha = x, y, z$, and the size of the box was chosen to reproduce correctly the diffusive part of the ACF as discussed later and in Appendix B. In particular for 3D Gaussian distribution, a beam waist in the range $0.4 < w_{xy} < 0.7\mu m$ ($w_z = 2.5w_{xy}$) and under two-photon excitation, a good reproducibility of the ACF amplitude (<3% in the molecule concentration) is found for a box size $L_xL_yL_z = 3 \times 3 \times 15\mu m^3$.

4.2.1.2 Photodynamics

The simulation algorithm refers to the simplified energy diagrams reported in Panel (C) and (D) of Figure 4.10.
As reported in Figure 4.10 (C) and (D), there is no reason to implement explicitly the excited level D^*, to allow for the photo-switching process, as long as we operate in the $\gamma_2 \gg k_{32}$ approximation. In this case, in fact, since the only possible transition is $D^* \rightarrow S_1$, the chromophore can be thought to transit directly from D back to S_1, when irradiated by the probe laser beam.

Inside the simulation algorithm the photoactive state of each diffusing molecule is labeled with an integer variable, the Optical Label (OL) flag. At the beginning of the simulation all the OL labels are initialized to zero, indicating that all the molecules starts their PD history in S_0. At each PD time step dT, a Monte Carlo (MC) test is performed and the OL flag switches to values that characterize the states S_1 (OL=1), T_1 (OL=2) and D (OL=3). The transition probability (for every possible transition in Figure 4.10 C and D) is tested against a uniform distributed random number, according to a standard MC test. This allows to simulate the PD on a single chromophore and implement it within the Langevin formalism adopted to solve the diffusion motion. Alternative approaches that work within the Smoluchowski framework [79], follow the well known Gillespie algorithm for the simulation of stochastic chemical reactions Gillespie [83].

For every time step dT, if the OL flag is 0, a MC test is performed on the $S_0 \rightarrow S_1$ transition. In order to minimize the CPU time, as discussed in Appendix B, it is computationally convenient to simulate the spatial dependence of the excitation probability with a 3D Gaussian distribution of the exciting beam:

$$k_{12}^{nPE,G3D} = k_{12}[\rho_{G3D}(x,y,z)]^n \tag{4.8}$$

$$\rho_{G3D}(x,y,z) = \frac{(\pi)^{-3/2}}{\omega_0^2 z_0} \exp\Big[-2\frac{(x^2+y^2)}{\omega_0^2} - 2\frac{(z^2)}{z_0^2}\Big]$$

The excitation rate is computed as $k_{12} = \sigma_{nPE} I_{pump}^n$. For the probe beam excitation, a similar algorithm is assumed with $k_{32} = \sigma_{32}^{OPE} I_{probe}$[8]. Other excitation modes, discussed in Appendix B, do not imply substantial changes in the simulative results. The parameters ω_0 and z_0 depend on the objective numerical aperture, the laser wavelength and the confocal optics, as already mentioned in the previous Chapters.
Each chromophore excitation probability for the $S_0 \rightarrow S_1$ transition is $P_{12} = k_{12}dT$ and the transition is accepted (OL=1) if a random number ξ_1[9] satisfies the condition $\xi_1 \leq P_{12}$. In this case the chromophore OL flag is switched to 1.

The chromophore on the S_1 state (OL=1) may then take, already inside the very same PD step of the simulation, different de-excitation paths:

- *Radiative and non radiative relaxation to* S_0 - In this case the OL flag is reset to 0. The total $S_1 \rightarrow S_0$ de-excitation rate, Γ, in Figure 4.10(C) and (D), is given by the sum of the radiative, k_{12}^R , and non radiative, k_{12}^{NR}, decay rates. When the radiative pathway is sampled the emitted photon adds into the Fluorescence Time Vector (FTV) counter that provides the fluorescence time trace used for the ACF computation.

- *Intersystem crossing to* T *or conversion to* D - In these cases the OL flag switches to 2 and 3 respectively. The rates k_{23} and k_{24} refer to the $S_1 \rightarrow T$ and the $S_1 \rightarrow D$ transition, respectively, and $k_{tot} = \Gamma + k_{23} + k_{24}$. The T state is a triplet state from which the molecule relaxes to S_0, mainly through non radiative processes. These relaxation modes produce exponential components in the ACFs decays with characteristic times of the order of few microseconds (see Figure 2.14 and [84]). The D state is the dark state involved in the photoswitching.

[8] As already mentioned in the previous Chapters whereas the excitation $S_0 \rightarrow S_1$ may be obtained with multi-photon excitation technique (nPE), for the GFP mutant under study, the probe activation occurs only for One Photon Excitation

[9] belonging to the uniform distribution in the $[0,1)$ domain

If ξ_2 is a uniformly distributed random number, the MC test can be summarized as follows:

$$\begin{aligned} if \quad \xi_2 \in \left[0; k_{12}^R/k_{tot}\right] \quad &: \underbrace{S_1 \rightarrow S_0}_{radiative} \\ if \quad \xi_2 \in \left(k_{12}^R/k_{tot}; (k_{12}^R + k_{12}^{NR})/k_{tot}\right] \quad &: \underbrace{S_1 \rightarrow S_0}_{non-radiative} \\ if \quad \xi_2 \in \left((k_{12}^R + k_{12}^{NR})/k_{tot}; (k_{12}^R + k_{12}^{NR} + k_{23}/k_{tot}\right] \quad &: S_1 \rightarrow T \\ if \quad \xi_2 \in \left((k_{12}^R + k_{12}^{NR} + k_{23})/k_{tot}; 1\right] \quad &: S_1 \rightarrow D \end{aligned} \tag{4.9}$$

We finally need to consider the decay paths from T and D according to:

$$\begin{aligned} if \quad \left\{OL = 2 \quad and \quad \xi_3 \in \left[0; dTk_{31}\right]\right\} \quad &: T_1 \rightarrow S_0 \quad and \quad OL = 0 \\ if \quad \left\{OL = 3 \quad and \quad \xi_3 \in \left[0; dTk_{41}\right]\right\} \quad &: D \rightarrow S_0 \quad and \quad OL = 0 \end{aligned} \tag{4.10}$$

where ξ_3 is a third independent uniformly distributed random number in $[0, 1]$.

So far we have considered only the effect of the pump laser beam. Since we want to simulate photoswitching induced by a second beam (with intensity I_{probe}), we need to consider additional paths activated by the probe beam. When OL = 3, a fourth MC test is performed depending on the probe laser intensity.
For the scheme in Panel C (Figure 4.10), the probability that the second beam stimulates the $D \rightarrow S_1$ transition is computed as $P_{32} = \sigma_{32} I_{probe} dT$ and compared to a fourth uniformly distributed random number, ξ_4. If $P_{32} \leq \xi_4$, the protein OL flag is reset to 1, meaning that in the next photodynamic step the molecule may emit a photon with a probability k_{12}^R/k_{tot}.
For the scheme in Panel D (Figure 4.10), instead, the probability P_{32} is used to ascertain whether the molecule undergoes a $D \rightarrow S_0$ transition, and OL is set to 0: in this case, no photon emission may occur, and the transition is *diabatic* [3].

Since the starting configuration corresponds to all molecules in the ground state, the electronic states of the molecules must first reach a dynamical equilibrium. This was obtained by running 2s of simulation: after this equilibration time, the simulations were run for approximately 80s.

For the simulations of the fluorescence ACFs under dual (pump and probe) beam excitation and with a square modulation of the probe beam (at frequency ν_L), we evaluate for every time step t the factor $N = t\nu_L$ and set $I_{probe} = 0$ only if $N - \text{round}(N) < 0.5$.

4.2.1.3 AutoCorrelation Function Calculation

The autocorrelation of the fluctuation of the fluorescence signal is computed on the data stored in the Fluorescence Time Vector ($F(t)$), according to the following algorithm:

$$\begin{aligned} G(k\tau) &= \frac{dt}{\langle F(t)\rangle^2} \sum_{t=0}^{(TST)-k\tau} \frac{(F(t) - \langle F(t)\rangle)(F(t+k\tau) - \langle F(t)\rangle)}{(TST - k\tau)} \\ \langle F(t)\rangle &= \frac{dt}{TST} \sum_{t=0}^{TST} F(t) \end{aligned} \tag{4.11}$$

where TST indicates the Total Simulation Time. The lag times of the ACF are computed as in the ALV 5000E correlator card[10] (ALV, Langen, D). The first (shortest) 10 lag times are distributed linearly whereas the following ones are geometrically distributed so that in a logarithmic scale they would appear as uniformly distributed. The ACF calculation routine is called after the end of the dynamics cycle.

The mixed BD-MC algorithm was first extensively tested for reproducing the known analytical shape and amplitude of the fluorescence fluctuation ACF. For the case of fluorescence fluctuations induced only by diffusion the simulations indicate that by choosing the TPE excitation mode with a 3D Gaussian beam shape (Equation 4.8) and the simulation box volume = 135 μm^3 we can correctly reproduce the ACF decay, and an analytical fitting function for the fluorescence ACF can be used. The more realistic Gaussian-Lorentzian shape, on the contrary, would imply a non-analytical fitting function and the use of a much larger simulation box due to the slow axial decay of the Lorentzian component of the beam shape. No substantial change in the main results of simulations discussed hereafter is expected for a different excitation mode and laser beam profile (see Appendix B).

[10] The one in use in our laboratory.

4.2.2 BD-PD Coupling Mathematical Model and Discussion

This Section is organized as follows: the case of coupling be- tween diffusion and photodynamics fluctuations is treated analytically for the simplified case of spherical excitation volume, and a simple scaling law is obtained. To verify the analytical results, we discuss a graphical analysis of the ACFs that allows us to estimate the amount of diffusion/photodynamics coupling. Finally, we validate both the simulation outputs and the graphical analysis of the ACFs on experimental data on the E222Q.

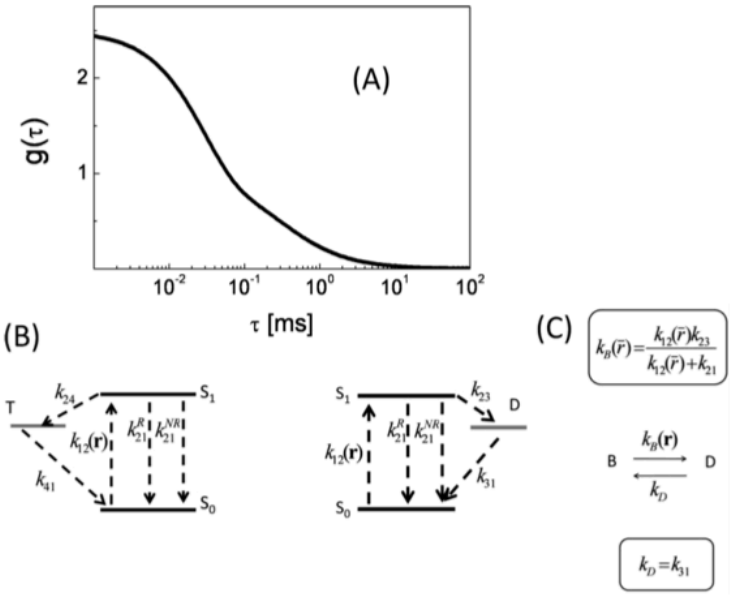

FIGURE 4.11: Typical short-lived triplet state ACF predicted from Equation 4.12, $\tau_{diff}^{(xy)} = 300\mu$s, $\tau_{diff}^{(z)} = 3000\mu$s, $f_{dark} = 0.6$ and $\tau_{dark} = 30\mu$s. Panel **B**: three-state (S_0-S_1-T) energy diagram scheme that describes the flickering of the fluorescence emission from a single chromophore. The T state is a triplet short-lived dark state. The rate k_{24} is the intersystem crossing rate. Panel **C**: three-state (S_0-S_1-D) energy diagram scheme that describes the trapping of the excited state chromophore in a dark long-lived state D. The bright state, S_1, is resonant with the radiation and is coupled to a dark state, D. The rates between the states are: the position-dependent excitation rate, $k_{12}(\bar{r})$, the radiative k_{21}^R and the non radiative k_{21}^{NR} de-excitation rates, the $S_1 \rightarrow D$ crossing rate, k_{23}, and the de-excitation rate, k_{31}. We sketch also a simplified unimolecular reaction between two states, B (bright) and D (dark), that is equivalent to the three-state model. The equivalent forward and backward reaction rates $k_B(\bar{r})$ and k_D are defined in the text.

4.2.2.1 Diffusive-photodynamics coupling: analytical result for a short lived dark state.

The flickering of the fluorescence emission from a single chromophores implies a resonant bright state, coupled to a generic non fluorescent state.

The resonant bright state can be found in the ground, S_0, and in the excited electronic configuration, S_1.

When the bright-dark state kinetics falls in a frequency range that is higher than the diffusion rates, the non fluorescent state can be identified in the triplet state T. The energy scheme for this case is reported in Figure 4.11(B).
In this case it is possible to decouple the photodynamics and the diffusion process for the computation of the AutoCorrelation Function (ACF) of the fluorescence fluctuations (δF), which is the natural output of Fluorescence Correlation Spectroscopy (FCS) experiments. For the system depicted in Figure 4.11(B), the ACF becomes:[85]

$$\begin{aligned} g(\tau) &= \frac{\langle \delta F(t+\tau)\delta F(t)\rangle_t}{\langle F(t)\rangle_t^2} = \\ &= \underbrace{g(0)\left(1+\frac{\tau}{\tau_{\Delta_{xy}}}\right)^{-1}\left(1+\frac{\tau}{\tau_{\Delta_z}}\right)^{-0.5}}_{g_\Delta(\tau)}\underbrace{\left(1+\frac{T}{1-T}exp\left[-\tau/\tau_T\right]\right)}_{g_{PD}(\tau)} \end{aligned} \tag{4.12}$$

where the diffusion times in the focal plane and along the optical axis are $\tau_{\Delta_{xy}} = \omega_0^2/(8\Delta)$ and $\tau_{\Delta_z} = z_0^2/(8\Delta)$, respectively and the bright to dark kinetics parameters are the relaxation time τ_T and the dark fraction T.
Equation 4.12 is valid only when $\tau_T \ll \tau_{\Delta_{xy}} \leq \tau_{\Delta_z}$: in this case the excitation intensity seen by the chromophore during its photo-dynamic cycle is substantially constant. If we assume that the excitation rate has no spatial dependence, i.e. $k_{12}^{(nPE,G3D)}(x,y,z) = \bar{k}_{12}$, the relaxation time and the triplet fraction are written as (Figure 4.11(B)):

$$\begin{aligned} \tau_T &= \frac{\bar{k}_{12}+k_{21}}{\bar{k}_{12}\left(k_{23}+k_{31}\right)+k_{21}k_{31}} \\ T &= \frac{\bar{k}_{12}k_{23}}{\bar{k}_{12}\left(k_{23}+k_{31}\right)+k_{21}k_{31}} \end{aligned} \tag{4.13}$$

However, in order to describe more realistically the experimental conditions, we should consider the effect of the spatial dependence of the excitation rate, k_{12}, on the triplet relaxation time τ_T and the dark state fraction T. As discussed by Widengren et al. [86] a continuous distribution of exponentials over a range of values of τ_T is more realistic in this case. If the distribution is sufficiently narrow it is possible to perform a spatial

average of τ_T and T (Equations 4.13) over the light intensity distribution ($\rho(x,y,z)$ in Eq.4.8). The photodynamic component of the autocorrelation function results[86]:

$$g_{PD}(\tau) = \left(\frac{\overline{T}_{eff}}{1-\overline{T}_{eq}}\right) \exp\left[-\frac{\overline{\tau}_T^{eff}}{\tau}\right] + 1 \tag{4.14}$$

where $\overline{T}_{eff}$ and $\overline{\tau}_T$ are respectively the spatial average of T and τ_T:

$$\overline{T}_{eq} = \frac{\int \frac{\overline{T}(\bar{r})}{1-\overline{T}(\bar{r})}\rho^2(\bar{r})dV}{\int \frac{\rho^2(\bar{r})}{1-\overline{T}(\bar{r})}dV} \tag{4.15}$$

and

$$\overline{\tau}_T^{eff} = \frac{\int \frac{\overline{T}(\bar{r})}{1-\overline{T}(\bar{r})}\rho^2(\bar{r})\tau_T(\bar{r})dV}{\int \frac{\overline{T}(\bar{r})}{1-\overline{T}(\bar{r})}\rho^2(\bar{r})dV} \tag{4.16}$$

representing the effective photo physical parameters.

In equations 4.15 and 4.16 the spatial dependence of τ_T and T is through the function $\rho(\bar{r})$ (Equation 4.8). The numerical algorithm outlined in the previous Section allows us to recover the effects described by Equations 4.14, 4.15 and 4.16 on the ACF in agreement with previous studies [87].
However, when the dark state is long-lived with respect to the diffusion time, even Equations 4.14, 4.15 and 4.16 cannot describe correctly the experimental data. Additional and more important corrections to Equation 4.12 must then be searched by solving the photodynamics and diffusion equations without the factorization of these two sources of fluctuations. In the next paragraph, we describe a simple model that underlines the significant variables that must be taken into account when dealing with long-lived dark states.

4.2.2.2 Long Lived Dark State

In this case the characteristic of the dark state are more similar to those of the neutral conformational state in GFP mutants (see previous Chapter). The energy scheme in this case is reported in Figure 4.11(C).

For treating this case, we want to derive a closed expression for the dark state population for a simple three-state model (see model in Figure 4.11C) from the solution of the

coupled diffusion/photodynamics equations:

$$\begin{aligned}
\frac{\partial}{\partial t}c_{S_0}(\vec{r},t) &= \Delta\nabla^2 c_{S_0}(\vec{r},t) - k_{12}(\vec{r},t)c_{S_0}(\vec{r},t) + k_{21}c_{S_1}(\vec{r},t) + k_{31}c_D(\vec{r},t) \\
\frac{\partial}{\partial t}c_{S_1}(\vec{r},t) &= \Delta\nabla^2 c_{S_1}(\vec{r},t) + k_{12}(\vec{r},t)c_{S_0}(\vec{r},t) - (k_{21}+k_{23})\,c_{S_1}(\vec{r},t) \\
\frac{\partial}{\partial t}c_D(\vec{r},t) &= \Delta\nabla^2 c_D(\vec{r},t) + k_{23}c_{S_1}(\vec{r},t) - k_{31}c_D(\vec{r},t) \qquad (4.17)
\end{aligned}$$

$$N = c_{S_0} + c_{S_1} + c_D$$

In these equations, we have assumed that the total protein concentration, $C = N/V_{system}$, is conserved (i.e. no photobleaching).
These equations can be approximated (see Appendix A) to a unimolecular chemical kinetics (see Figure 4.11D) in which the state B is the bright state, including both the ground (S_0) and excited (S_1) state ($B = S_0 + S_1$), and the D state is the dark state[11]. The equations for diffusion and photodynamics of the B and D species are then:

$$\begin{aligned}
\frac{\partial c_b(\vec{r},t)}{\partial t} &= \Delta\nabla^2 c_b(\vec{r},t) + k_d c_d(\vec{r},t) - k_b(\vec{r})c_b(\vec{r},t) \\
\frac{\partial c_d(\vec{r},t)}{\partial t} &= \Delta\nabla^2 c_b(\vec{r},t) - k_d c_d(\vec{r},t) + k_b(\vec{r})c_b(\vec{r},t) \qquad (4.18)
\end{aligned}$$

In this equation $k_b(\vec{r})$ indicates the rate constant related to the probability to enter the dark state (or to leave the bright one) and k_d is the one related to the transition from the dark state to the ground state. It must be noted that k_b is not the k_{12} rate reported in the energy diagram of Figure 4.10, for the last one **only** refers to the passage between S_1 and D. The rate k_b refers instead to the rate at which the whole bright state b is depopulated, and must be proportional to the population of S_1 that depends on the singlet lifetime and the irradiating beam intensity. Therefore we expect that k_b has a spatial dependence that is proportional to the excitation beam intensity. An estimate of the average dark state fraction in the presence of coupling between the diffusion and the photodynamics can be obtained from the equilibrium solution of Equations 4.18. By writing $\bar{C} = \bar{c}_b + \bar{c}_d$, the equations can be simplified to:

$$\begin{aligned}
\Delta\nabla^2\bar{c}_d(\vec{r}) - k_d\bar{c}_d(\vec{r}) &+ k_b(\vec{r})(\bar{C} - \bar{c}_d(\vec{r})) = 0 \\
\bar{c}_b(\vec{r}) &= \bar{C} - \bar{c}_d(\vec{r}) \qquad (4.19)
\end{aligned}$$

Due to the proportionality of $k_b(\vec{r})$ to $k_{12}(\vec{r})$, the k_b space dependence is described by the 3D Gaussian beam profile $\rho_{G3D}(\bar{r})$ as reported in Equation (4.8). Numerical

[11] B and C labels will not be reported in capitals in the following passages.

solutions could of course be obtained for other profiles and excitation modes. However we are here interested in deriving a general analytical dependence of the effect of the diffusion/photodynamics coupling on the average dark concentration detected by the ACF measurements and analysis. Hence, we search for an analytical solution in the simplest case in which the excitation volume is assumed spherical:

$$k_b(r) = \begin{cases} 0 & \text{if} \quad \text{r} \geq \text{L}; \\ \bar{k}_b & \text{if} \quad \text{r<L} \end{cases} \tag{4.20}$$

The size L must be chosen to describe the overall dispersion of the light on the excitation volume. Due to the spherical geometry of $k_b = k_b(r)$ we search for a spherically symmetric solution: $\bar{c}(\vec{r}) = \bar{c}(r)$. In spherical coordinates and with the given functional form of $k_b(r)$ (Eq.4.20), Eq. (4.19) becomes:

$$\begin{aligned} \Delta \frac{1}{r^2}\frac{d}{dr}\left[r^2 \frac{d}{dr}\bar{c}_d(r)\right] - k_d \bar{c}_d(r) + \bar{k}_b(\bar{C} - \bar{c}_d(r)) &= 0 \text{ if } r < L \\ \Delta \frac{1}{r^2}\frac{d}{dr}\left[r^2 \frac{d}{dr}\bar{c}_d(r)\right] - k_d \bar{c}_d(r) &= 0 \text{ if r} \geq \text{L} \end{aligned} \tag{4.21}$$

where the expression for the Laplace operator in spherical coordinates had been used. We then solve the equation for $r < L$ and $r > L$ and then set a continuity condition at L both for the concentration and it's derivative. This leads [3] to the functional dependence of the average fraction of dark molecules, $\bar{D}_{eff}$, in the excitation volume on the translational diffusion coefficient (Δ) and the photodynamics time ($\tau_T = 1/(\bar{k_b}+k_d)$). The dependence of $\bar{D}_{eff}$ on these parameters can be computed according to the relation:

$$\bar{D}_{eff} = \frac{\int_0^L d^3\vec{r} c(\vec{r})}{\int_0^L d^3\vec{r}\bar{C}} \tag{4.22}$$

Eq.4.22 allows to cast $\bar{D}_{eff}$ in terms of adimensional quantities, $lL = \sqrt{\frac{\bar{k_b}+k_d}{\Delta}}L \propto \sqrt{\frac{\tau_\Delta}{\tau_T}}$ and $mL = \sqrt{\frac{k_d L^2}{\Delta}} \propto \sqrt{\frac{\tau_\Delta}{\tau_T}(1-T)}$, and of the decoupled dark fraction, $D = \bar{k_b}(\bar{k_b} + k_d)^{-1}$. The connection between the dark fraction of molecules in the excitation volume computed with and without diffusion-photodynamics coupling, is given by a composition of hyperbolic functions:

$$\bar{D}_{eff} = D\left\{1 - \frac{3\left[1+(mL)\right]}{(lL)^2}\left[\frac{(lL)\cosh(lL) - \sinh(lL)}{(mL)\sinh(lL) + (lL)\cosh(lL)}\right]\right\} \tag{4.23}$$

The term in curled parentheses takes into account the coupling effect. The significant variables become mL and lL, where the diffusional time and the dark state rate constant and fraction are mixed together. For τ_Δ comparable to τ_D the correction factor becomes relevant, while for $\frac{\tau_\Delta}{\tau_D} \cong (lL)^2 >> 1$ (Figure 4.12) $\bar{D} \cong D$. It is worth noting that an estimate of the experimental dark fractions can be obtained from the zero lag time limit of the simulated or computed correlation function as $g(0) = [\langle N\rangle (1-D)]^{-1}$, where $\langle N\rangle$ is the average number of proteins in the excitation volume.

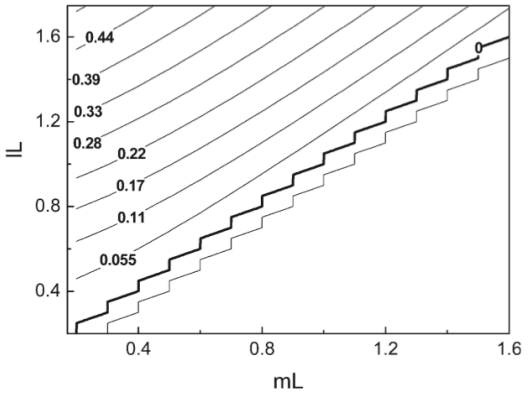

FIGURE 4.12: Contour plot of the correction factor to the dark fraction $\bar{D}_{eff}/D$ in Equation 4.23, due to the diffusion process. Values of lL and mL lower than 1 correspond to a diffusion time shorter than the dark state lifetime. Since $m \leq l$, half of the plot is null. Numbers in the plot indicate the contour levels.

Regarding the effect of the diffusion-photodynamics coupling on the time dependence of the ACF decay in a FCS experiment, is reported in **Daglio, S.C.** et al. that, in the limit of high coupling between the diffusion and the photodynamics processes, it will not be possible any more to discriminate between a diffusion-like hyperbolic decay, due to diffusion, and an exponential decay due to the photodynamics within the ACF decay. All the coupling cases discussed in [3] can be described by the trial function

$$G^{-1}(g(t)) = A(1 - \exp\left[-t/\tau_D\right]) + \frac{t}{\langle\tau\rangle} + \frac{t^2}{2\langle\tau\rangle^2}\sigma_2 \tag{4.24}$$

The exponential growth describes any fast decaying photodynamics component: the amplitude A is related to the dark fraction, $\bar{D}$, by $A = \bar{D}/(1-\bar{D})$.

In order to verify this hypothesis and the prediction given by Eq.4.23 we discuss in the following paragraphs numerical simulations of FCS experiments in the two opposite limits: $\tau_\Delta << \tau_T$ and $\tau_\Delta >> \tau_T$.

4.2.2.3 Numerical Simulation Analysis of the diffusive - photodynamics coupling: short lived dark state.

The mixed BD-MC algorithm was extensively tested for reproducing the known analytical shape and amplitude of the fluorescence fluctuation ACF. For the case of pure diffusive motion with no photodynamics the simulations indicate that by a proper choice of the beam shape and the simulation box size, we can correctly reproduce the ACF decay and also predict known effects on the ACF such as the increase of the ACF diffusive relaxation time at increasing laser intensity, due to the spatially inhomogeneous ground state depletion [86].
On the basis of the discussion reported in Appendix B, we have adopted, in the analysis reported hereafter, a TPE excitation mode with a 3D Gaussian beam shape (Equation 4.8), since in this case the simulation box size can be minimized ($\cong 135\mu m^3$) with respect to the beam waist ω_0 and an analytical fitting function for the fluorescence ACF can be used (Equation 4.12, for no coupling between the diffusive and the photo-dynamics fluctuations). [12]

Short Lifetime Triplet State $S_1 \rightarrow T$ We first test the BD-MC algorithm for the case of decoupled diffusion-photodynamics fluctuations and for a protein of the size of GFP.
In this case, we expect the BD-MC simulations should at least reproduce the effect of the spatial inhomogeneity of I_{pump} on the shape of the ACF decay, as previously reported [86].
We assume in this case a single (pump) excitation beam whose energy is resonant with the $S_0 \rightarrow S_1$ transition and treat explicitly only the transition $S_1 \rightarrow T$ that introduces microsecond scale flickering in the fluorescence signal. The simulation input rates are then chosen according to the estimated values reported in the literature [71] [72] for the the E222Q GFP mutant and reported in Table 4.1.

The TPE cross-section is assumed here $\sigma_{TPE} \cong 3 \cdot 10^{-49} cm^4$ in agreement with reported literature values for GFP mutants [73] [74] and the beam waist are $\omega_0 = 0.66\mu$ m and $z_0 = 1.55\mu$m. The simulations have been performed as a function of the excitation

[12] The more realistic Gaussian-Lorentzian shape, on the contrary, would imply a non analytical fitting function and the use of much larger simulation boxes due to the slow axial decay of the Lorentzian component of the beam shape. No substantial change in the main results of simulations discussed hereafter is expected for a different excitation mode and laser beam profile (see Appendix B).

power (in the range 30 mW - 150 mW) and the fluorescence ACFs, fitted with Equation 4.12, provide the trend of the diffusion times, τ_Δ, the particle number in the excitation volume $\langle N \rangle$, the triplet times, τ_T, and fraction T as a function of the excitation rate. The peak excitation probability per PD step, $dT \cdot k_{12}^{TPE}$ (Eq.4.8), spans the range $6 \times 10^{-3} - 1.5 \times 10^{-1}$ for $dT = 20ns$. Higher values of the excitation power or larger values of dT would imply non negligible secondary absorption probability.

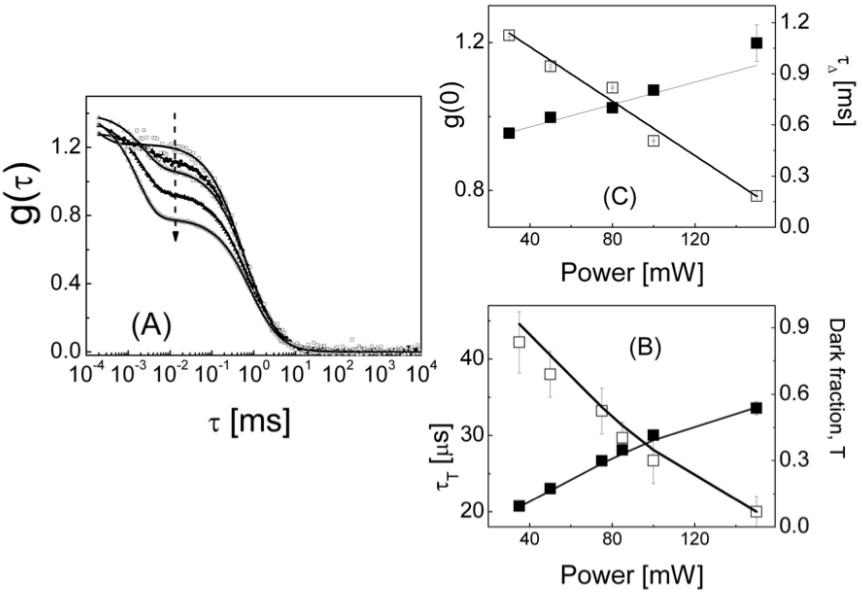

FIGURE 4.13: BD-MC simulation of a triplet state dynamics ACF for GFP (panel A) according to the parameters reported in Table 4.1 as a function of the excitation power (G3D profile and TPE): 30, 50, 75, 85, 100 and 150 mW from top to bottom. The solid lines are the best fit of Equation 4.12. Panel B reports the best fit values of the triplet time, τ_T (opensquares) and the dark fraction (filled squares), T, as a function of the excitation power. The solid lines report the values of these parameters computed according to Equations 4.15 and 4.16. Panel C reports the best fit values of the diffusion time, τ_Δ, and of the zero lag time extrapolation of the ACF, $g(0)$. The solid lines are linear fit curves drawn to guide the eye.

The effect of the triplet dynamics on the ACF shape is evident from Figure 4.12.A .
The fitting parameters of the triplet dynamics component of the ACF are reported in Figure 4.12.B and compared with the estimates that can be computed from Equations 4.15 and 4.16.
The excellent agreement between the computed and the simulated values for these parameters stems for a correct evaluation of the effect of the beam profile on the ACF decay obtained from the simulations. This can be also appreciated qualitatively from the dependence on the excitation power of the diffusion time τ_Δ and the apparent concentration $\gamma/(V_{exc}g(0))$ reported in Figure 4.12.C.
The observed increase in the average number of bright molecules per excitation volume ($\propto 1/g(0)$) and of the best fit diffusion time, is in fact originated by the non linear

dependence of the $\langle S_1(\bar{r},t)\rangle_t$ population on the excitation intensity that induces a deformation of the single excited state population with respect to $\rho^2_{G3D}(\bar{r})$ and results in the increase of the effective size of the beam waist.[86]. These effects have been already investigated both experimentally and theoretically in the literature by Widengren et al. [86] and the simulations performed here can then be taken as a validation of the BD-MC simulation algorithm.

Long Lifetime Dark State and Enhancement Photodynamics $S_1 \rightarrow D$ The case simulated in the previous section corresponds to an almost complete decoupling of the diffusive and the triplet photodynamics, since the triplet and the diffusion times were $\tau_T < 50\mu s$ and $\tau_\Delta \cong 600\mu s$. We pass now to investigate numerically the PD-BD coupling in order to assess the degree of accuracy of the theoretical treatment developed before.

For this case, let's assume the four-state models (S_0-S_1-T-D), such as the one represented in Figure 4.10. Let's also keep the T-involving rates at the values reported in Table 4.1, as we approach the strongly coupled case by varying the population rate of the triplet state, k_{23}, in the range 450 Hz$\leq k_{23} \leq$4.5 MHz while assuming $k_{31} = 1$kHz. We have chosen an average excitation power of 30 mW ($k_{12} = 2.35 \cdot 10^6$ excitations/s) to minimize the effect of the spatial inhomogeneity on the ACF decay [3].
The ACFs obtained from the simulations can be reasonably well force fitted to a simple diffusion ACF decay ($g_{diff}(t)$ in Equation 4.12) for all the simulated cases (Figure 4.14A). The best fit value of the zero lag time ACF, $g(0)$, can be used to measure the effective number of bright molecules in the excitation volume. In fact, the effective dark state fraction D_{eff} can be evaluated from $g(0)$ and the input value of $\langle N\rangle$, as $D_{eff} = 1 - [\gamma/(\langle N\rangle g(0))]$.
By increasing the value of k_{23}, the effective dark fraction raises as can be seen in Figure 4.14(A) and (B). Its trend can be closely reproduced (Figure 4.14(B)) by Equation 4.23 for the set of couples (k_{12}, k_{31}) reported as an example in the inset of Figure 4.14A (under the assumption $L = \omega_0/2$ and $k_{12} = 2.35$ MHz and $k_{31} = 1$kHz). It is worth noting that the values of the dark fraction that can be computed from Equations 4.13 (that assumes a complete decoupling of the PD and the brownian diffusion) would be markedly overestimated (inset of Figure 4.14B) with respect to the numerical simulations and the analytical models (Equation 4.23).
Therefore, the good qualitative agreement reported in Figure 4.14 indicates that Equation 4.23 correctly describes the overall effect of the diffusion/photodynamics coupling on the determination of the dark fraction from the ACFs. However, we could not measure the effective dark fraction and therefore the effective diffusion/photodynamics coupling, on real experiments, unless we knew *a priori* the average number of molecules $\langle N\rangle$.

This can be accomplished instead by measuring the σ_2 parameter from the analysis of the $G^{-1}(g(t))$ functions according to Equation 4.24 [3].
The trend of $G^{-1}(g(t))$ of the simulated ACFs (Figure 4.14C) appears to be well described by this equation with an initial photodynamic component that is followed by a linear trend. Depending on the value of k_{23}, the long lag time behavior appears to be slightly upward or downward curved, as expected by the theoretical considerations made by [3].
It must be noted that the suggested analysis of the fluorescence fluctuations in terms of $G^{-1}(g(t))$ stands on the assumption of a robust evaluation of the ACF extrapolation to large and small lag times. At very large lag times, $g(t)$ should attain 1. However, even slight, slow changes in the concentrations due to photobleaching can result in values $g(t \to \infty) > 1$. This trend must be recognized in the ACF and, if possible, corrected or the ACF discarded from further analysis. In fact, in the presence of slow fluctuations of the fluorescence, we expect to have $B = \lim_{t\to\infty} g(t) > 1$ and that $g(0) = B + g_0$.
We can therefore write

$$G^{-1}(g(t)) = \frac{t}{\tau_\Delta}\left(1 + \frac{B}{g_0}\left(1 + \frac{t}{\tau_\Delta}\right)\right)^{-1} \tag{4.25}$$

This G^{-1} function has therefore a downward curvature at large lag times since it extrapolates to $B/g(0)$ for $t \gg \tau_{diff}$.
The presence of the offset, B, on the ACF induces then a negative σ_2 parameter, $\sigma_2 \cong -2B/g(0)$.
An additional source of uncertainty in the G (g) analysis is due to the need to normalize g(t) and therefore to accurately evaluate g(0), which is an issue for fast photodynamics molecules.

Due to those considerations, it is important to assess to what extent the proposed analysis is feasible on experimental data on fluorescent proteins with slow photodynamics. For this reason it is then perfectly applicable to the GFP E222Q mutant under study.

4.2.2.4 Application to photoswitchable proteins: E222Q-GFPMut2

For the cases of photo-switchable GFP mutant, such as the E222Q under study here, the energy scheme representing the chromophore dynamics, such as the ones represented in Figure 4.10, contains both one or several triplet state T and a dark state D. This last trap state, as already underlined in the previous Sections represents the neutral conformational state of the chormophore and can be depopulated by direct transition to the ground state (k_{31}) or by pumping the chromophore from the trap state back to the singlet excited state (at the rate k_{32}), through a transition to some higher energy state

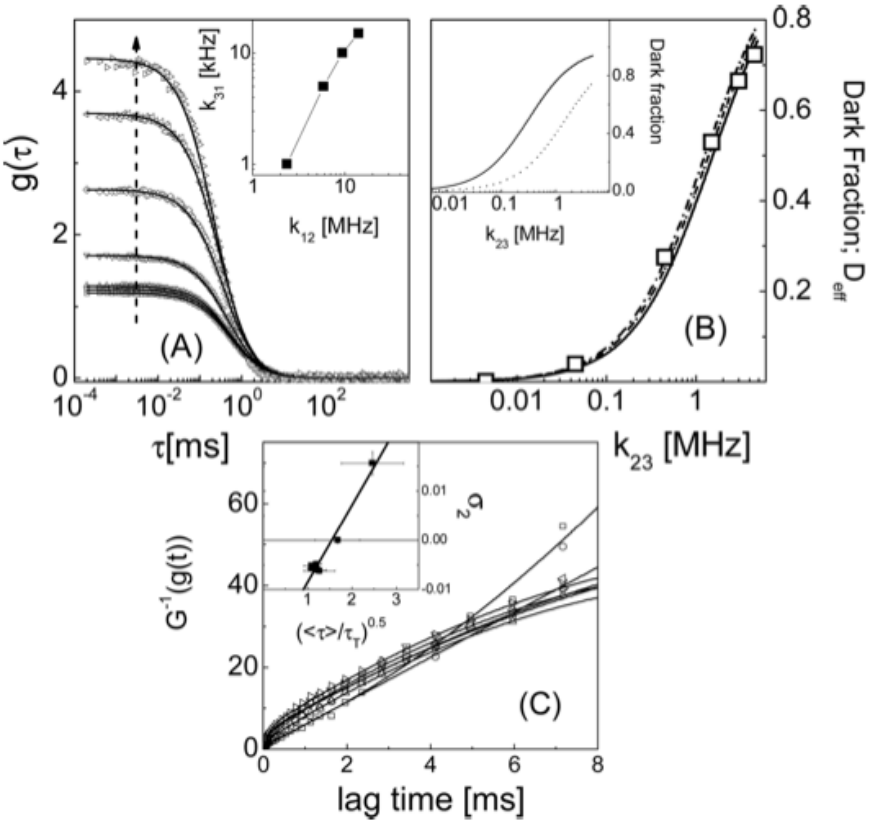

FIGURE 4.14: Simulation of the fluorescence ACFs and extrapolation of the effective dark state fraction, $\bar{T}_{eff}$. The simulation parameters are those reported in Table 4.1 (for the $S0$-$S1$-T part of the energy diagram in Figure 4.10). The dark state rates are k_{31} (assumed here 1kHz) and k_{23} that is varied in the range 450 Hz $< k_{23} <$ 4.5 MHz. Panel A reports the simulated ACF decays corresponding to decreasing values of k_{23}, from bottom to top (k_{23} = 0.45; 4.5; 45; 450; 1500; 3000; and 4500 kHz). Solid lines are the best fit of Equation 4.12 on the simulated data.
Panel B reports the effective dark state fraction $\bar{T}_{eff} = 1 - [\gamma/(\langle N \rangle g_{diff}(0))]$ derived from the best fit value of the zero lag time value of the ACF, $g_{diff}(0)$ (open squares). On the same panel we report the predictions of the triplet fraction obtained from Equation 4.23 (by assuming $L = \omega_0/2$ and one of the couples (k_{12}, k_{31}) drawn in the inset of Panel A). The line code at increasing values of k_{12} is: solid (k_12 =2.35 MHz, k_{31} =1 kHz), dotted (k_12 =5.87 MHz, k_{31} =5 kHz), dashed (k_12 = 9.4 MHz; k_{31} =10 kHz), and dash-dotted (k_12 = 14.1 MHz; k_{31} = kHz). The inset of panel B reports the trend of the dark fraction $\langle D \rangle$ (solid line; Equation 4.23)
Panel C reports the $G^{-1}(g)$ functions of the ACFs reported in Panel A (with the same symbol code) together with the best fit toEquation 4.23 (solid lines). The value of the best fit curvature parameter σ_2 is reported as a function of the coupling parameter obtained by the very same fitting of Equation 4.24 to the $G^{-1}(g)$ functions.

induced by the probe beam.

This kind of processes have been widely studied experimentally by means of FCS [71] and [72] and the data analysis have been carried out in the approximation of complete BD-PD de-coupling (see for example Jung et al. [72] [2]. However, from the results of the previous section, Figure 4.14B, a large underestimation of the value of the singlet

$\rightarrow$ trap state transition rate has to be expected.
It becomes therefore a natural application of the developed simulative method, reported here, to simulate the effect of the photo-switching dynamics on the fluorescence fluctuations.

Continuous probe irradiation In this type of experiment two laser beams, tuned on the $S_0 \rightarrow S_1$ (pump) and the $D \rightarrow D^*$ (probe) transitions respectively (Figure 4.10), are impinging, continuously, on the chromophore.
At first approximation, the effect of the probe beam irradiation is to lower the dark state trapping propensity of the chromophore by effectively reducing $k_{23}^{(eff)} = k_{23} - \sigma_{32} I_{probe}$. We can then expect that, under growing values of the probe beam intensity, the dark fraction (D state) decreases: this can also be derived from Equation (4.23) by using $k_{23}^{(eff)}$ instead of k_{23}.
The fluorescence signal is enhanced due to the dark state depopulation and this trend can be described experimentally by the saturation function:

$$\langle F \rangle (I_{pump}, I_{probe}) = F_0 (I_{pump}) + \Delta F (I_{pump}) \frac{I_{probe}}{I_{probe} + I_{sat}} \tag{4.26}$$

The maximum fluorescence enhancement ΔF and the saturation intensity I_{sat} can be derived from Eq.(4.23) as a function of the k_{23} rate. In the experiments on the fluorescence emission of the E222Q mutant [2] $\langle F \rangle$ was found to decrease at very high probe excitation intensities[13].

The fluorescence enhancement can be derived by considering that, under pump beam only, the fluorescence output is smaller than the maximum output F_{max}, due to the dark state population, D, and it is described by the relation $\langle F \rangle \cong F_{max}(1-D)$. This situation would correspond to $I_{probe} = 0$. On the contrary, when irradiating the chromophore with high intensities of the probe beam (assuming that bleaching or transitions to higher energy states is not significant), the fluorescence signal is $\langle F \rangle \cong F_{max}$.
The relative enhancement factor is then:

$$\frac{\Delta F}{F_0} = \frac{F - F(1-D)}{(1-D)F} = \frac{D}{1-D} \tag{4.27}$$

For example, for the E222Q mutant, a maximum enhancement factor $\Delta F/F_0 \cong 2$ has been reported [2]. We can then set a constraint on the possible values of the (k_{23}, k_{31}) couple that correspond to the enhancement $\Delta F/F_0 \cong 2$. The couples $(k_{23}, k_{31})_{\Delta F/F_0 \cong 2}$ are obtained by putting $\frac{D}{1-D} = 2$ in equation (4.23). In agreement with the experimental

[13] An effect more pronounced when considering the dependence of $\langle F \rangle$ on I_{pump}, see Fig.1.A by Quercioli et al. [2] due to transitions to higher energy states, a process that is not taken into account here for sake of simplicity.

conditions [2] we have assumed $\omega_{xy}^2 = 0.44\mu m$, $\Delta = 90\frac{\mu m^2}{s}$ and $k_{12} = 5.8 \times 10^5 Hz$ or $k_{12} = 1.7 \times 10^7 Hz$ for an incident pump beam power of $\langle P \rangle = 10mW$ or $\langle P \rangle = 80mW$, respectively (Figure 4.15).

It must be noted that the allowed ranges of k_{23} and k_{31} span widely different frequency

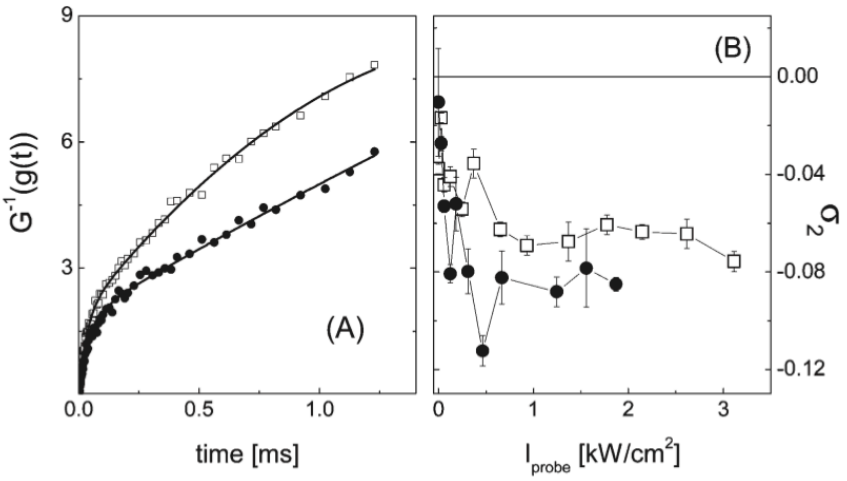

FIGURE 4.15: G^{-1} analysis of the E222Q experimental ACFs. Panel **A**. Samples of $G^{-1}(g(t))$ as a function of the lag time for $I_{pump} = 17\text{kW/cm}^2$ and $I_{probe} = 3.7\text{kW/cm}^2$ (open squares) and $I_{probe} = 0.3\text{kW/cm}^2$ (filled circles). The solid lines are the best fit curves of Equation 4.24 to the data, with best fit parameters: $A = 1.8 \pm 0.04$, $\tau_D = 48 \pm 2\mu s$, $\langle \tau \rangle = 300 \pm 7\mu s$;$A = 1.8 \pm 0.05$, $\tau_D = 33 \pm 2\mu s$, $\langle \tau \rangle = 280 \pm 10\mu s$. Panel **B**. Summary of the analysis of the $G^{-1}(g(t))$ functions: curvature parameter, σ_2, as a function of I_{probe}, for two values of $I_{pump} = 10\text{kW/cm}^2$ (filled circles) and $I_{pump} = 17\text{kW/cm}^2$ (open squares). The points are connected by segments to guide the eye.

ranges, Hz for k_{31} and MHz for k_{23}. The latter is in striking contrast with the result of the approximated analysis of the activation process provided originally by Quercioli et al. [2] in which the diffusive-photodynamics coupling was not taken into account. In that work in fact, the rate k_{23}, that refers to the transition rate between S_1 and the trap state, D, and that was needed to reproduce the observed enhancement relaxation times, $\cong 1 - 10ms$, was surprisingly low, $k_{23} \cong$ 400-500 Hz.

In conclusion, by taking into account the coupling between the slow switching photodynamics and the protein diffusive motion, the values of the transition rate k_{23} are much higher and can acquire more physical values, compatible with constraints reported in Figure 4.15. To this purpose we simulate the photodynamics under dual beam modulated excitation (modulating the probe beam intensity by a square wave function while continuously irradiating the protein with the probe beam).

Modulated probe beam excitation The analytical evaluation of the characteristic times of the photo-switching processes should be obtained from the analysis of the time dependent solution of Equations 4.22. However these times can also be derived from numerical simulations if we exploit the same approach adopted experimentally by Quercioli et al. [2].

This method, fully described in Section 3.3.2.1, Equations 3.3-3.11 is based on the computation of the zero lag time extrapolation ($g(0)$, see Equation 4.12) of the autocorrelation function under modulated probe beam irradiation.
The mathematics, already formalized in Section 3.3.2.1 can be summarized in the following equations:

$$
\begin{aligned}
g(0,\omega) &= \frac{F_0^2}{2(F_0+F_B)^2}\sum_{n=0,1,2} A_{2n+1}^2\left[M_n(\omega,\tau_1,\tau_2)^2 + N_n((\omega,\tau_1,\tau_2))^2\right] \\
M_n(\omega,\tau_1,\tau_2) &= \left(f_1 L_n^R(\omega,\tau_1) + (1-f_1)L_n^R(\omega,\tau_2)\right) \\
N_n(\omega,\tau_1,\tau_2) &= \left(f_1 L_n^I(\omega,\tau_1) + (1-f_1)L_n^I(\omega,\tau_2)\right) \\
L_n^R(\omega,\tau_1) &= \frac{1}{1+(2n+1)^2\omega^2\tau_1^2} \\
L_n^I(\omega,\tau_1) &= \frac{(2n+1)\omega\tau_1}{1+(2n+1)^2\omega^2\tau_1^2}
\end{aligned}
\tag{4.28}
$$

Through the analysis of the trend of $g(0,\omega)$ as a function of ω, obtained from the numerical simulations, we can then measure the characteristic relaxations times of the photo-switching process that falls in the range of the modulation frequencies.
In order to implement the modulated excitation in the numerical simulations, for every time step t the following factor is evaluated:

$$
\pounds = t\nu_L \tag{4.29}
$$

where ν_L is the modulation frequency of the light modulation, $\omega = 2\pi\nu_L$. If $\pounds - \text{round}(\pounds) < 1/2$ then the probe intensity is set to 0. On the contrary, for $\pounds - \text{round}(\pounds) > 1/2$, the probe intensity is set to I_{probe}.

The simulations indicate indeed that the modulation of the probe beam at frequencies in the range 0.1 Hz$\leq \nu_L \leq$1 kHz induce oscillations in the ACFs at times $\tau_n = n/\nu_L$, whose amplitude $g(0,2\pi\nu_L)$ decreases as ν_L rises (see Figure 4.16(B)).
Control simulations have been run to verify that the visibility of the long lag time modulations in the ACFs increases with the protein concentration (Figure 4.16(B), inset).

The simulated $g(0,2\pi\nu_L)$ data are reported in Figure 4.16C for the case $k_{12} = 576$kHz ($I_{pump} = 1.7$kW/cm^2), $k_{23} = 450$kHz, and $k_{31} = 8$Hz (for the simulation of the triplet

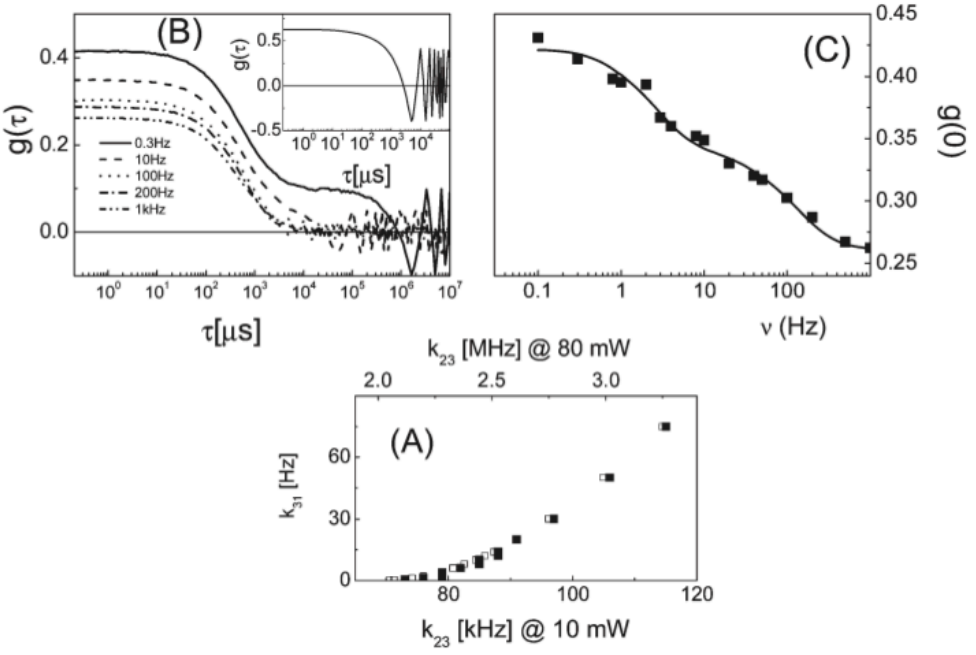

FIGURE 4.16: Panel **A**: couples of values of the relaxation rates k_{23} and k_{31} that satisfy the condition $\bar{T}_eff/(1-\bar{T}_eff) = 2$, according to Equation 4.23, and $\omega_0 = 0.66\mu$m,$D_T = 90\mu$m^2/s. The lower and upper scales (open and filled squares, respectively) correspond to $k_{12} = 580$kHz ($\langle P\rangle = 10$mW) and $k_{12} = 17$ MHz ($\langle P\rangle = 80$mW).
Panel **B**: ACFs computed on simulations run for increasing values of the probe laser modulation frequency with $I_{probe} = 1$kW/cm^2 and $I_{pump} = 1.7$kW/cm^2 and rates $k_{23} = 450$kHz, $k_{31} = 8$Hz, $k_{24} = 20$kHz, and $k_{41} = 13$kHz.
Panel **C**: extrapolated $g(0,\omega)$ values obtained from panel (B) as a function of the modulation frequency (filled squares). The nonvanishing value of $g(0,\omega)$ for $\omega \to \infty$ is to be ascribed to a high-frequency correlation component, F_B. The solid line is the fit of the simulated data to Equation 4.28 with best fit relaxation times $\tau_1 = 45$ms and $\tau_2 = 1$ms.

state dynamics, we have assumed the rates reported in Table 4.1).

These data closely resemble the experimental ones reported by Quercioli et al. [2] and, when analyzed by means of Equation 4.28, provide two relaxation times $\tau_1 = 1$ ms and $\tau_2 = 48$ms, very close to the experimental best fit relaxation times $\tau_1 = 1.3 \pm 0.2$ms and $\tau_2 = 33 \pm 5$ms found by Quercioli et al..

We have not made here a direct fit of the simulated ACFs to the experimental data, mainly due to the different normalization of the data trend relative to the smaller chromophore concentration used in the simulation in order to save CPU times. However, we notice that the qualitative (Figure 4.16B) and quantitative (Figure 4.16C) agreement clearly confirms the validity of the simulation model (within the scheme represented in Figure 4.10A) and the values of the relaxation rates, $k_{23} = 450$kHz and $k_{31} = 10$Hz, for the E222Q mutant.

The substantially higher value of k_{23} with respect to the previously experimentally determined one [2] $k_{isc} = k_{23} \cong 400$Hz, is then to be ascribed to the coupling between the brownian diffusion and the PD processes, thereby showing again the relevance of this phenomenon for the FCS data analysis in these specific cases.

Finally, we again point out that a demodulation spectrum as that reported in Figure 4.16C could have been obtained also within the framework of the energy scheme reported in Figure 4.10B (diabatic transition), though with lower rates (k_{23} = 40 - 50kHz). However, in this case, as discussed previously, the BD-PD coupling should decrease with increasing probe intensities, opposite to the experimental behavior reported in Figure 4.15.

4.2.3 Simulative and Mathematical Conclusions

We have analyzed the effect of the coupling between the molecular Brownian diffusion (BD) and the chromophore photodynamics (PD) on the shape of the fluorescence autocorrelation functions. For the case of uniform spherically symmetric excitation volume, the chromophore dark fraction scales, with respect to the uncoupled result, as the square root of the ratio of the diffusion to the photodynamics relaxation times, $lL = (\tau_{diff}^{(xy)}/\tau_{dark})^{1/2}$. We have also discussed a graphical method, called here G^{-1}-analysis, for the evaluation of the BD-PD coupling on the fluorescence ACFs. This kind of analysis is based on the evaluation of the sign of the large lag times curvature (σ_2) of the inverse of the ACF and has provided us with an estimate of the limit of the coupling parameter, $lL \cong 2$, below which the effect of the BD-PD coupling on the ACF decay becomes effective.

The G^{-1}-analysis has been validated on numerical simulations and applied to data on the E222Q mutant. From the numerical simulation, we find that the curvature parameter, σ_2, scales with the ratio $(\tau_{diff}^{(xy)}/\tau_{dark})^{1/2}$. This result indicates that, despite the crudeness of the approximations made here, our simple analytical treatment describes qualitatively rather well the dark fraction values and the ACF shape and suggests a data analysis method to be applied to the experimental ACFs to evaluate the amount of diffusion/PD coupling.

Finally, numerical simulations applied to the study of the GFP slow photoswitching dynamics are essential to correctly estimate the relaxation rates of the process. For the case of the E222Q mutant, the estimate of the excited singlet to the dark state relaxation, k_{23}, is approximately 3 orders of magnitude lower when we do not take into account the diffusion-photodynamics coupling. The treatment given here indicates a numerical simulation approach that could be applied to the analysis of the fluorescence fluctuations arising from the photodynamics of photo-switchable fluorescent proteins.

Chapter 5

Introducing Beating Mode

In this Chapter we present the theoretical principles behind the new image acquisition protocol we have developed in these years.
As will be shown, this protocol, that we called **Beating Mode**, is characterized by an innovative exploitations of the peculiar properties of photo-switchable chromophores (throughly discussed in the previous Chapters), in order to obtain images with an higher information content.

5.1 Basic Principle of B.M.

5.1.1 Standard Imaging Limitations

In a standard imaging process, as described in Chapter 2.1.3, there is a relative motion between the sample and the laser beam[1] while detecting the output fluorescence intensity.
The acquisition software then rebuilds the image matrix inserting in every pixel of the image matrix the fluorescence photon rate, emitted by the very portion of the sample mapped by the particular pixel itself.

The evident limitation of this kind of imaging is that the only information contained in the image is the fluorescence photon rate directly proportional to the concentration of the chromophores in the sample. On the contrary, our new protocol gives also informations about some physical properties of the sample such as pH and viscosity.

[1] Or the other way around

5.1.2 Exploiting Photo-Active Chromophore for Better Imaging

The acquisition protocol hereby proposed allows to overcome the previously mentioned limitation by exploiting the properties of the photo switchable chromophores such as the GFP Mutants described in the previous Chapters.

In particular, with a single Beating Mode acquisition, as it will be detailed, it is possible to obtain raw data that can then be analyzed to obtain up to four different images out of the same acquisition. Each image maps a peculiar characteristic of the photo switchable chromophores in the sample:

- The standard **marker concentration** images, where the information is the photon count rate per pixel as mentioned proportional to the local concentration of the chromophore in the sample. This image is at the same time obtained both for the activated case (D state depopulated) and the de-activated case (D populated).
- The **ER** map image. In this image, the information stored in each pixel is the enhancement ratio between the deactivated and the activated chromophore condition.
- The **DePopulation Time** map image. In this image the information stored per pixel is the best fit D-state dePopulation time induced by the irradiation of the sample by the probe light.
- The **Population Time** map image. Same as the latter but with the D-Population time consequent to the switching on of the probe beam.

As discussed in the previous Chapter, for the GFP mutants the photoactive properties we are able to map pixel-by-pixel are dependent on properties of the surrounding of the fluorescent molecules such as the pH or the viscosity.
The Beating Mode protocol, hence, allows the mapping on a biological sample of the physical and chemical properties of the sample itself, and the information content of the single image acquisition is therefore increased.
Of course, as it will be discussed in a few pages, the basic laws of the information theory suggests that this increase of output information is paid in terms of image acquisition time.

5.2 Beating Mode Acquisition Protocol

Let's now see how to engineer our image protocol acquisition in order to obtain al the spectroscopic parameters regarding the D-state dynamics.

The method bases on subsequent scans of the same acquisition line, in order to re-costructruct for each pixel, at least, one full period of On/Off switch of the probe light. This allows to obtain, for each pixel, the full trend of the light emission of the sample under the following photo-physical condition:

1. Only pump excitation: the average pixel content under this condition il the photon rate arising from the chromophore when the D state is populated.
2. Transition between only pump and pump + probe excitation (D-state depopulation time)
3. Pump + probe excitation (ER is the ratio between the ratio between the photon rate under this condition (D-state depopulated) and the one in point 1)
4. Transition between pump + probe (bright state) and only pump excitation representing the average D-state population time.

5.2.1 Exploiting Subsequent Scans of the Same Sample Line

Keeping in mind the acquisition experimental setup, described in Appendix C, let's define the following variable:

- ν_L is the scanning frequency of a single line of the sample; $T_L = 1/\nu_L$ is the acquisition time of a single line
- ν_S is the open/close shutter frequency that regulates the irradiation **only** of the probe beam on the sample. The effective frequency of the square wave probe signal impinging on the sample is $\nu_S/2$.

In order to elucidate the method, let's first consider the single line acquisition of a uniform dye concentration sample.
If $\nu_S > \nu_L$ the PMT detects a square-waved signal such as the one in Figure 5.2.1 (A). When the probe beam, as well as the pump, impinges on the sample, we detect the fluorescence enhancement due to the depopulation of the dark state D (see Chapter 3.3.2 and 4.1.2) and this correspond to the high level of the trace in Figure 5.2.1 (A).
Let's now suppose that the ratio between the two frequencies, ν_L and ν_S is a natural

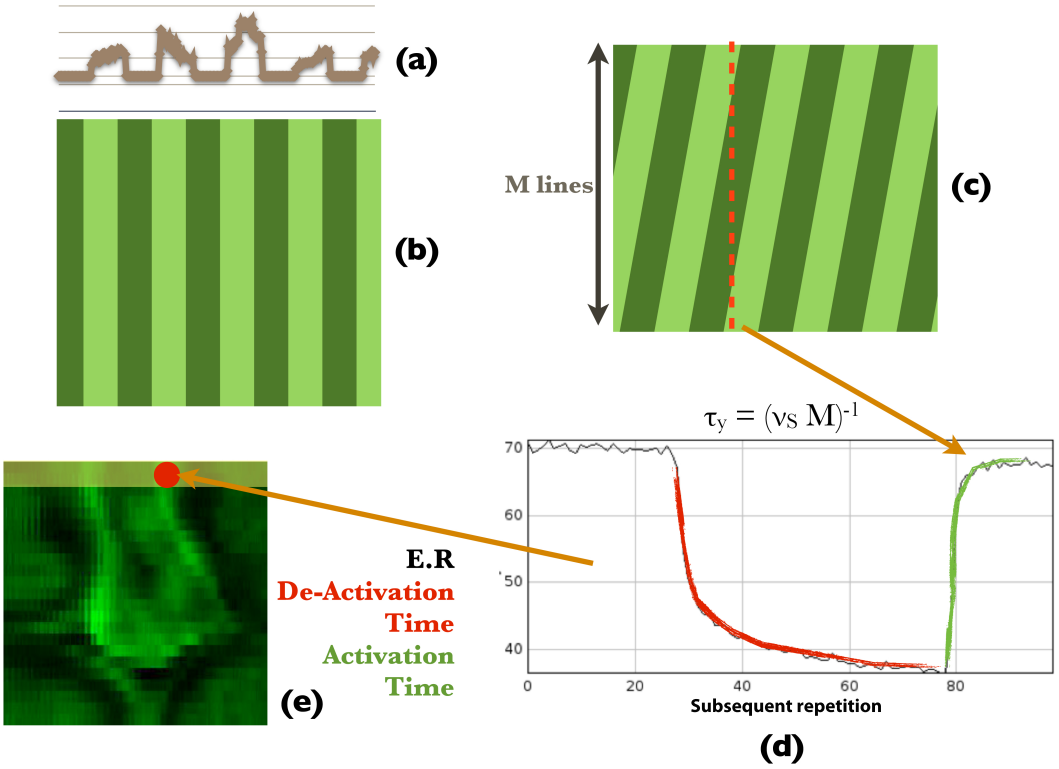

FIGURE 5.1: Beating Mode acquisition principle. In Panel (**A**), a single line acquisition with constant pump and square-wave modulated probe irradiation on a homogeneous sample. In Panel (**B**), a multiple acquisition of the same sample line with the probe shutter frequency, ν_S, being and integer multiple of the line acquisition frequency, ν_L: the image reports the dark and bright fringes perfectly vertical along the subsequent line repetition. In Panel (**C**), we show the same repetitive acquisition of the same line with a value of the ν_S slightly different from a different a integer multiple of ν_L: the effect is to have a inclination of the fringes in the images and the possibility to explode the dark-bright transition along the y direction of the single-line repetition image. In Panel (**D**), the intensity plot along a y-line represents the explosion of the whole dark-bright transition along the M repetition of the same sample line. The x axis in the plot can be converted in a time scale representing the delay of the probe on/off switch for every subsequent repetition on the same sample line via the formula $\tau_{repet} = (\nu_S M)^{-1}$. From this plot it is possible to calculate for every pixel of the sample line the three output information of B.M.: the enhancement ratio, the D state depopulation time (probe beam on) and the D state population time (probe beam off). The informations are then stored in each pixel corresponding to the acquired sample line and the same operations are repeated for each line of the sample in order to obtain a complete image Panel (**E**).

number[2]. If so, in the case of multiple acquisition of the same line, we obtain the same dark-bright fringes all over again for each line repetition. Representing in a image matrix (on the x the pixel of the sample line and on the y the repetition on the line itself) the series of acquisitions of the same line, we would obtain something similar to what is represented in Figure 5.2.1 (B).

[2]After correction of the ν_L value for the delay imposed by the return of the beam at the beginning of the line.

What we are actually interested here is to be able to study the dark-bright transition, due to the probe light on/off switching, for each pixel of the line. This can be done simply by slightly varying the ν_S/ν_L ratio. In this way we have, for every subsequent repetition, a tunable positive or negative delay of the probe light switching on each pixel: the effect of this delay is an inclination of the dark-bright fringes[3] (see also Figure 5.2(B). If we choose wisely, both the ν_S/ν_L ratio and the number of repetition on the same line, we are able to identify, along the y image direction, the dark-bright and bright-dark transition for each pixel of the sample line. The image matrix representation of the repetitive acquisition of the same sample line will then get similar to the one represented in Figure 5.2.1 (C).

We can now plot the fluorescence signal trend for each x-pixel along the repetition axis (the y axis) for the same sample line: if the frequency ratio, ν_S/ν_L, is chosen wisely for every single pixel it is possible to have the blow up of a full dark-bight transition, such as the one represented in Figure 5.2.1 (D). The x axis in this plot represents, of course, the number of the repetition on the same line, but this can also be converted in a time information. In fact, if we count how many pixel a full dark-bright transition (triggered by the ν_S frequency) is exploded in, it is possible to obtain the value of the lag time represented by each repetition for every sample pixel.

If a single full dark-bright transition is exploded in M lines, the lag time of the single repetition pixel representing the phase shift between subsequent lines (on the y axis in the image matrix of Figure 5.2.1 (C), and on the x axis in the plot of Figure (D)) simply is:

$$\tau_{shift} = (\nu_S M)^{-1} \tag{5.1}$$

Actually this is a very important information, since it allows the fitting of the exponential decay/growth of the fluorescence intensity signal and the measure of the average lifetime of the population and depopulation processes triggered by the probe light on/off switching.

The resolution of this decays relates to the number of repetition M required to obtain the full activation of the whole sample line (this value being dependent of the ν_S/ν_L ratio) and therefore on the acquisition time for the sample line $\nu_L M$. The more precise we desire the information about the photo dynamics to be, the longer we have to spend acquiring the sample image.

In conclusion, from a plot, such as the one represented in Figure 5.2.1 (D), it is possible to obtain all the informations of interest for each pixel of the acquired line (Figure 5.2.1

[3]The sense of this inclination changes in relation to the ν_S/ν_L ratio: in the imposed delay is positive the fringes will be falling backward, whereas in the case of a negative delay the fringes will be falling forward. The higher is the gap between the ν_S/ν_L ratio to an integer value, the more sloped the fringes will be.

(E)):

- the **E.R.** values are obtained dividing the averaged value of bright plateau with the averaged value of the dark plateau.
- the **photo activation/deactivation times** are obtained by the fitting of the exponential growth/decay characteristic of each transition, with the time-resolution limitation introduced above and argumented in the following Sections.

In order to complete the acquisition, this procedure has to be repeated on all the lines of the sample: this way it is possible to obtain the maps of the E.R. and the photodynamics times along the sample area. Using than the characterizations presented in Chapter 4.1, it is possible to obtain the functional maps of the desired chemical/physical characteristic of the sample itself.

5.3 Taking Bleaching into Account

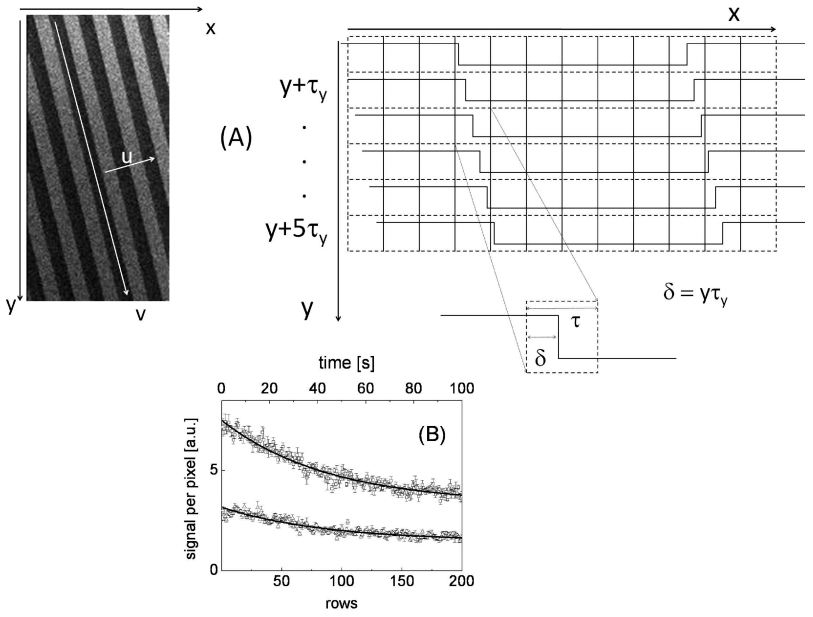

FIGURE 5.2: Beating Mode experiments in Acrylamide gels. As mentioned in the text, the sample were scanned under conditions in which a slight difference exists between the line scanning and the modulation wave frequencies that yields a time shift $\delta = \tau_{shift}$ per subsequent row-repetition. The **image** reported is therefore only the collection of several line scannings of the same row on the gel. (A) The image, acquired in the beating mode, was $10 \times 20\mu m^2$ (100×200 pixels) in size, and it was acquired at a $\nu_L = 1.9608$Hz line scanning frequency while the shutter frequency was set at $\nu_S = 9.78$Hz. The corresponding time shift per row is $\tau_{repetition} = 1.23$ms. The x-, y-, and v-axes are indicated as arrowed lines. The sketch outlines the time scanning along the three axes. The blowup illustrates the role of the time shift per row, $\tau_{repetition}$, and of the time shift, δ on each pixel. (B) Plot of the average of five profiles measured along bright (open squares) and dark (open triangles) V lines on the image reported in (A). The time scale is set by the line scanning frequency. The solid lines are the best-fit exponential fit to the data.

As in all the optical imaging methods, particularly if based on laser scanning, the most relevant competing phenomenon that has to be taken into account in a BM acquisition[4], particularly when dealing with organic chomophores is the **bleaching**.

The photo bleaching is the statistical turning off of fluorescent molecules as a consequence of repetitive excitation in time [88] [89].

When performing measurements on single molecule the effect of a bleaching is a on/off switch of the fluorescence intensity detected.

When operating in bulk, the single molecule on/off phenomena sum in an exponential decay of the fluorescence signal vs. the excitation time [90] and [91].

[4]several subsequent acquisition i.e. Excitation on the same sample line

An example of the bleaching effect on GFP Mut2 proteins in relation to the beating mode acquisition protocol is reported in Figure 5.2. Here, one can appreciate that the repeated acquisition of the same line on a uniform sample of E222Q mutant embedded in an Acrylamide gel.
From the picture it is easy to realize how the sample gets less and less fluorescent increasing the number of subsequent excitations. By plotting the fluorescence signal along the dark and bright fringes (v direction in Figure 5.2A), it is possible to measure the decay of this signal as a function of the line acquisition time and obtain from a fit the parameters of the photobleaching, as an exponential decay trend dependent on the excitation time, as reported in the literature (see for example Lakowicz and Masters [92]), see Figure 5.2 (B).

In order to the BM acquisition to be effective, particularly in the calculation of the Enhancement Ratio, the effect of the bleaching has to be subtracted from the raw data. The way that we have chosen to do that is reported in Figure 5.3.
For each pixel we consider the plot of the emission as a function of the number of time repetitions (i.e. the intensity plot along the y direction in Figure 5.3 (A)). In this plot (see Figure 5.3B) we can discern the dark and bright states that are not plateau regions, as one would expect, but slowly decays that are fit to two exponential decays (the violet and red lines in Figure 5.3B). The best parameters of the exponential fits are used to compute the contribution of the photobleaching that is subtracted from the raw data in order to recover the correct, bleaching unaffected, fluorescence intensity of the sample pixel.
This bleaching correction method, whose results can be seen both analytically (Figure 5.3 panel B and C) and pictorially (Figure 5.3 panel A and D), needs a huge analytical work to be carried out for each pixel of every line of the acquired sample. For this it is mandatory to have a dedicated analysis software that automatically and efficiently recover the relevant parameters from a raw image. This raw image is M times larger than the conventional image, M being the number of repetitions per scanned line. The piece of software, that we developed and that will be discussed in the next Chapter, is optimize for the CPU time.

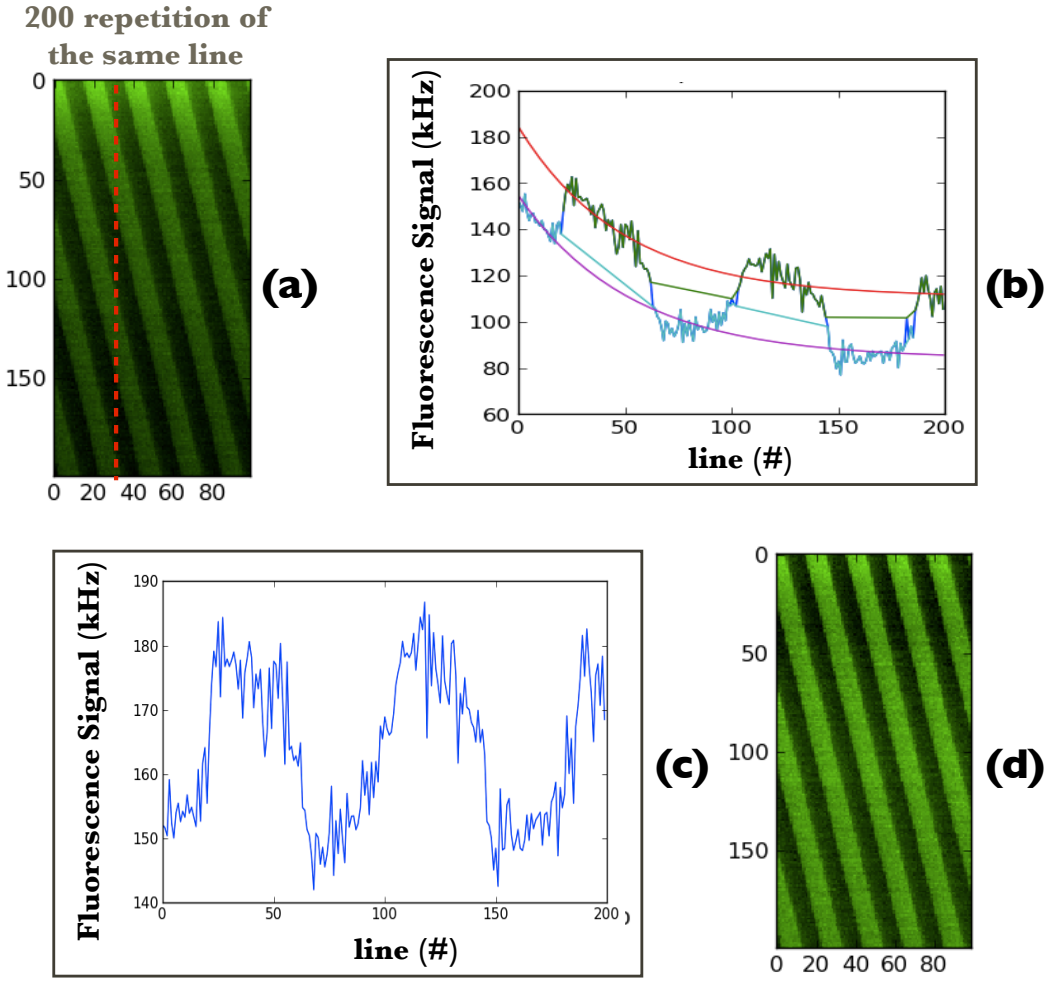

FIGURE 5.3: Bleaching Correction in B.M. Acquisition. In Panel (A) a 200 repetition acquisition on the same homogenous sample line with pump + modulated probe excitation: the effect of the bleaching is clearly visible in the darkening of the image as the repetitions adds. In Panel (B) the same effect can be identified in the intensity plot vs the line repetition where one can easily identify the combined effect of the exponential bleaching and the square modulation of the signal induced by the modulate depopulation of the D state. The dark and bright pixel are fitted with an exponential decay function used in order to normalize the effect obtaining the plot in Panel (C). The effect of the bleaching correction is clearly visible in the now homogeneously luminous image of Panel (D).

5.4 Optimizing a B.M. Acquisition

5.4.1 How to Get the Best from Beating Mode Data

As outlined in the previous Section, the B.M. protocol can be a significant innovation in the image acquisition methods, due to its capability of exploiting the photo physical parameters of photoactive chromophores, to obtain functional maps of the sample.
The possibility to use GFP mutants protein (that can be encoded in the native genome

of cells, and by them expressed) as markers gives the possibility of cellular functional probing without the introduction in the sample of an external probe[5].

For all these reasons it is of paramount importance to understand how to optimize the analysis of the huge amount of data that is the output of the acquisition of a whole image under the BM protocol, in order to extract from them the most complete information content.
We discuss first the parameters that affect the repeated single line acquisition under probe beam modulation. A complete raw image will be then set up by M times the number of lines of the conventional image, M being the number of repeated scans of each line.

5.4.1.1 Noise Correction

Until now we detailed how the information about the Enhancement Ratio and the Photo Dynamics times are obtained for each pixel of the matrix image.
These three out coming images[6] cannot anyway exist by themselves due to the intrinsic unassessability of the noise impact.

In a standard, fluorescence intensity based, image, in fact, a threshold on the noise can be identified and a threshold correction of the image can be implemented by setting a custom value. This value is easy and direct to estimate since the information represented in the image is the same used for the threshold setting [93] [94].
The same thing is far from straightforward when dealing with a BM images. For example, the construction of the E.R. image, automatically calculate the fluorescence intensity ratio between the two excitation condition[7] on each pixel, regardless the intensity of the fluorescence signal arising from the pixel itself[8].
The potential false information that these noise pixels may provide is of course misleading and extremely subtle, and has for this reason to be screened (see Figure 5.4).
For example, a pixel that corresponds to a detected area (the point spread function) in which the chromophore content is so low that the average fluorescence signal is much lower than the (mostly but not only) thermal noise from the photon detectors, can contribute to the ER image in two ways:

- **E.R. < 1**: this is the less subtle case where the signal is detected higher under pump only excitation that under pump + probe excitation. Being the information

[5] That may change the characteristics of the sample only due to its presence
[6] Those where the information stored is respectively the ER, the population and the depopulation time.
[7] pump only and pump + probe
[8] i.e. regardless of the actual presence, in the pixel area, of any concentration of photoactive chromophores.

an absurd regarding the physics we are here observing, this case is easily identifiable even without screening.

- **E.R. > 1**: this is the more sneaky case because the E.R. contribution of the pixel may have values compatible to one expected for the photoactive sample. Without the parallel information of the fluorescence intensity this kind of noise is impossible to screen and actually provides false informations.

The same argument, of course, holds for the population and depopulation times images where such a noise screening is just as important.

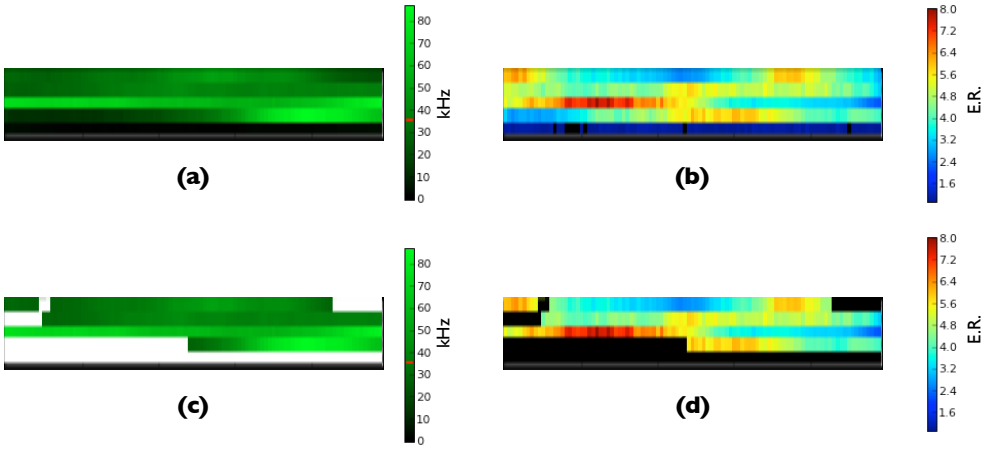

FIGURE 5.4: Noise Correction in BM acquisitions. In Panel (A) is reported the standard fluorescence image of a non uniform sample marked with GFP E222Q under pump+probe illumination condition[9] In Panel (B) the corresponding B.M. image where the information represented is the E.R. Some of the zone in the E.R. images contributes with a sensible signal even if the fluorescence intensity arising from the corresponding pixel is more compatible with noise than with actual fluorescence. To correct this phenomenon it is possible to set e noise threshold on the standard images (Panel (C)) that is then reported in the E.R. image thus filtering the noisy pixels (Panel (D)).

The noise screening is directly implemented in the analysis program developed during this work and detailed in the next Chapter.
The software allows to set the threshold on both the dark and bright fluorescence state images and then to maintain it on the B.M. images. This way only the fluorescence contributing pixels are taken into account in the output functional maps.

5.4.1.2 Choice of the Studied Chromophores

In Section 4.1, for two GFP Mut2 mutants, we presented a characterization of the trend of the photo-physical properties, mapped by the B.M. acquisition protocol, as a function of some physical properties of the molecules surrounding.

As reported the behavior of the different mutants is quite different and can give a hint regarding the choice as a function of the desired application.

- E222Q mutant with its monotone trend is naturally the best choice for a full spectrum mapping of the pH of the sample; the little magnitude of the variation of the values along the spectrum, though, makes the data analysis quite difficult. Furthermore E222Q E.R. show a slight monotone trend as a function of the sample viscosity.
- Mut2GQ is the ideal choice for the mapping of the neutral regions of a sample due to the sharp peak both in the E.R. and the PhotoActivation times.

5.4.2 How Many Repetitions Per Lines

In order to conclude the first outlook on the B.M. acquisition protocol, is worth noting that the setting of the B.M. characteristic frequencies, ν_L and ν_S (see Section 5.2.1), influences both the time usage of, and the informations stored by, the single acquisition.

First of all, the setting of the ν_L frequency[10] influences directly the acquisition time required to collect the whole image data.
Of course, since the implicit aim is to have the quicker acquisition possible, the ν_L should be kept as high as possible, but experimental limitations have to be taken into account:

- The target dyes under study here are a biological protein characterized by by moderate values of quantum yield, (0.4-0.6) and hence a limited number of output photons per pixel. A limit to the frequency is then imposed by a minimum integration time per pixel that allows the detector to record a significant number of photon, so not to have an excessive contribution of the noise in the image.
  For a generic sample emitting an average signal of 100-200kHz, in order to collect 5-10 photons per pixel, the pixel acquisition frequency has to be limited to 20-50kHz; as a consequence $\nu_L < \frac{1}{N} \cdot$ 20-50kHz, where N is the number of pixel per line in the image matrix.
- The image acquisition setup used in this work (and described in Appendix C) also imposes a significant limitation that overcomes the one just outlined.
  In our case, in fact, is the sample to be moved along the exciting beams by means of pietzo-electric μmotors. Due to the characteristics of this motors the frequency for each μstep has to be limited in order to have repeatability between subsequent

[10] ν_L, directly proportional to the single pixel acquisition frequency, with a factor N, number of pixel per line, is the inverse of the permanence time of the detectors on each pixel of the image.

scanning of the same line/image. For the applications proposed in this work the pixel acquisition frequency was always set between 100Hz and 1 kHz.
With an improved galvanometric mirrors imaging system, this limitation can be easily overcome and the only limitation would be the limited brightness of the dye.

Slightly more complex are the considerations that lead to the choice of the ν_S parameter. As already mentioned before, the fine tuning of this frequency determines the inclination of the dark-bright fringes and, hence, the number on repetition of the same line in which a single dark-bright transition is exploded.
In particular the more the angular coefficient of the fringes is close to zero, the more compressed is the dark-bright transition in the y direction of the raw image (i.e. number of line repetition) in Figure 5.2. As the fringe's angular coefficient gets steeper, we have an increment of the line repetitions needed to track a full dark-bright period.
The compromise here is fairly evident: in terms of acquisition time the aim should be to adjust the ν_S in order to minimize the subsequent repetition on the same line. The problem in doing so is that there is a loss in terms of time resolution, necessary to well fit the photodynamics times as pictured in Figure 5.5.
When dealing with images in which we are only interested in the E.R. the number of repetitions per line can be minimized down to 20-30. If we are also interested in the PD times the number of repetition has to be increased up to 90-120. In this case the acquisition time can be a serious limitation.

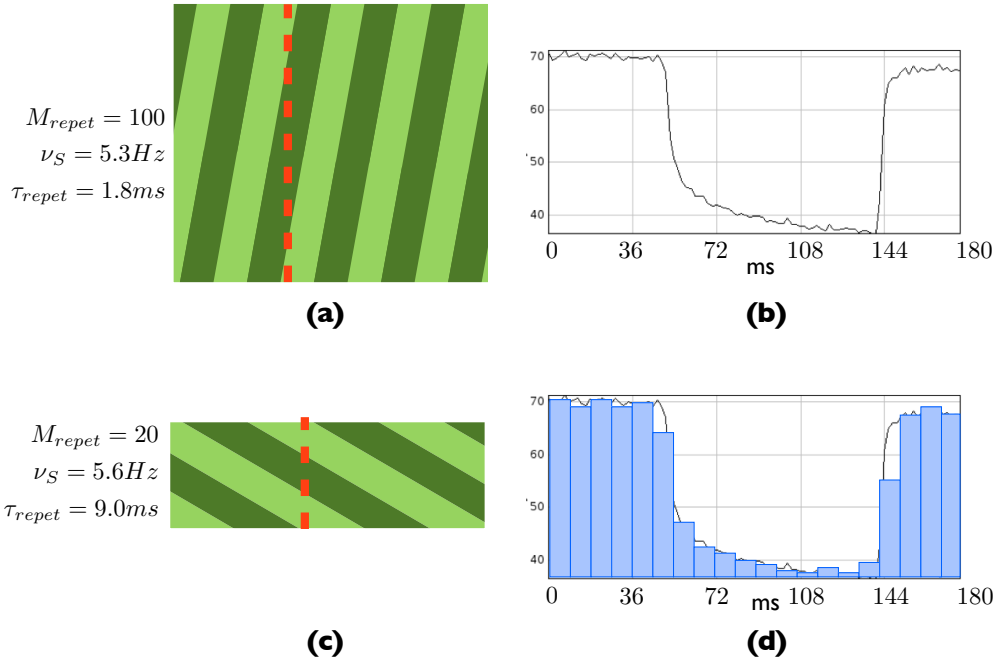

FIGURE 5.5: The choice of the ν_S in relation with the ν_L can tune the inclination of the fringes and thus the time resolution of the dark-bright transition plotting. Fixed ν_L = 1Hz the choice of ν_S = 5.3Hz implicates a slightly inclined fringes and a time resolution of the y direction plot, corresponding to the lag time between subsequent repetition, of 1.8ms (Panel (A) and (B)). This however cause 100 repetition to be acquired in order to be able to plot a full dark bright transition. In Panel (C) and (D) the shutter frequency is set to ν_S = 5.6Hz. The fringes are more inclined, the time binning along the transition plot is less efficient (9.0ms) but the full transition is acquired in just 20 subsequent repetition. If we are only interested in the E.R. this is the optimal acquisition time condition in which to operate.

Chapter 6

Beating Mode Protocol Application

As understandable from the B.M. protocol presentation of the previous Chapter, in order to obtain any image , the raw data image matrix, acquired with B.M. protocol,has to undergo some serious data analysis. At the begin of this Chapter we presents the Raw Data Analysis Software we developed during this work. After that, actual applications of the B.M. acquisition and analysis method will be presented.

6.1 B.M. Analysis Software

The B.M. analysis software has been developed in collaboration with a computer scientist of the Politecnico di Milano. The code has been chose to be written in Python since this coding language combines a easy portability between operating system and the availability of a large amount of high level scientific libraries[1].

6.1.1 Analysis of a Single Line Repetitive Acquisition

In order to explain the various function of the analysis software let's focus, for starter, on the operations it performs during the analysis of a single repetitive acquisition of a particular sample line (Figure 6.1).

[1] iPython, Numpy, Scipy , wxWidgets and PyLab

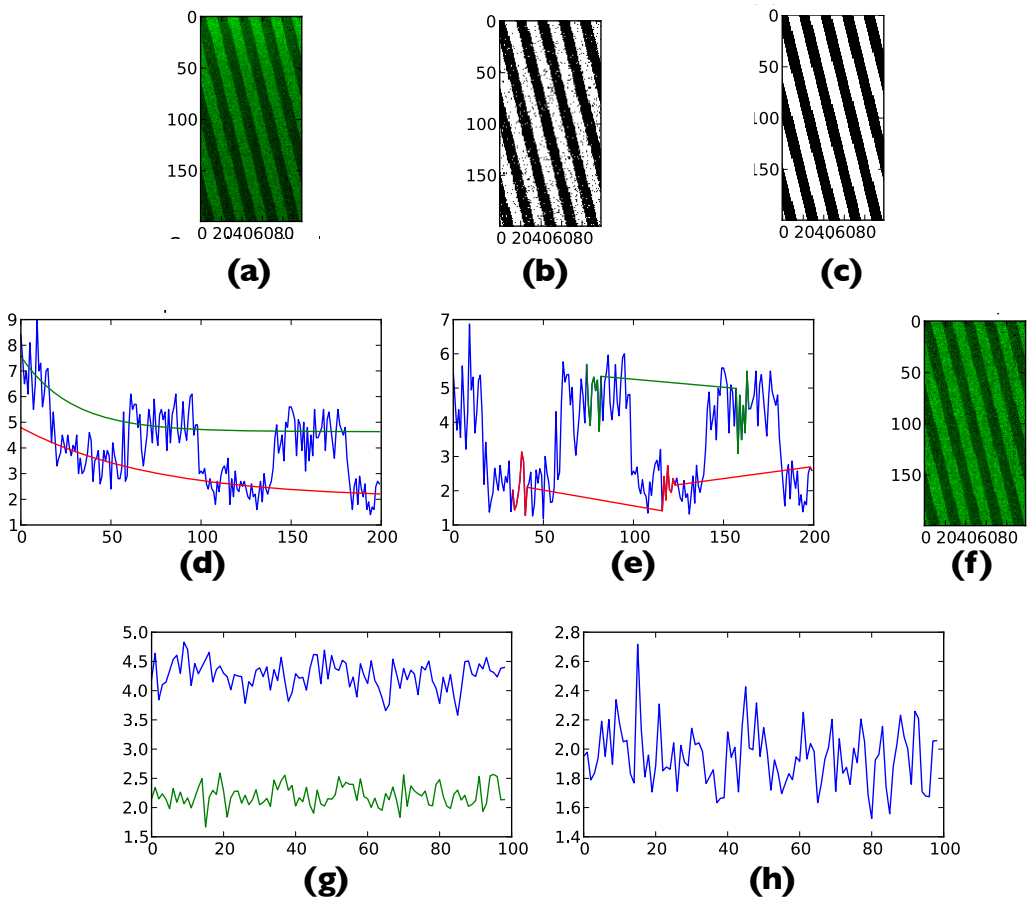

FIGURE 6.1: Single Line B.M. Analysis on a homogenous GFP-marked Acrylamyde gel. In Panel (A), the raw data of a single line acquired in 200 subsequent repetitions. In Panel (B), the first *dark-bight* categorization based on the column average calculation. The square wave fitting refinement results is shown in panel (C), where it is possible to see how the fringes are optimally defined and labeled. In Panel (D),the fluorescence intensity plot (divided between dark and bright contributions) with the fitting bleaching curve. In Panel (E), the same plot with the bleaching effect corrected and the emission renormalized. In Panel (F), the image as in Panel (A) but with the bleaching effect corrected: it is possible to see how the luminosity of the image does not degrade along the following repetitions. In Panel (G), for each pixel of the sample line the average value of the dark and bright status is plotted. The average calculation is done on a user-definable fraction (usually 50% centered on the fringe) of the dark and bright pixels per fringe (highlighted in Panel D): this in order to reduce the noise do to the D state population and depopulation time. In Panel (H), the plot of the enhancement ratio vs. the x pixel on the aquired sample line.

6.1.1.1 Probe Mask Definition

The first macro operation performed by the analysis software when dealing with a repetitive acquisition of the same sample line is to label each pixel as *bright* or *dark*[2]. The labeling depends on the illumination condition under which the sample contributes to the particular pixel acquisition.
The label operation is composed by two subsequent steps:

- The first gross distinction is done analyzing per columns all the pixels, along the subsequent repetitions, corresponding to the same sample area (y direction in the image of Figure 6.1A). The average value of the fluorescence is computed for each column, and the software labels as *bright* the pixel with a recorded fluorescence photon count above the average, *dark* otherwise (Figure 6.1B).
  Of course this first labeling is deeply affected by the bleaching process: this means that the labeling is more precise for the first repetitions and loses reliability with the repetitions as the photon count is lowered by the bleaching.
- The second labeling steps operates on the previous results fitting a square wave function on the repetition pattern. Knowing the B.M. frequencies, ν_L and ν_S, and accounting for the end line delay occurring at each repetition[3] the fitting actually estimate the initial phase of the dark-bright fringes pattern.
  This step integrated with the previous allows a sharp and well defined labeling of the dark-bright fringes both on uniform and patterned samples (Figure 6.1C)

6.1.1.2 Bleaching Correction

Also the bleaching correction has to be done column-by-column since adiacient pixels of the sample line can map different concentration or population of chromophore and therefore be affected by different bleaching.
The algorithm, for each column, fits the function

$$y = A \cdot e^{-t/\tau_{Bleac}} + C \tag{6.1}$$

separately on the dark and bright data (6.1D). A check is done on the two characteristics bleaching time founded in order to check the compatibility of the two values obtained by the fit.

[2]hence discerning if the sample contribution of the generic pixel x at the acquisition time t is due to the fluorescence of the dark (pump only excitation) or bright (pump + probe illumination) state of the chromophore.
[3]Delay do to the repositioning of the pietzo-electic

If the fit was performed correctly the column data are renormalized (as represented in Figure 6.1E) to the maximum fluorescence value recorded at $t = 0$.

The bleaching functional fitting and correction is a fairly complicated matters to be implemented due to the intrinsical non reproducibility of the data on subsequent images. The experience during this work has allowed us to differenciate various typical cases that can be encountered by the analysis software.

- Best case scenario: the two fit are carried out correctly, returning compatible values of the two different bleaching process lifetime τ_{Bleach}. Here the correction and renormalization is straightforward.
- No fittable bleaching: in this scenario, occurring particularly on multiple acquired samples, the bleaching process presents itself only as the far tail of the exponential decay. Trying to fit an exponential (starting from $t = 0$) on an almost flat data trend, returns output values unpredictable and absolutely not physically credible for both the fitted τs. In this case the bleaching correction step is automatically skipped by the software.
- Mixed-up scenario. In this, extremely unfrequent, case. The two bleaching times fitted are two completely different numbers. When this happens the sw have built-in a range of acceptability for the τ_{Bleach}[4]: if the fitted τ stays into this range the bleaching is corrected , if not the bleaching is not renormalized.
  In the case of a column where the bright bleaching is corrected but the dark one is not, the software proceeds raising a flag in a log file. A case like this is keen to happen when the E.R. is extremely high: the dark state excitation base line is characterized by a low bleaching effect whereas when the chromophore is in the bright state the bleaching process becomes serious.
  In Figure 6.1F the same image of panel A but with the bleaching effect renormalized.

6.1.1.3 E.R. Calculation

After the bleaching correction the software calculates the average photon count intensity for both the dark and bright state of the chromophore, using only a used-definable fraction of each fringe (highlighted in 6.1D). This selection is done in order to avoid possible noise due to the D-state population and depopulation times.
The average values are reported in Figure 6.1G plotted vs. the x pixel on the acquired

[4] 1sec$< \tau_{Bleach} <$200sec

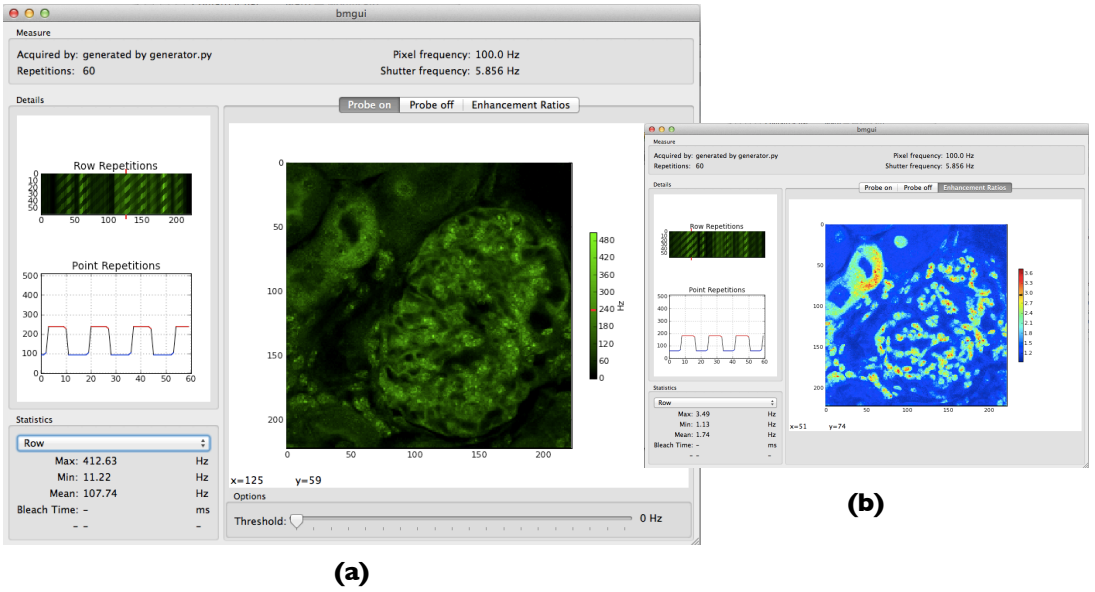

FIGURE 6.2: B.M. Analysis software: GUI and full image analysis. The bright state, dark state and E.R. images are reported in different tabs: in Panel A the bright state corresponding to the E.R. reported in Panel B.

sample line. The ratio between this two values is reported in a similar plot in Figure 6.1H.

6.1.2 Multi-Line Analysis

When dealing with multi-Line images, that is *always*, the software iterates the algorithm steps described in the previous Sections on all the single repetitive-acquired sample lines.

6.1.2.1 Full Image of the Sample

The Graphic User Interface, shown in Figure 6.2, is organized so that the raw data analysis is performed on the opening of the raw data. The picture is then reconstructed with the right pixelage and the information about the B.M. acquisition parameters, necessary for the analysis are read directly from the raw data text file and reported on the top of the window.

On the left, the software show the various repetitive acquisitions regarding the particular sample line selectable by the mouse positioning. Right below for the selected series of repetition the intensity plot the particular pixel along the subsequent repetitions.

The bright state, dark state and E.R. images are reported in different tabs (Figure 6.2).

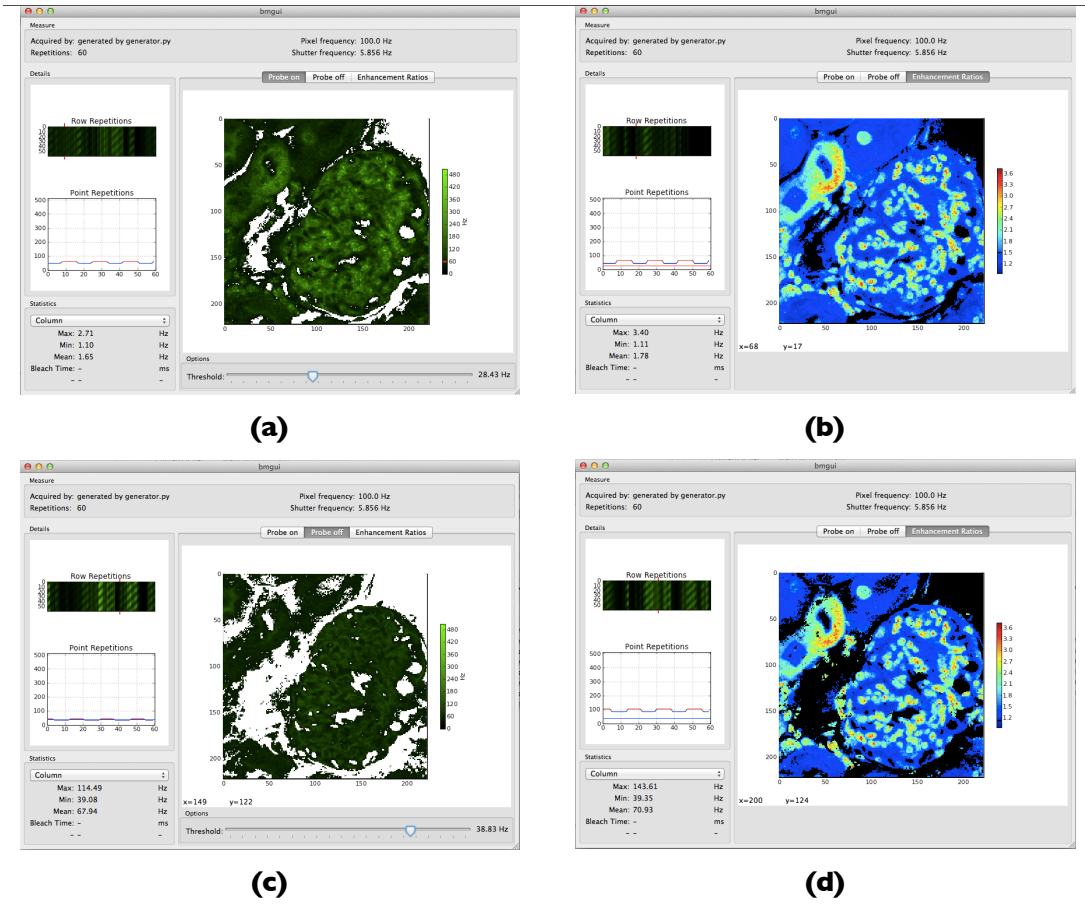

FIGURE 6.3: B.M. Analysis software: noise threshold setting. In Panel (A) the threshold set on the bright state image; in Panel (B) on the state image.

6.1.3 Threshold Setting

The software itself allows the user a luminosity threshold setting for the noise correction. This threshold can be set both on the bright and dark state image in a photon count range between 0 and 50% of the intensity range of the image itself (see Figure 6.3). The pixels in the intensity images that are discarded by the threshold are reported in black color in B.M. image, hence clearly distinguishable from the coloured ones.

6.2 Applications

6.2.1 Artificial Patterns

The first application of the analysis software was on artificial patterns created with the finality of extensively testing the functionality and the real capabilities not only of the software itself but also of the coupled acquisition/analysis protocol.

6.2.1.1 Why Using Artificial Patterns

The great utility of the artificial patterns is to input the analyzing software a B.M. raw-image, custom-created starting with a well defined geometrical pattern.
This image are by definition completely deprived of acquisition problems (both connected to the experimental setup and the biological sample quality), whereas the noise can be introduced in a proportion completely definable *a priori*.
The analysis of this patterns via the B.M. Analysis Software offered us with two main advantages:

- During the sw development, the analysis of the artificial patterns was a simple way to have a proof a principle that the software was actually doing what it was intended to do. The same thing would be far more difficult to realize with a real acquired image since it would have meant the performing of an handmade analysis of the same image in order to prove the sw calculations were correct.
- Analyzing with the final version the artificial patterns, gave us the possibility to test and stress the actual robustness of the B.M. analysis method. This was done simply by varying the noise level of the image and evaluating how much the reconstructed pattern differed by the real one. This was actually a fairly important evaluation to be done since in case of a bad result the idea of the implementability of such an acquisition protocol on biological sample would have become pointless.

6.2.1.2 How the Artificial Pattern is Constructed

The artificial patterns are constructed starting from two image matrixes reporting the desired sample pattern with the pixel filled with a custom defined photon rate corresponding to the standard (corresponding to pump only excitation) and enhanced (pump + probe excitation) fluorescence condition.
Starting from this two images and gave the input of the two B.M. frequencies, a dedicated software reconstruct the B.M. raw data image matrix mimicking the subsequent

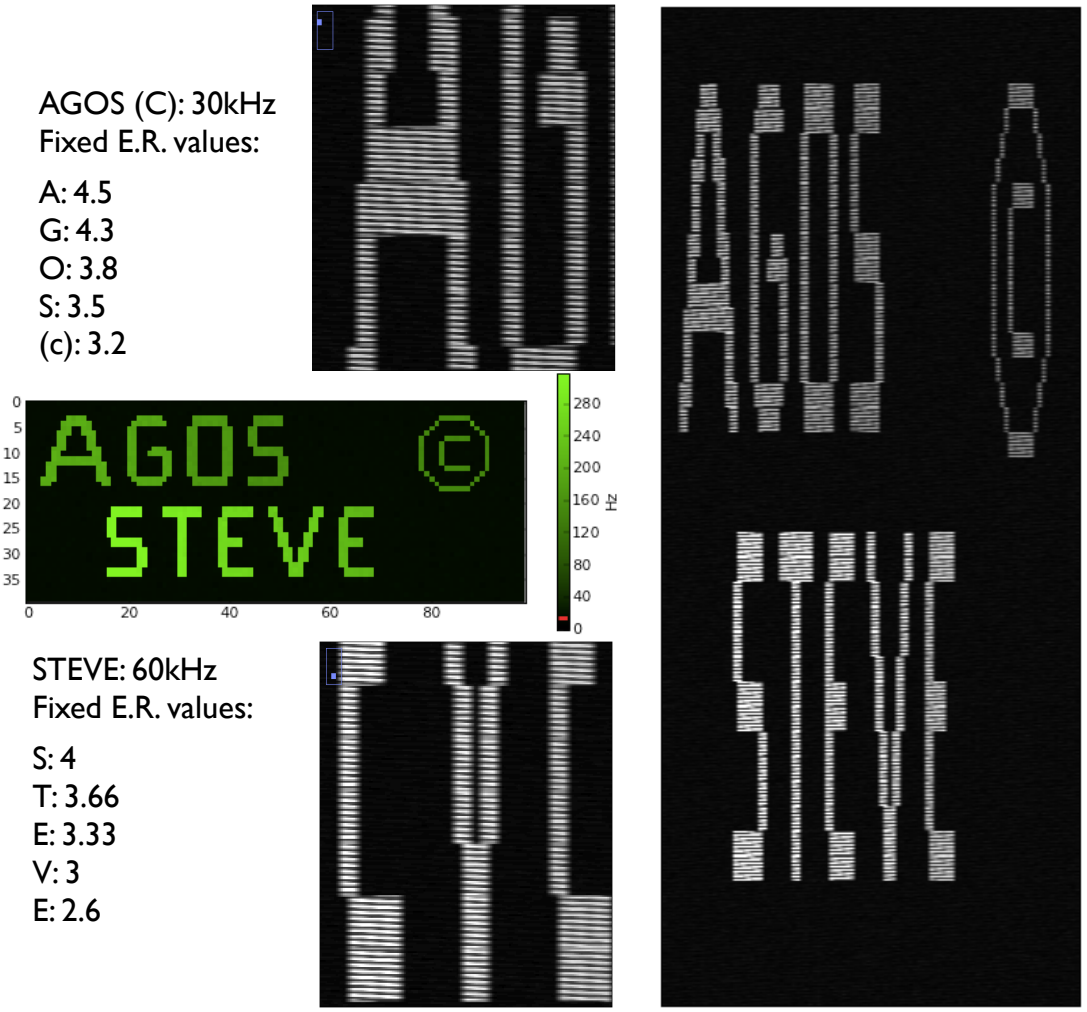

FIGURE 6.4: Example of an artificial pattern created for the validation of both the software and the acquisition protocol. In the colored panel the created pattern represented here as an image of the pump+probe excitation condition: the first word is characterized by a higher luminosity (60kHz in the pump only case) than the second one (30kHz in the pump only excitation case). Every letter on both words is characterized by a different E.R. as defined by the text inset.
On the right the artificial pattern reconstructed as a B.M. acquisition raw data image and ready to be analyzed by the Beating Mode Analysis Software described in the previous Section.

acquisition repetitions on the same line with the delay in the dark bright fringes imposed by the choice of ν_L and ν_S.

After the definition of the sample pattern, the noise is added to the images[5] following the following two algorithm:

- Background **White Noise**: On all the pixel of the image a white noise is added as extracted by a gaussian distribution with custom defined mean value and standard

[5] Always by the same dedicated software.

deviation. The first represents the image-noise-offset[6], while the latter represents the amplitude of the excursion of the white noise phenomenon. The range for both values has been estimated in our laboratory by performing test acquisitions.

- Fluorescence **Statistical Noise**: At every pixel corresponding to the sample pattern and hence contributing with a fluorescence signal is summed the contribution to the noise to the signal itself due to the Poisson statistics. The value to be summed was extracted by a normal distribution centered in zero and with std deviation equal to $1/N$ where N is the magnitude of the fluorescence signal of the particular pixel.

Varying the initial luminosity of the parent images and tuning the parameters of the noise addition, it is possible, using this artificial patterns to test the response of the acquisition and analysis method[7] to close-to-real case scenario, still being able to have a term of confrontation between the reconstructed and the actual shape of the sample. An example of the artificially reconstructed B.M. raw data image is reported in Figure 6.4

6.2.1.3 Data Analysis

The analysis of the artificial patterns (beyond the validation of the analysis software) gave us important information on the limits of the B.M. raw data analysis in terms of both noise correction and E.R. resolution. In Figure 6.5 we report some of the analyzed pattern in which the white noise was deliberately set quite high in order to test the actual efficiency of the threshold process in the pattern detection in a raw data analysis. The mean value of the gaussian distribution (i.e. the offset noise, see previous Section) was set to 15kHz and the σ-parameter of the Gaussian distribution was also set to 15kHz. This values actually represents an overestimation by a factor 3 of the noise characteristic of our experimental setup.

From the images collected in Figure 6.5, the following can be state:

- In the represented case the white noise contributes to the image, in the no pattern pixel, with a variable E.R. comprised between 1 and 3 (Figure 6.5(A)). From this stem the need for a noise threshold setting: in Figure 6.5(B) the noise setting is set on the bright (pump+probe excitation condition) image to 30kHz. In this ideal case the threshold filters all the pixels that are not part of the pattern.

[6] This can be related, in the laboratory world, to both the experimental and acquisition setup, characterizing the basic quality of the image.

[7] And not only of the software

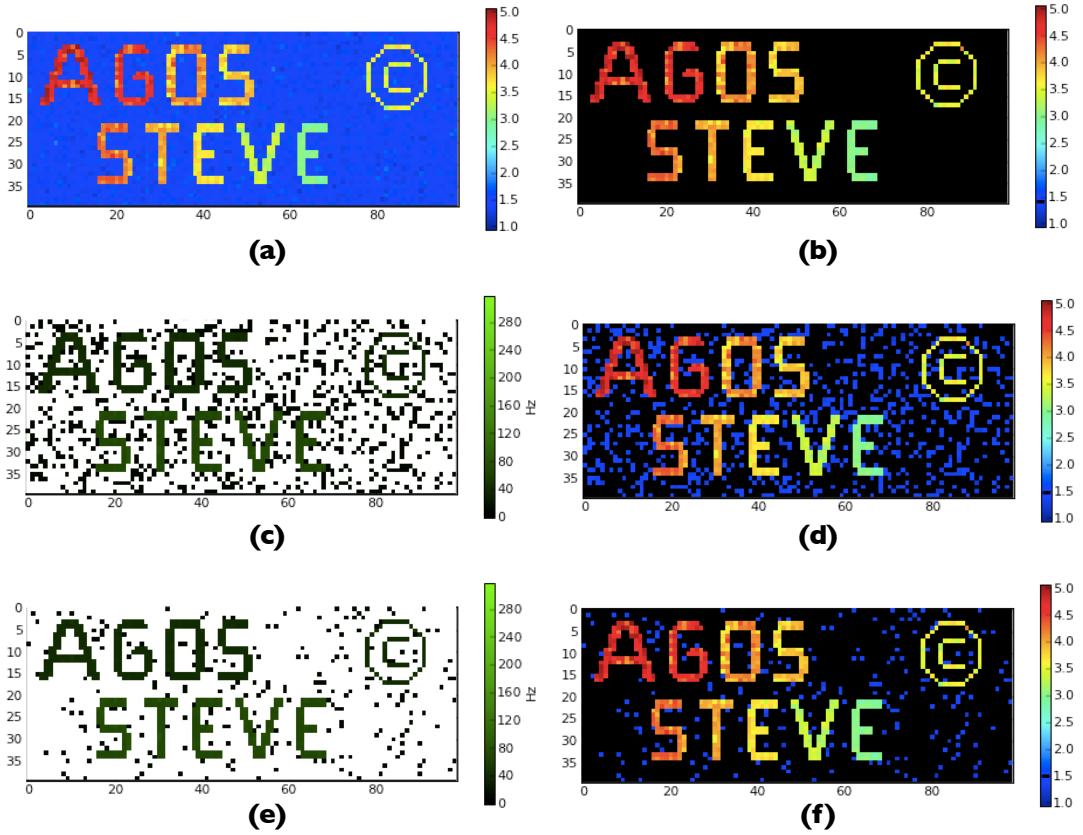

FIGURE 6.5: Analysis of Artificial Pattern. In Panel (A) the straightforward analysis of the pattern defined in Figure 6.4. In Panel (B) the image is filtered with a 30kHz threshold set on the bright-state image: the different ranges on the fluorescence and noise signal allows a perfect filtering of the noise.
In panel (C) a 15kHz threshold set on the dark-state image and the corresponding B.M. image in Palen (D). The same for a 25kHz threshold in Panel (E) and (F) respectively. Also in this case the pattern is visible after the filtering giving an ulterior validation to the acquisition and analysis protocols.

- The present threshold case is actually an ideal case since the white noise and the fluorescence signal in the specific case actually belonged to different ranges, hence the filtering can be perfect.

  In order to evaluate how the noise filtering works, in more subtle cases in which the white noise and the fluorescence signal have the same magnitude, the same threshold setting is performed on the dark image (pump only excitation condition). In this case (particularly for the *STEVE* word, characterized by a 30kHz signal) the fluorescence photon count and the white noise signal are of the same order.

  For both a threshold set of 15kH (Figure 6.5(C) and (D)) and 25KHz (Figure 6.5(E) and (F)), the pattern is still clearly identifiable in the analyzed images. This gives the B.M acquisition and analysis protocol further value as an applicable method in biological imaging.

- The effect of the Poisson Statistical noise affects the sensitivity in the E.R. calculation by a significant factor: inside the same letters[8] it is possible to find a E.R. excursion up to ±0.5. For this reason it may be suitable for this kind of measurements to map the photo properties of a chromophore characterized by a large E.R. range value along the desired spectrum of the physical properties(see Section 5.4.1.2).

[8] each one characterized by a particular E.R.

6.2.2 Experimental Data

The first preliminary experimental application of the B.M. acquisition and analysis protocol has been carried out on samples of GFP E222Q and Mut2GQ incapsulated in both latex micro spheres and Escherichia Coli bacteria.
Due to the not optimal condition of our image acquisition setup (resulting in an longer acquisition time, see Section 5.4.2), the preliminary B.M. images, presented in this Section, will be characterized by a different resolution along the x and the y axis of the images. This because of the effect of the bleaching: the longer scanning time results in a greater damaging effect of the sample that affecting a large part of the sample, proportional to the PSF of the optical excitation setup (see Section 2.1.2.1). The spatial extension of the phenomenon gives origin to a degeneration of the sample in the area to be scanned by following lines. In order to avoid, in the acquired image, this effect the μ-step in the y direction, separating the subsequent acquired lines, has to be kept high enough: 3/10μm.

For starter, let's focus on two images, one acquired on the GFP-incapsulating latex spheres (Figure 6.6) and the other on the marked Escherichia Coli bacteria (Figure 6.7).

At title of exemplification of the practice of the B.M. acquisition and analysis protocol, let's focus on the latter. The square image on the bottom is the standard acquisition of a part of the sample (30x30μm^2 with a scanning step of 200nm, resulting in a 150x150 pixel^2 image) obtained only with the pump probe impinging on the sample. Of this image, we select to focus on the detail outlined by the red line and reproduced in the second panel from the bottom: the selection is an area of 10x25μm that was acquired with B.M. protocol with a resolution of 100nm on the x and 5μm on the y. The detail of the B.M. acquisition with 60 repetitions per lines is reproduced in the third panel from the bottom. As visible, the two B.M. frequencies $\nu_L = 1$Hz and $\nu_S = 5.856$Hz were chosen in order to obtain a single complete dark-bright transition for each x pixel of the image.
From the analysis of this B.M. raw data image we obtain the reconstruction of the sample portion in both the dark (pump only excitation) and bright (pump+probe excitation) case. Finally in the top right panel the analyzed B.M. image in which the color-scale indicates the E.R. calculated on each pixel.
In this way we were able to map the E.R. of a detail of the bacteria, proportional to the intracellular pH. Quickening the sample scan it will be possible to reconstruct images of the full bacteria by lowering the effect of the bleaching and selecting a smaller y-step.

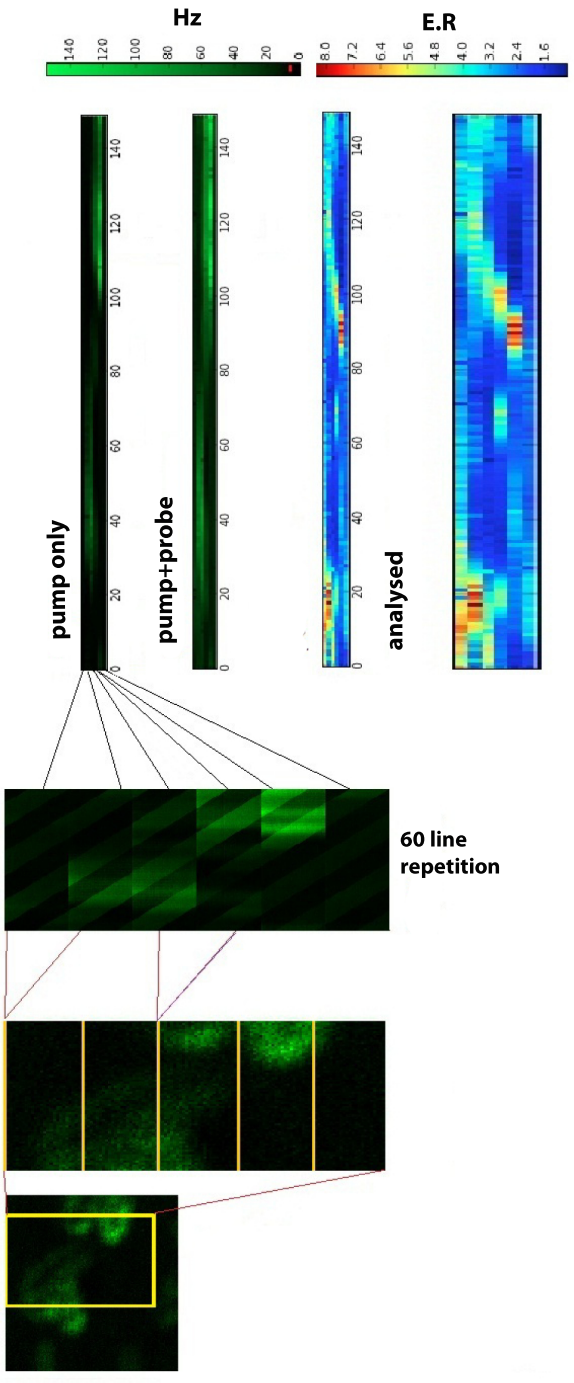

FIGURE 6.6: B.M. image of latex spheres with GFP E222Q incapsulated on the surface.

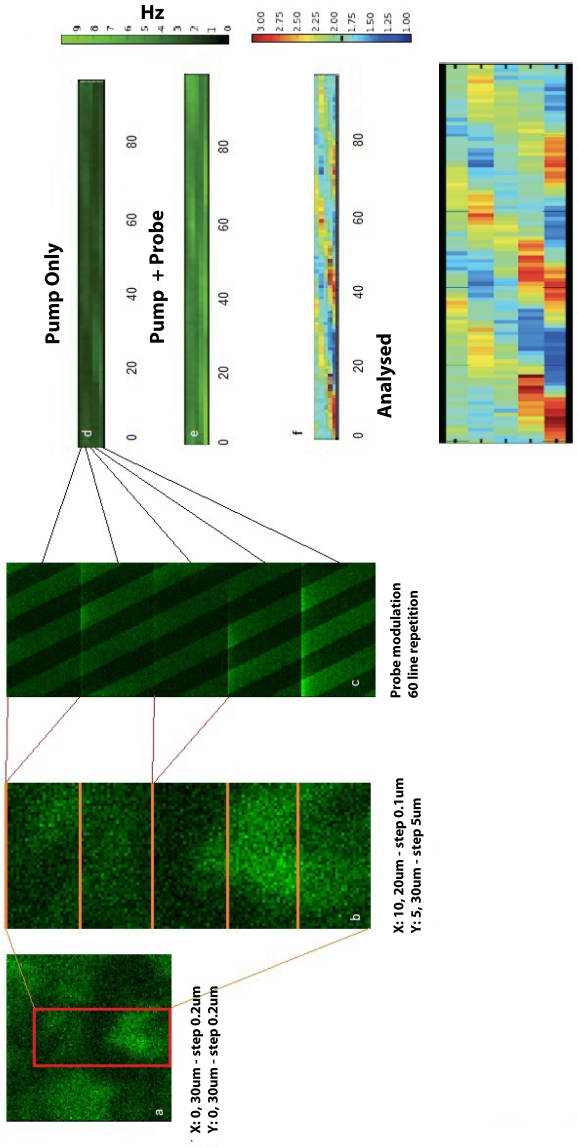

FIGURE 6.7: B.M. image of Escherichia Coli bacteria incapsulating GFP E222Q.

The same image reported in Figure 6.7 has also been acquired with a larger number of repetitions per lines (from 60 to 90). This should allow a better estimate of the E.R. since, not having changed ν_S and ν_L, for each pixel is mapped more that a single dark-bright transition. Anyway, as it is clear from the image reported in Figure 6.8 the longer acquisition time caused a massive photobleching and photodamaging of the sample (see Section 5.4.2): this causes a visible lowering of the luminosity of the pump+probe image (from 9 to 6Hz) and a consequent reduction or the enhancement ratio(from 3 to 2.5).

The result of this, as can be realized observing Figure 6.8, is a dramatic lowering of the image quality. The excessive impact of the noise causes a flattening of the image both in

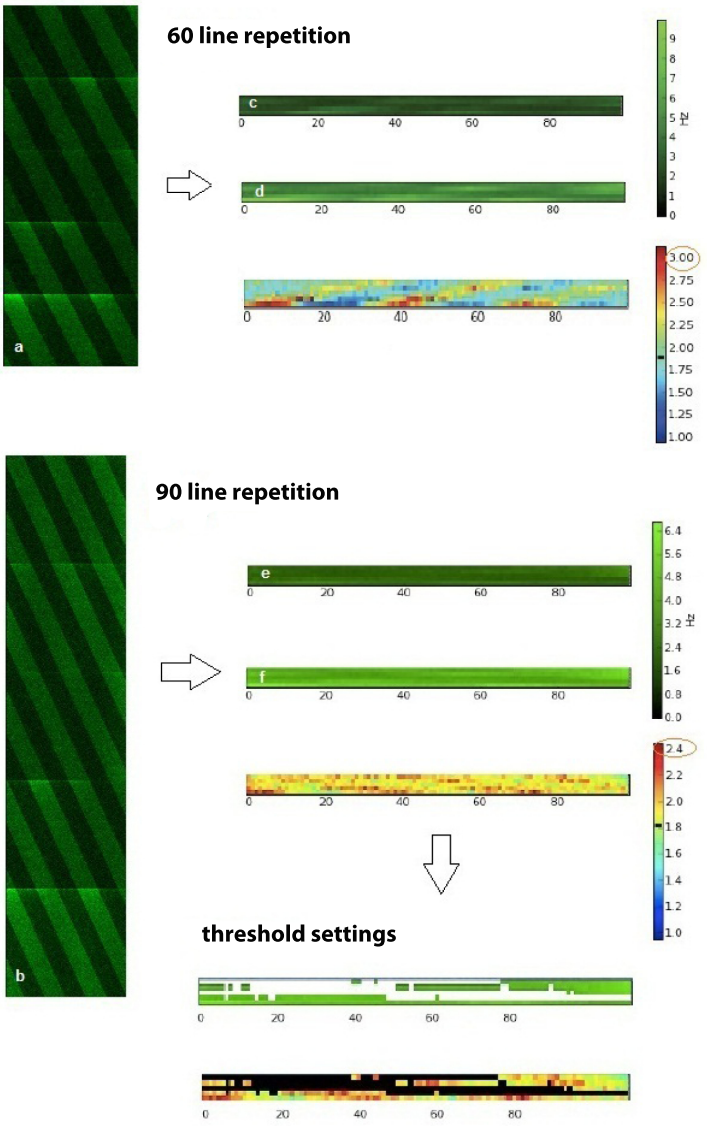

FIGURE 6.8: B.M. images of the same sample varying the number of repetitions per line: 60 vs 90. Here the B.M. frequency setting ($\nu_S = 5.856$Hz and $\nu_L = 1$Hz) forced a quite longer acquisition time and hence a huge impact of the photobleaching and photodamaging of the biological sample. In this case the increment of the repetitions per line has a greater impact in the degradation of the image quality. This loss of quality is clearly visible in the greater noise level of the image and in the fact that even the threshold setting in the 90-repetitions case is not able to show the same pattern visible in the 60-repetitions case.

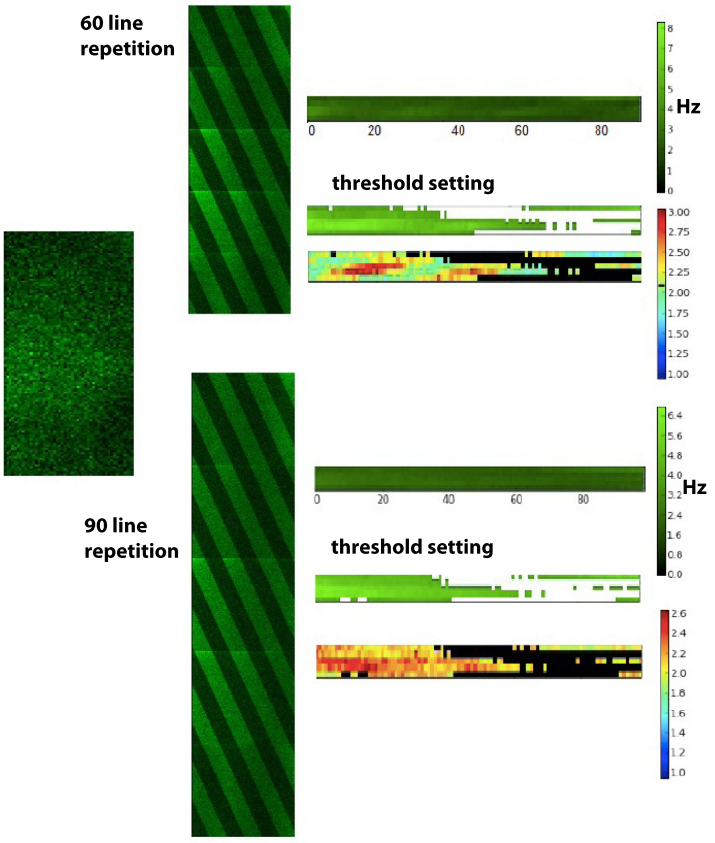

FIGURE 6.9: B.M. images of the same sample varying the number of repetitions per line: 60 vs 90. The faster frequency settings, $\nu_S = 58.56$Hz and $\nu_L = 10$Hz, allow a faster image acquisition and hence less photobleaching and photodamaging of the sample. The quality of the image is better then the previous case reported in Figure 6.8, but the E.R. pattern is still better defined for the case with 60 repetitions per line

term of intensity and E.R. image. The application of a noise threshold helps in filtering most of the false E.R. contribution to the image (see Section 5.4.1.1), but, also with this correction, the image quality (when compared to the first one) is still characterized by poor quality and a not complete definition of the biological pattern of the sample (Figure 6.8 lower panel).

The same thing has been done (and reported in Figure 6.9) on a another sample of marked Escherichia Coli. In this case, though, both the frequency ν_L and ν_S have been multiplied by a factor 10 with respect to the previous values. This allowed a faster acquisition and a less impact of the photobleaching and sample damaging.
The result in this case is way better than before: the two thresholded images have the same shape even if the E.R. pattern is still better defined for the case with 60 repetition per line (Figure 6.9).

In Figure 6.10 an example of a Mut2GQ marked bacteria. It is notable how both the fluorescence rate and the enhancement ratio are higher as characteristic of the particular mutant (see Section 4.1.2). Inspecting the E.R. B.M. image it is possible to identify the area of the sample where the pH is close to neutral value, corresponding to the pixels characterized by the higher values of the E.R.

Finally in Figure 6.11 we report an exemplification of an high resolution B.M. analysis in which the μ-step were equal to 200nm both for the x and y axis. The aim is to obtain a x-y homogeneously resolved B.M. analyzed image, this way it should be possible to outline in detail the particular structure of the sample.
Clearly the photobleaching and damaging of the sample is, in this case in particular, an ever present danger, that we tried to avoid by setting the B.M. frequency the fastest that our setup allowed: $\nu_S = 58.56$Hz $\nu_L = 10$Hz.
Unfortunately, this was not enough to prevent the photodamaging effect to mess with the image quality in terms of both noise and definition of the sample pattern on the collected image.
The only way we see to solve this issue is to implement the B.M. acquisition protocol on a scanning confocal setup reducing the acquisition time and allowing an interlacing of the repetition on subsequent line in order to diluite in time the effect of the bleaching per area (See Conclusions in the next Chapter).

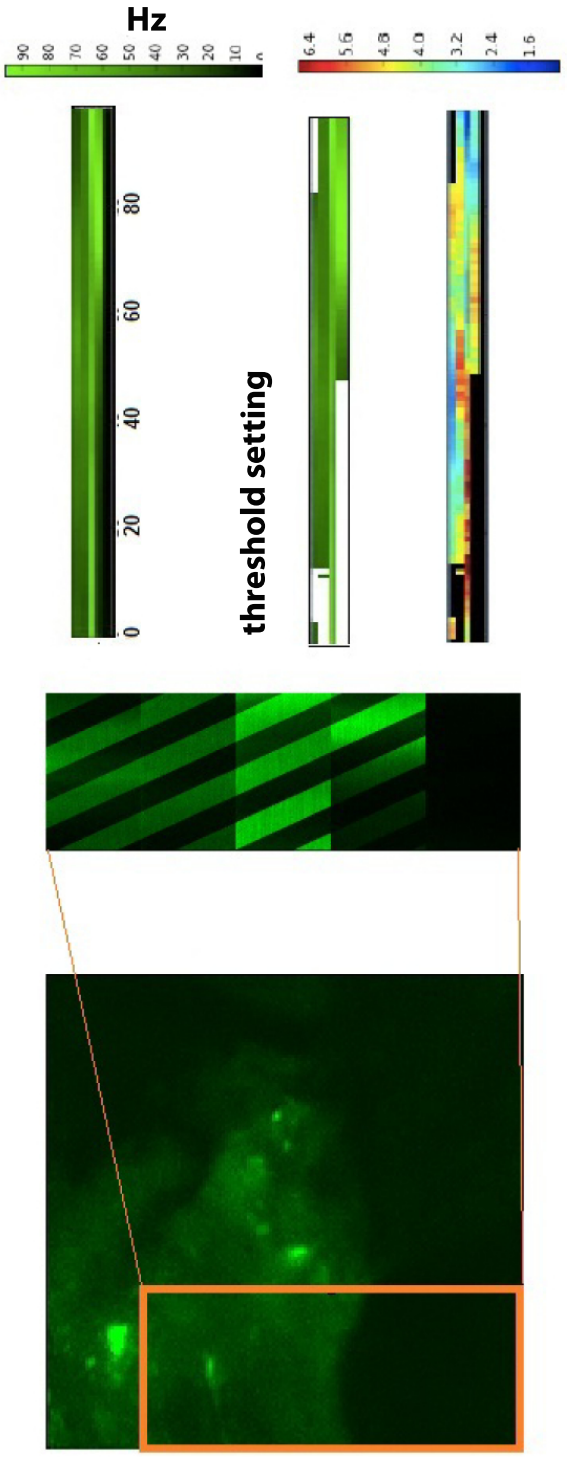

FIGURE 6.10: B.M. image of E-Coli bacteria marked with Mut2GQ. On the lower panel the standard fluorescence image of the sample with the B.M. analyzed area outlined. At the top of the Figure the two fluorescence images (dark and bright state) and the threshold setting. At top-right the B.M. E.R. image in which we can identify areas characterized by an high E.R. indicating zone of the sample where the pH is close to the neutral value.

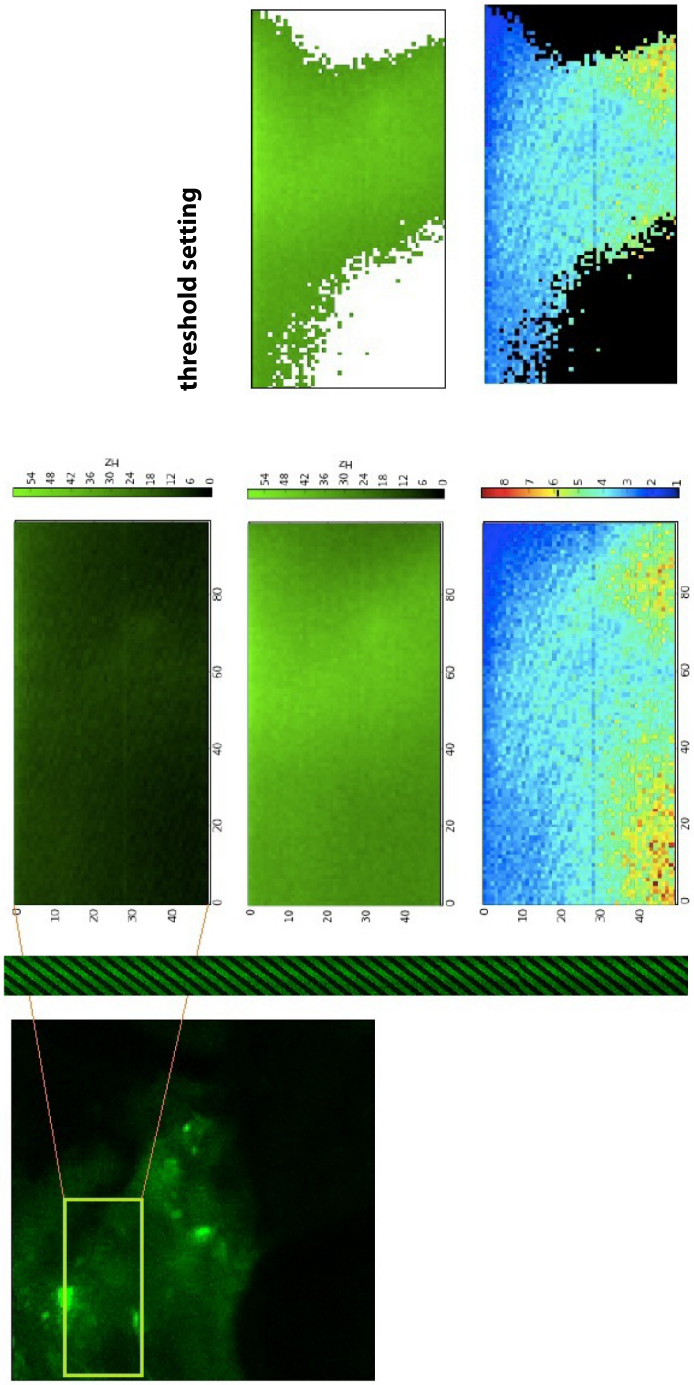

FIGURE 6.11: High resolution B.M. image: the acquisition was a failure in term of both noise and pattern definition due to the photobleaching and photodamaging effect as described in the text.

Chapter 7

Conclusions and Future Outlook

This study focused on photo-switching chromophores with particular attention paid to GPF Mut2 class mutants, E222Q and Mut2GQ.
These two mutants are derived from a common parent protein, GFP Mut2, a particularly bright folding mutant. They differ for the balance between the internal and external protonation of the chromophore that translates in a long lived dark state D [1] that in normal condition dumps the fluorescence yield of the molecule. The photo-switching properties stem from the possibility to trigger the depopulation process of the D state through the irradiation with a more energetic beam (the probe beam, see Section 3.3.2) with a wavelength that typically lies in the violet region of the optical spectrum[2].
The possibility to depopulate the D-state, implies that the fluorescence signal arising from the chromophore can be enhanced (*Enhancement Ratio*) and that this can be triggered and controlled by the probe excitation beam. Moreover, the population and depopulation lifetime of the dark state can be measured with pump + modulated probe excitation FCS experiments, as outlined in Section 3.3.2.1.
The actual, exploitable characteristic of the Mut2 class photo-switchable GFP mutants, on which this work is focused, is the dependence of the E.R. and the photo active times on physical properties of the surrounding such as pH, viscosity, temperature and so on. It is indeed the characterization of the photo-switching of these GPF mutants through FCS methods and the development of a statistical analysis method for slowly relaxing fluorescent states that constitutes the most fundamental contribution of this thesis. An innovative approach to imaging by exploiting the photo-switching properties of these mutants was then outlined and tested and will be the object of future developments.

In Sections 4.1.2 and 4.1.3, we present, respectively, the characterization of the Enhancement Ratio and the PhotoActive Times, of both the chromophore under study, as

[1] i.e. the neutral conformational state for the Mut2 mutants (see Figure 3.4).
[2] not actually contributing by itself to the $S_0 \rightarrow S_1$ excitation.

a function of pH and viscosity. It is particularly notable that the behavior of the E.R. is completely different for the two mutants, being characterized by a monotone trend for the E222Q (Figure 4.2) and a sharp peak for neutral pH for Mut2GQ (Figure 4.6).
A joint mathematical-simulative model has been developed in Section 4.2 in order to facilitate the study, via FCS analysis, of the properties of those chromophore with a dark-bright dynamics occurring on a time scale compatible with the brownian diffusion time τ_D.

The innovative proposal closing this work is what we called here Beating Mode: a new acquisition and analysis protocol suitable to obtain enhanced fluorescence images. As outlined in Chapter 5, this protocol is based on a multiple acquisition of each of the line of an raster scanning image, with slightly different dephasing between the probe laser beam modulation and the line scanning frequency. In this way it allows to exploit the photo-switching properties of the chromophore under study, in order to increase the information content of each pixel that represents not only the average brightness but also the E.R. and the photoactivation time of the chromophore (Section 5.1.2).
Due to the dependence of the E.R. and the PA.T. on the chemical and physical parameters of the protein mutants, the final goal of the B.M. protocol is to create functional maps of those physical properties of biological samples that influence the photo-switching properties of the chromophores: i.e. pH, viscosity, temperature, etc. (see Section 5.1.2)

In Chapter 6 we reported the state of the art of the new protocol, both in terms of the analysis software developed as a part of this work (see Section 6.1), the proof of principle of the protocol obtained from artificial pattern raw data images (see Section 6.2.1) and the first applications on biological samples (Section 6.2.2).

As often is the case in microscopy and spectroscopy, the increase in the image content implies longer acquisition time, during which the sample may suffer photobleaching and photodamaging phenomena. For this reason the current state of the art does not allow high resolution imaging (particularly on the y axis), as pointed out in Section 5.4.2
The strategies to fix this limitations, allowing a broader spectrum application of the B.M. protocol are at least two:

- The implementation of the protocol on a galvanometric mirror image acquisition system. This way not only the acquisition will be faster (as already pointed in Section 5.4.2), but the acquisition process can be optimized interlacing the line during the acquisition so that the photo damaging effect of the excitation can be better distributed on the sample reducing the local damaging effects[3].

[3]For example in a 50 line acquisition, with 60 repetitions per line, instead of proceeding in order of lines, the acquisition can be performed on line 1-26-2-27-3-.. and so on. This way the local area of the

- The engineering and development of the *synthetic* photoswitching chromophores that, while being characterized by the same D state dynamics (characterized in Section 4.1.2) of the GFP Mut2 mutants under study here, are less affected by the photobleaching and damaging phenomena, being less susceptible to energy deployment.

sample corresponding to line 1 is allowed to dissipate the heat deployed by the excitation, before being once again illuminated for line 2 acquisition.

Appendix A

Derivation of Equation 4.17

The Eqs. 4.17 can be cast into the form of a couple of coupled equations representing the dynamics between a bright state a and a dark state b for molecules diffusing in a solution, where the state a represent the fast lifetime states of the molecules (B and B^*) and the state b the dark long-lived state D. For this reason, let's define two new variables $u = c_{B_0} + c_{B^*}$ and $v = c_D$ for which the diffusion equations become Eqs. 4.18. In order to derive the functional form of the rates k_a and k_b we treat explicitly the case of spatially uniform rates. With this simplification Eqs.13 become:

$$\begin{aligned}
\frac{\partial}{\partial t}c_{B_0}(\vec{r},t) &= D\nabla^2 c_{B_0}(\vec{r},t) - \bar{k_{12}}c_{B_0}(\vec{r},t) + k_{21}c_{B^*}(\vec{r},t) + k_{31}c_D(\vec{r},t) \\
\frac{\partial}{\partial t}c_{B^*}(\vec{r},t) &= D\nabla^2 c_{B^*}(\vec{r},t) + \bar{k_{12}}c_{B_0}(\vec{r},t) - (k_{21}+k_{23})\,c_{B^*}(\vec{r},t) \\
\frac{\partial}{\partial t}c_D(\vec{r},t) &= D\nabla^2 c_D(\vec{r},t) + k_{23}c_{B^*}(\vec{r},t) - k_{31}c_D(\vec{r},t) \\
c_{B_0} &+ c_{B*} + c_D = N
\end{aligned} \tag{A.1}$$

where it is important to stress that the excitation rate, $\bar{k_{12}}$, is constant. This is equivalent to assume that the diffusion of the molecule through the excitation volume is much slower than the characteristic transition times between the different electronic states. In this case we should focus on the solution of the simple time differential equation:

$$\begin{aligned}
\frac{\partial}{\partial t}c_{B_0}(\vec{r},t) &= -\bar{k_{12}}c_{B_0}(\vec{r},t) + k_{21}c_{B^*}(\vec{r},t) + k_{31}c_D(\vec{r},t) \\
\frac{\partial}{\partial t}c_{B^*}(\vec{r},t) &= \bar{k_{12}}c_{B_0}(\vec{r},t) - (k_{21}+k_{23})\,c_{B^*}(\vec{r},t) \\
\frac{\partial}{\partial t}c_D(\vec{r},t) &= k_{23}c_{B^*}(\vec{r},t) - k_{31}c_D(\vec{r},t) \\
c_{B_0} &+ c_{B*} + c_D = N
\end{aligned} \tag{A.2}$$

It is now possible to rewrite the Eqs.A.2 as a couple of differential equations for the $u(t)$ and $v(t)$ variables, whose solution can be found as :

$$\begin{aligned} c_{B_0} &= A_{01}exp[-\lambda_0] + A_{02}exp[-\lambda_2] + A_{03}exp[-\lambda_3] \\ c_{B^*} &= A_{11}exp[-\lambda_0] + A_{12}exp[-\lambda_2] + A_{13}exp[-\lambda_3] \\ c_D &= A_{21}exp[-\lambda_0] + A_{22}exp[-\lambda_2] + A_{23}exp[-\lambda_3] \end{aligned} \tag{A.3}$$

where $\lambda_0 = 0$, $\lambda_1 = -k_{12} - k_{21}$ and $\lambda_3 = -\left(k_{31} + \frac{k_{12}k_{23}}{k_{12}+k_{21}}\right)$. Moreover the coefficients (eigenvectors) follow the relations:

$$\begin{aligned} A_{01} &= \frac{k_{21}k_{31}}{\Delta} & \Delta &= k_{12}\left(k_{23} + k31\right) + k_{21} + k_{31} \\ A_{02} &= \frac{k_{12}}{k_{12}+k_{21}} & A_{03} &= \frac{k_{12}k_{21}k_{23}}{\Delta\left(k_{12}+k_{21}\right)} \\ A_{11} &= \frac{k_{12}}{k_{21}}A_{01} \qquad A_{12} = -A_{02} & A_{13} &= \frac{k_{12}}{k_{21}}A_{03} \end{aligned} \tag{A.4}$$

Since the second eigenvalue, λ_1, corresponds to the anti-bunching process and is therefore of the order of GHz (approximately 1/lifetime), and we are interested in computing the correlation functions on time scales slower than microseconds, we can disregard the terms A_{02} and A_{12} in Eqs.A.3. In this case the $u(t) = c_{B_0} + c_{B^*}$ variable can be written in terms of c_{B_0} or c_{B^*} alone as:

$$u(t) = c_{B_0} + c_{B^*} \cong \left(1 + \frac{k_{12}}{k_{21}}\right) c_{B_0} \cong \left(1 + \frac{k_{21}}{k_{12}}\right) c_{B^*} \tag{A.5}$$

If we now rewrite Eqs.A.2 in terms of the two variables $u(t)$ and $v(t)$ and, taking into account the conservation of the number of molecules, we obtain:

$$\begin{aligned} \frac{\partial}{\partial t}u(\vec{r},t) &= -k_{23}c_{B^*}(\vec{r},t) + k_{31}c_D(\vec{r},t) \cong \\ &\cong -\frac{\bar{k_{12}}k_{23}}{k_{21}+\bar{k_{12}}}u(\vec{r},t) + k_{31}v(\vec{r},t) \\ N &= u(\vec{r},t) + v(\vec{r},t) \end{aligned} \tag{A.6}$$

If we now add to the above photo-induced relaxation process the diffusion of the molecules (for which we assume a common value of the diffusion coefficient Δ), we can write a set

of two coupled differential equations similar to Eqs. 4.18:

$$\begin{aligned} \frac{\partial}{\partial t}u(\vec{r},t) &\cong \Delta\nabla^2 u(\vec{r},t) - k_b u(\vec{r},t) + k_d v(\vec{r},t) \\ N &= u(\vec{r},t) + v(\vec{r},t) \end{aligned}$$

where

$$k_b = \frac{\bar{k_{12}} k_{23}}{k_{21} + \bar{k_{12}}}$$

and

$$k_d = k_{31}$$

A.1 Fraction of Dark Molecules in the Excitation Volume

Here is presented a derivation of the solution of the following steady state equation (see Eqs. 4.22):

$$\frac{\Delta}{r^2}\frac{d}{dr}\left[r^2\frac{d}{dr}\bar{c}_b(r)\right] - k_b\bar{c}_b(r) + \bar{k}_a(\bar{C} - \bar{c}_b(r)) = 0 \text{ if } r < L$$

In order to simplify these equations we introduce the function $\chi(r) = r\bar{c}_b(r)$. The term

$$\nabla^2\bar{c}_b(r) = \nabla^2\frac{\chi(r)}{r}$$

becomes

$$\frac{1}{r}\frac{d^2}{dr^2}\chi(r)$$

and the equations to be solved inside and outside the excitation volumes becomes respectively (A.7) and (A.8).

$$\Delta\frac{d^2}{dr^2}\chi(r) - k_b\chi(r) + r\bar{k}_a\bar{C} - \bar{k}_a\chi(r) = 0 \tag{A.7}$$

$$\Delta\frac{d^2}{dr^2}\chi(r) - k_b\chi(r) = 0 \tag{A.8}$$

Let's begin by solving equation (A.7). The homogeneous associated equations is:

$$\Delta\frac{d^2}{dr^2}\chi_{hom}(r) - k_b\chi_{hom}(r) - \bar{k}_a\chi_{hom}(r) = 0 \tag{A.9}$$

and has the solution reported in equation (A.10) where the substitution $l = \sqrt{\frac{\bar{k_a}+k_b}{\Delta}}$ has been made.

$$\chi_{hom}(r) = P_1\exp(-lr) + P_2\exp(lr) \tag{A.10}$$

Remembering that the concentration is $c_b(r) = \frac{\chi(r)}{r}$ in order to avoid a divergence of $c_b(r)$ for $r \to 0$ (which, being integrable, would be acceptable but physically meaningless) we chose $P_1 = -P_2$. The solution to the inhomogeneous equation is reported in Eq.(A.11):

$$\chi_{in}(r) = P \sinh(lr) + \bar{C}Tr \tag{A.11}$$

where $T = \frac{\bar{k_a}}{k_a + k_b}$. The solution of equation (A.8) is:

$$\chi_{out} = C_{11} e^{-mr} + C_{12} e^{mr} \tag{A.12}$$

In writing the outer solution (Eq.A.12) we have used the definition $m = \sqrt{\frac{k_b}{\Delta}}$. Plus, in order to avoid a divergence of the concentration for $r \to \infty$ the constant C_{12} must be taken equal to zero, so the solution results:

$$\chi_{out} = C_1 e^{-mr} \tag{A.13}$$

In conclusion the concentration function inside and outside the volume are:

$$\begin{aligned} \bar{c}_b^{(in)}(r) &= P\frac{\sinh(lr)}{r} + \bar{C}T \\ \bar{c}_b^{(out)}(r) &= C_1 e^{-mr} \end{aligned} \tag{A.14}$$

From the continuity condition for the concentration function at $r = L$ follows the condition,

$$P\frac{\sinh lL}{L} + \bar{C}T = C_1 \frac{e^{-mL}}{L} \tag{A.15}$$

whereas from the continuity condition of its derivative it follows the condition:

$$Pl\frac{\cosh lL}{L} - P\frac{\sinh lL}{L^2} = C_1(-m\frac{e^{-mL}}{L} - \frac{e^{-mL}}{L^2}) \tag{A.16}$$

From the above relations, the integration constant, C_1, can then be written as follows:

$$C_1 = Pe^{mL}\frac{1}{1+mL}(\sinh lL - lL\cosh lL) \tag{A.17}$$

and by inserting equation (A.17) in (A.15) we obtain the P parameter:

$$P = -\frac{(1+mL)\bar{C}T}{m\sinh lL - l\cosh lL} \tag{A.18}$$

Inserting the functional forms for P and C_1 in eq.(A.14) the concentration of the bright state of the chromophore inside the observation volume becomes:

$$\bar{c}_b^{(in)}(r) = \bar{C}T\left[1 - \frac{(1+mL)}{m\sinh(lL) - l\cosh(lL)}\frac{\sinh(lr)}{r}\right] \tag{A.19}$$

The ratio between the concentration of state b and the total concentration in the observation volume, $\bar{T}$, can be, then, obtained by computing:

$$\begin{aligned}\bar{T} &= \frac{\int_0^L d^3\bar{r}c(\bar{r})}{\int_0^L d^3\bar{r}\bar{C}} = \\ &T\left\{1 - \frac{3}{l^2L^3}\left[lL\cosh(lL) - \sinh(lL)\right]\left[\frac{(1+mL)}{m\sinh(lL) + l\cosh(lL)}\right]\right\}\end{aligned} \tag{A.20}$$

Appendix B

Effect of the beam shape on the simulated ACF

The fluorescence fluctuations autocorrelation function is largely determined by the fluctuations of the concentration of the molecule within the excitation/observation volume. The fluorescence fluctuations arise also from variations in the molecular brightness due to process concerning the chromophore excited state (photo-dynamics) and ground state (chemical reactions).

In experiments and, more important, in simulations several other phenomena may affect the shape of the ACF: spatially inhomogeneous ground state depletion, finite box size in periodic boundary conditions, shape of the excitation beam, are just a few examples. This section is devoted, in particular to the study of the effect of the beam shape on the ACF decay, by means of the simulation code described in the main text (Section XXXCITAZIONEXXX). This process also offers an indirectly validation test of the algorithm itself. For starters, it is important to distinguish between the *excitation laser profile* and the fluorescence spatial distribution in the focal volume (*fluorescence profile*). The former is the distribution of a dye excitation probability in the ground state which depends on the intensity distribution of the laser light and on the absorption cross section (ϵ). The *fluorescence profile* depends also on the space dependent probability to find the chromophore in the first excited energy level ($\cong S_1(\vec{r}, t)$).

B.1 Gaussian beam profile, One photon Excitation.

As a first approximation it is convention to assume that the excitation laser profile is 3D Gaussian $\rho_{G3D}(\vec{r})$:

$$\rho_{G3D}(x,y,z) = \frac{(\pi)^{-3/2}}{w_{xy}^2 w_z} exp\left[-2\frac{(x^2+y^2)}{w_{xy}^2} - 2\frac{(z^2)}{w_z^2}\right] \tag{B.1}$$

and therefore that the time integrated emission profile is:

$$F(x,y,z) = F_0^{OPE}\exp(-2(x^2+y^2)/\omega_{xy}^2)\exp(-2z^2/w_z^2) \tag{B.2}$$

The beam waist is $\omega_{xy} = 0.6\lambda(N.A.)^{-1}$, where $N.A.$ is the objective numerical aperture and w_z is evaluated empirically ($w_z \cong 5w_{xy}$) from the confocal setup. The position independent factor F_0 for the case of one photon excitation with chromophore cross-section σ_{OPE} is:

$$F_0^{OPE} = \frac{\sigma_{OPE}\Delta t\langle P\rangle\lambda}{(hc)\pi\omega_{xy}^2} \tag{B.3}$$

where Δt is the integration time (which in the simulation is the photodynamics time scale and experimentally is the sampling time of the detection electronics), λ is the radiation wavelength, $\langle P\rangle$ is the average laser power and h, π and c have the usual meaning. For the G3D fluorescence intensity profile represented by Eq.B.2 it is possible to compute[95] the fluorescence (diffusive only) autocorrelation function:

$$g(\tau) = g(0)\left(1+\frac{\tau}{\tau_\Delta}\right)^{-1}\left(1+\left(\frac{\omega_{xy}}{w_z}\right)^2\cdot\frac{\tau}{\tau_\Delta}\right)^{-\frac{1}{2}} \tag{B.4}$$

In Eq.B.4, the diffusion relaxation time is $\tau_\Delta = \frac{\omega_{xy}^2}{4\Delta}$ and the amplitude of the ACF is related to the average number $\langle N\rangle$ of molecules within the excitation volume or to their concentration, C, in the simulation box since $g(0) = \frac{\gamma}{C\cdot V_{exc}}$, where:

$$\begin{aligned} \gamma &= \frac{\int d\vec{r}\rho_{G3D}^2(\vec{r})}{\int d\vec{r}\rho_{G3D}(\vec{r})} = \frac{1}{\sqrt{8}} \\ V_{exc} &= \left(\frac{\pi}{2}\right)^{3/2}\omega_{xy}^2\omega_z \\ C &= \frac{\langle N\rangle}{V_{exc}} \end{aligned} \tag{B.5}$$

An example of the autocorrelation function simulated through the BD-MC algorithm described in the text is reported in Fig.(B.1). The parameters used for these simulations are reported in Table (B.1).

We have run ten simulations for a box volume $V_{box} = 135\mu m^3$ and for a total simulation

C	$1nM = 0.6 \left[\frac{molecules}{\mu m^3}\right]$
Δ	$90 \frac{\mu m^2}{s}$
σ_{OPE}	$4.5 \cdot 10^{-15} cm^2$
λ	$0.8\ \mu m$
ω_{xy}	$0.4\ \mu m$
ω_z	$0.63\ \mu m$
ϵ	1

TABLE B.1: Parameters used for the BD simulation for the G3D illumination volume: C, Δ and σ_{OPE} indicate respectively the concentration, the translational diffusion coefficient and the OPE absorption cross-section of the molecules. The light wavelength is λ; the beam waist parameters are ω_{xy} and ω_z calculated as a function of λ. The collection efficiency, ϵ, is here taken = 1.

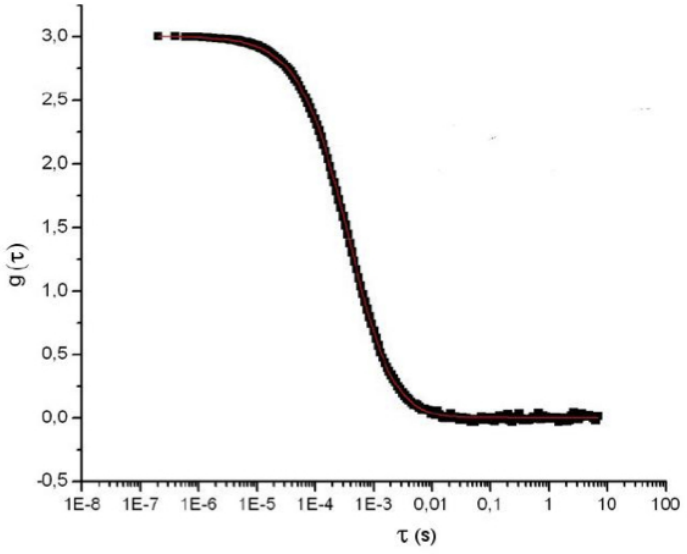

FIGURE B.1: Simulated pure diffusive autocorrelation function for the G3D excitation profile under OPE (Eq.B.2 and B.1) according to the parameters given in Table B.1.

time of 80s, with the parameters reported in the Table B.1. The result of the analysis of the simulated ACFs by means of Eq.B.4 are reported in Table (B.2) and show a very good agreement with the input simulation values.

B.2 Gaussian beam profile, Two photon excitation.

In the case of a two photon excitation process and with the 3D Gaussian laser profile approximation still holding, the time average fluorescence emission due to a pulsed laser

$\omega^2_{xy,input}$ $[\mu m^2]$	C_{in} $[\frac{molecules}{\mu m^3}]$	$\omega^2_{xy,fit}$ $[\mu m^2]$	C_{fit} $[\frac{molecules}{\mu m^3}]$
0.16	0.6	0.160 ± 0.002	0.597 ± 0.004
0.16	1.2	0.161 ± 0.002	1.19 ± 0.004
0.16	2.4	0.159 ± 0.002	2.39 ± 0.004

TABLE B.2: Best fit parameters of the analysis of the simulated fluorescence ACFs made according to Eq.B.4 and for varying G3D laser profiles. The standard deviations have been computed on ten different simulations.

beam of average power $\langle P\rangle$, repetition rate f_p and pulse duration τ_p is given by:

$$F(x,y,z) = F_0^{TPE}\left(\exp(-2(x^2+y^2)/\omega_{xy}^2)\exp(-2z^2/\omega_z^2)\right)^2 \tag{B.6}$$

The parameter F_0^{TPE} depends on the two-photon excitation cross-section σ_{TPE} as:

$$F_0^{TPE} = \frac{\sigma_{TPE}\lambda^2\Delta t 4\langle P\rangle^2}{\tau_p f_p (hc)^2\pi^2\omega_{xy}^4} \tag{B.7}$$

The factor 4 appearing in the above relation is due to the assumption that TPE occurs for a wavelength that is double the wavelength assumed for the OPE experiments. The fluorescence autocorrelation function can be analytically evaluated in this case as:

$$g(\tau) = g(0)\left(1+\frac{\tau}{\tau_\Delta}\right)^{-1}\left(1+\left(\frac{\omega_{xy}}{\omega_z}\right)^2\frac{\tau}{\tau_\Delta}\right)^{-\frac{1}{2}} \tag{B.8}$$

The zero lag time extrapolation of the ACF, $g(0)$, depends on the average number of molecules in the excitation volume: $g(0) = 2^{-\frac{3}{2}}/\langle N\rangle$. It is worth noting that, for a 3D Gaussian profile, the γ factor (Eq.B.5) is $\gamma = 2^{-2/3}$ even under two-photon excitation. $\langle N\rangle$ is related to the molecular concentration as $\langle N\rangle = \langle C\rangle V_{exc}^{TPE,G3D}$, where $V_{exc}^{TPE,G3D} = (\frac{\pi}{4})^{\frac{3}{2}}\omega_{xy}^2\omega_z$, and the diffusion time in Eq.B.8 is $\tau_\Delta = \omega_{xy}^2/(8\Delta)$.

The simulations were performed with a photodynamic time step of $dT = 10ns$ and a diffusion timescale of $dt = 200ns$. Such a choice of dT was required to reduce double excitation events, that are not accounted by the algorithm, as the average power was increased in the range $0.01 \leq \langle P\rangle \leq 0.05W$. The numerical values assigned to the other parameters are reported in Table B.3.

We have simulated the diffusion of proteins within boxes of different sizes and at various concentrations. The typical fluorescence ACF computed for a concentration of $C = 1nM$ and a box size of $5\times5\times5\mu m^3$ is reported in Fig. B.2. We have then analyzed the simulated ACFs by means of the theoretical functional form given by Eq.B.8 finding

τ_p	$2 \cdot 10^{-13}$ s
f_p	$8 \cdot 10^7$ Hz
$\langle P \rangle$	$0.01 - 0.05W$
σ_{TPE}	$3 \cdot 10^{-49} cm^4$
ϵ	0.05
ω_{xy}	0.4 - 0.66 μm
ω_z	1.55 μm

TABLE B.3: Parameters adopted for the simulation of the diffusive component of the ACF under two-photon excitation and with a 3D Gaussian laser beam profile. ϵ is the detection efficiency.

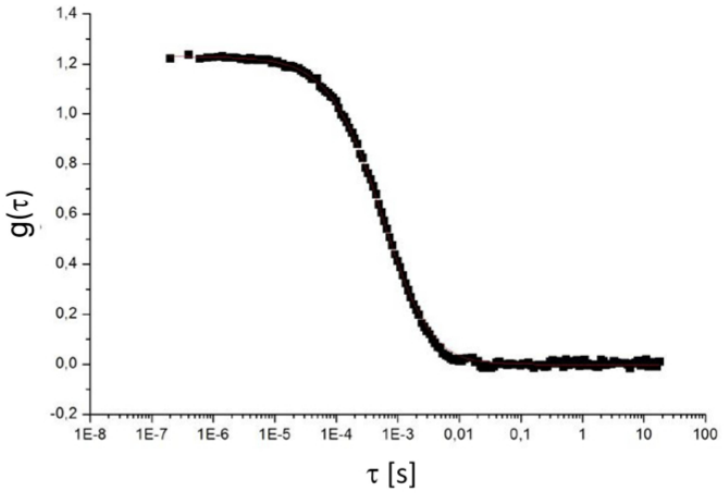

FIGURE B.2: Typical simulated pure diffusive autocorrelation function for the 3D Gaussian excitation profile under TPE (Eq.B.6 and 4) according to the parameters given in Table B.3 ($\omega_{xy} = 0.66 \mu m$). The solid line is the best fit curve (Eq.B.8).

best fit values of the beam waist and the molecular concentration in close agreement with the input ones (see Table B.4).

$\omega^2_{xy,input}$ $[\mu m^2]$	C_{in} $[\frac{molecules}{\mu m^3}]$	$\omega^2_{xy,fit}$ $[\mu m^2]$	C_{fit} $[\frac{molecules}{\mu m^3}]$	
0.16	0.6	5	0.160 ± 0.002	0.59 ± 0.01
0.44	0.6	3	0.43 ± 0.01	0.60 ± 0.01
0.44	0.6	50	0.44 ± 0.01	0.59 ± 0.01

TABLE B.4: Best fit parameters of the analysis (Eq.B.8) of the simulated fluorescence ACFs under TPE excitation mode, for varying G3D laser profiles and excitation power values. The standard deviations have been computed on ten different simulations.

B.3 Gaussian-Lorentzian intensity distribution, Two photon excitation.

The Gaussian-Lorentzian (GL) profile is physically the most significant profile for laser optical focusing. In fact the lowest order mode of the electric field propagating from the center of a resonant cavity, the TEM_{00} mode, corresponds to the following functional form of the intensity:[96]

$$\begin{aligned} I(x,y,z) &= I_0 \left(\frac{\omega_0}{\omega(z)}\right)^2 \exp\left[-2\frac{r^2}{\omega^2(z)}\right] \\ \omega(z) &= \omega_0 \left[1+\left(\frac{z}{z_0}\right)^2\right]^{1/2} \end{aligned} \tag{B.9}$$

The Lorentzian dependence of the laser beam intensity is determined by the z_0 parameter, $z_0 = \pi\omega_0^2/\lambda$. The laser beam waist ω_0 is determined by the confocal cavity parameters (mirror curvature radii) or the numerical aperture of an aberration free optics. It must be noticed that for the GL beam profile the axial decay of the intensity is much slower than for the 3D Gaussian one: therefore the simulation of the amplitude of the fluorescence ACF, that depends on the number of the molecules diffusing through the excitation volume, is particularly critical: in order to count correctly $\langle N \rangle$ we should simulate with much larger box sizes than in the 3D Gaussian case.

Since a larger simulation box means a longer CPU time required, we have estimated the minimum size of the box to be used to reproduce the ACF amplitude with a reasonable accuracy ($\leq 3\%$) by running simulations for a fixed set of beam parameters (see Table B.5) but for increasing box size (see Table B.6).

Due to the slow (not integrable) decay of the excitation probability along the axial

τ_p	$2 \cdot 10^{-13} s$
f_p	$8 \cdot 10^{7} Hz$
$\langle P \rangle$	0.003 W
σ_{tpa}	$3 \cdot 10^{-49} cm^4$
ϵ	1
ω_0	0.397 μm
z_0	0.55 μm

TABLE B.5: Parameters assumed for the simulation of the diffusive component of the ACF under two-photon excitation and with a Gaussian-Lorentzian laser beam profile. ϵ is the detection efficiency taken arbitrarily equal to 1.

direction, the total number of excited molecules in a simulation is underestimated for any finite size box. A first estimate of the underestimation of the total number of

L_xxL_yxL_z [μm^3]	N_{tot}	$N_{tot}/N_{tot,\infty}$
2x2x20	733459	0.84
4x4x30	800514	0.92
6x6x40	827063	0.95
8x8x50	840806	0.96
10x10x60	849030	0.97
12x12x70	854457	0.98
14x14x80	858055	0.98
16x16x90	860522	0.99
18x18x100	861689	0.99

TABLE B.6: Values of the total number of excited molecules per simulation as a function of the size of the simulation box. The third column report the ratio of N_{tot} to the plateau value obtained from the fit of the data to Eq. B.10.

molecules diffusing through the excitation volume has then been obtained by counting the total number, N_{tot} of excited molecules detected during the simulations as a function of the different box sizes. We expect that the major effect on N_{tot} is that of the axial size of the box, L_z, as indeed found in Fig.B.3. The observed trend can be fit to the following functional form:

$$N_{tot} = N_{tot,\infty}\left[1 - \left(\frac{L_{z,\infty}}{L_z}\right)^{\alpha}\right] \tag{B.10}$$

From this fit (Fig.B.3), a plateau value of $N_{tot,\infty} = 872463 \pm 380$ for the total number of excited molecules can be extrapolated, that corresponds to approximately 0.1 % of excitation efficiency ($L_{z,\infty} = 6.4 \pm 0.05\mu m$ and $\alpha = 1.62 \pm 0.01$).

The total number of excited molecule N_{tot} as a function of the z extension of the box size L_z and its ratio to the limit value $N_{tot,\infty}$ are also reported in Table B.6. From these data set we chose a box size of $12 \times 12 \times 70\mu m^3$, that corresponds to a 2 % underestimation of N_{tot}, to run simulations of the fluorescence ACFs. To this purpose we assumed different concentrations and ω_0 values while keeping the other simulation parameters as in the Table B.5.

An example of the autocorrelation function simulated with the parameters reported in the Table B.5 is shown in Fig.B.4. The fitting function of these ACFs must be chosen carefully. In fact it is possible to approximate the Gaussian-Lorentzian (GL) profile with a G3D profile, and to fit, with a very good accuracy ($\chi^2 = 0.99$), the simulated ACFs with the simple analytical function given by Eq. B.4 or Eq.B.8. However, an analytical approximation of the ACF for the Gaussian-Lorentzian profile has been recently derived:[97]

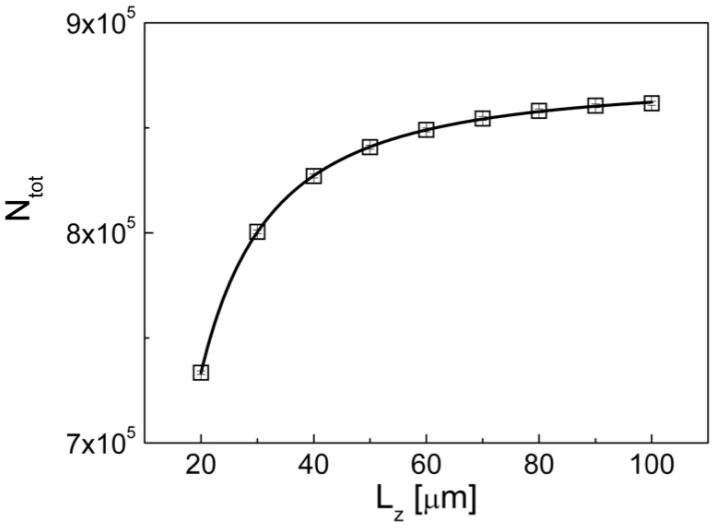

FIGURE B.3: Total number of excited molecules per simulation as a function of the z extension, L_z, of the simulation box. The Poisson uncertainty on the data is within the size of the symbols. See also Table B.6. The solid line is the best fit of Eq.B.10 to the simulated data. The best fit parameters are $N_{tot,\infty} = 872463 \pm 380$, $L_{z,\infty} = 6.4 \pm 0.05 \mu m$ and $\alpha = 1.62 \pm 0.01$.

$$\begin{aligned} g(\tau) &= g_{GL}(0)\frac{2^{9/2}}{3\pi^{3/2}}\frac{\beta}{\sqrt{\tau/\tau_\Delta}}L_\beta(\frac{\tau}{\tau_\Delta}) \\ g_{GL}(0) &= \frac{3}{16CV_{exc,GL}} \quad ; \quad \tau_\Delta = \frac{\omega_0^2}{8\Delta} \\ V_{exc,GL} &= \pi^3\frac{\omega_0^4}{4\lambda} \quad ; \quad \beta = \frac{z_0}{\omega_0} \end{aligned} \tag{B.11}$$

The function $L_\beta(t)$ is a tabulated special function that can be written as a combination of complex error functions.[97] In order to fit Eq.B.11 to the data, a first order approximation of the analytical solution, also derived in [97] can be used:

$$g(\tau) = g_{GL}(0)\frac{4\tau_\Delta}{3\tau}\left[1 + 2\frac{\tau_\Delta}{\tau}\left(\frac{1}{\sqrt{1+\tau/\tau_\Delta}} - 1\right)\right] \tag{B.12}$$

This function approximates very well the simulated ACFs as shown in Fig.B.4, in which the solid line represents the best fit of Eq.B.12 to the simulated ACF. We have then performed a study of the possibility to simulate the ACFs with a GL laser profile and under two-photon excitation, as a function of the beam waist, ω_0. The best fit value of ω_0, obtained by applying the functions given by Eq.B.12) ($\omega_{0,fitGL}$) or Eq.B.8 ($\omega_{0,fitG3D}$) to the simulated ACFs, are plotted as a function of the input simulation value, $\omega_{0,input}$ in Fig.B.5.

The values of the beam waist obtained by fitting the simulated ACFs by means of Eq.B.12 are close (within $6 \pm 1\%$) to the input value (see Table B.7). This result is

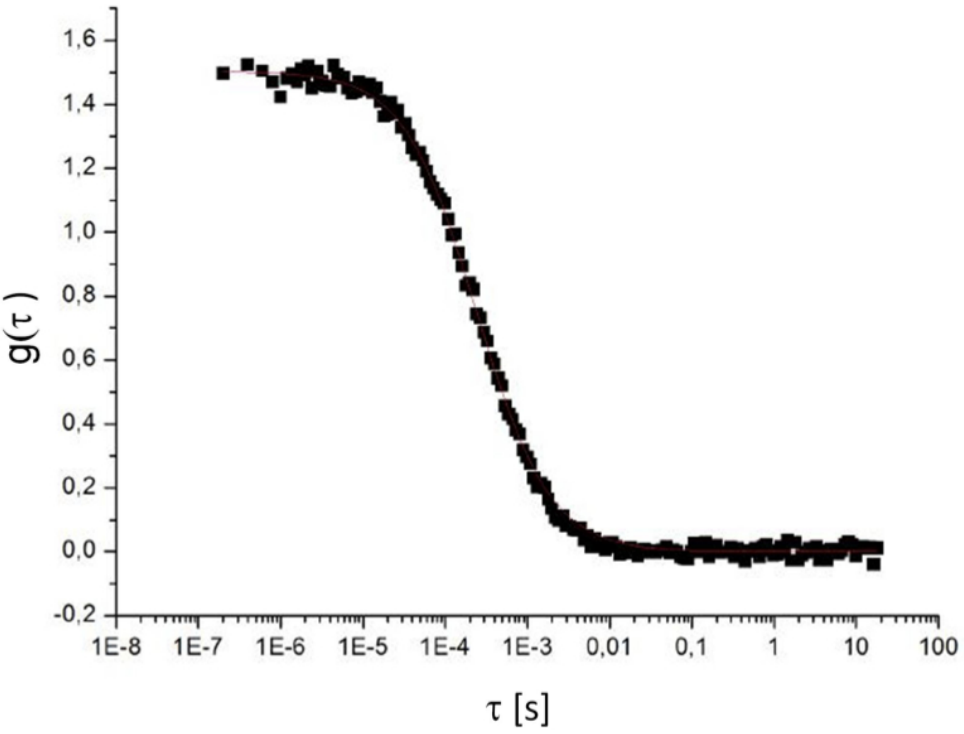

FIGURE B.4: Simulated pure diffusive autocorrelation function for the Gaussian-Lorentzian excitation profile under TPE (Eq.B.9) according to the parameters given in Table B.5. The solid line is the best fit of Eq.B.12 to the simulated ACF.

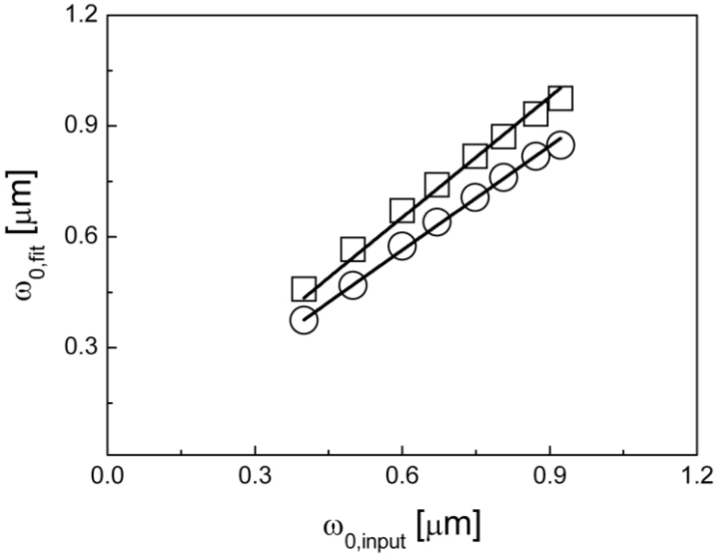

FIGURE B.5: Dependence of the best fit beam waists $\omega_{0,fitGL}$ (open circles) and $\omega_{0,fitG3D}$ (open squares) on the input beam waist, $\omega_{0,input}$ for the simulations of the ACFs for a GL laser profile and under TPE. The solid lines are the linear best fit curves that corresponds to slopes 0.94 ± 0.006 (for Eq.B.12,circles) and 1.09 ± 0.01 (for Eq.B.8, squares).

better than that obtained by fitting the simulated ACFs by means of Eq.B.8, that corresponds to an agreement of $10 \pm 1\%$. The systematic underestimation of the beam waist resulting by using Eq.B.12 should be due to the approximations that led to Eq.B.12 from Eq.B.11.

$\omega_{0,input}$	$\omega_{0,fit3DG}$	$\omega_{0,fitGL}$	$\omega_{0,fit3DG}/\omega_{0,input}$	$\omega_{0,fitGL}/\omega_{0,input}$
0.400	0.458	0.374	1.146	0.935
0.500	0.566	0.469	1.131	0.938
0.600	0.671	0.574	1.118	0.957
0.671	0.742	0.640	1.105	0.954
0.748	0.818	0.707	1.094	0.945
0.806	0.872	0.761	1.081	0.945
0.872	0.933	0.818	1.070	0.939
0.922	0.974	0.848	1.057	0.920

TABLE B.7: Beam waist of the laser profile in μm. The first column is the input value for the simulation ($C = 1nM$ for all the simulations). The second and the third columns report the best fit values obtained by using Eqs.B.8 and B.12, respectively. The last two columns report the discrepancy between the input and the best fit values.

Appendix C

Optical and Experimental Setup

In this appendix a description of the experimental setup, from the laser source up to the photo-multipliers tubes (PMTs) that detect the signal, will be presented.

C.1 Laser Sources

C.1.1 Stimulated Emission and Laser Basics

The word laser is the acronym for Light Amplification by Stimulated Emission of Radiation. While any thermal emitter, such as the sun, irradiates light in any direction without a defined phase relation, lasers are light amplifiers: all the photons emitted have the same phase and direction.
The emitted beam is then highly directional, monochromatic and coherent (Sironi[98]).

C.1.1.1 Light Amplification by Stimulated Emission

As said in Section 1.1, the stimulated emission occurs when an excited atom is hit by a photon carrying exactly the energy of the gap in the electronic structure of the atom itself. In this case the electron is triggered to fall to the ground state while the atom emits two photons characterized by the same polarization state, direction and phase.
Since the probability $B_{n,m}$ of having stimulated emission is strictly equal to the absorption probability $B_{m,n}$, the discriminating parameter between the two processes is the population ratio between the two levels.
A modeling of the number of photons as a function of the propagation distance z inside

the medium[1] is given as[5]:

$$n(z) = n_0 e^{(N_2 - N_1) b_{1,2} z} \tag{C.1}$$

where $n_0 = n(0)$ is the number of photons impinging on the medium, and $b_{1,2}$ is related to the Einstein coefficient.
It is now trivial to see that:

- When $N_1 > N_2$ the expression C.1 simply reduce to the usual Beer-Lambert law for the absorption.
- When $N_1 = N_2$ the number of photons remains constant along the propagation distance. In this case elementary absorption and stimulated emission processes are balanced due to the fact that $B_{n,m} = B_{m,n}$
- When $N_2 > N_1$ there are more excited atoms than atoms in the ground state: the population is said to be *inverted*. Eq. C.1 in this case indicates a net growth of the number of photons[2].

C.1.1.2 Population Inversion

As just shown the inversion of population is a necessary condition for light amplification in all lasers.
In a two-level system the inversion of population can be never achieved[3]: at least three levels are necessary. We will discuss the case of a four-level system because this is the most common solution implemented in commercial lasers as such as the ones used in our experimental setup, about to be described.

In Figure C.1 is shown the scheme for a four-level system.
A photon of frequency ν_1 excites the electron to jump from the ground state E_1 to the excited state E_4. If the transition probability $W_{4,3}$ is much larger than $W_{4,1}$ and if the state E_4 has a very short lifetime, all the electrons decay almost immediately in E_3.
From E_3 the electrons will decay on E_2 and then back to E_1. If level E_2, like E_4, has a short lifetime while, on the contrary, E_3 is *metastable* level[4], the population on E_3 grows progressively as far as the radiation ν_1 is on.

[1] For the sake of simplicity, at this stage, we neglect the spontaneous emission process.
[2] This growth is exponential but does not exactly correspond to a doubling every generation because the photons are resonant with the two-levels system. Some of the photons are then reabsorbed.
[3] The best one can do with a two-level system is to reach the balanced condition between absorption and stimulated emission
[4] i.e. the atoms in this state are characterized by a very long lifetime

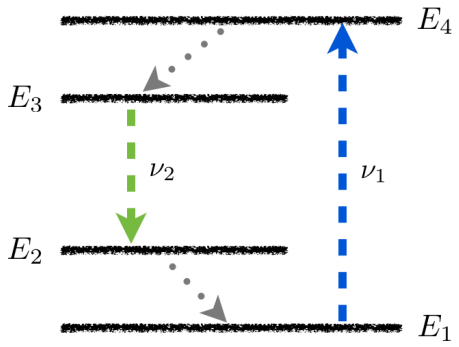

FIGURE C.1: Four-level system for inversion of population: E_4 and E_2 are unstable levels, while E_3 is metastable

The absorption coefficient for the frequency $\nu_2 = (E_3 - E_2)/h$ becomes negative (see Eq.. C.1) and the gain is proportional to the inversion of population.

C.1.1.3 The Resonant Cavity

To sustain lasing action, the gain medium must be placed in an optical cavity. The latter can be defined by two mirrors which provide feedback to the active medium, i.e. photons emitted parallel to the cavity axis are reflected back into the cavity to interact with other excited states. In this way the number of photons will increase geometrically until an equilibrium between excitation and emission is reached.
Both cavity mirrors are coated to reflect the wavelength, or wavelengths, of interest while transmitting the others. One of the mirrors, the output coupler, transmits a fraction of the energy stored within the cavity, and the escaping radiation becomes the output beam of the laser.

The laser oscillates within a narrow range of frequencies around the transition frequency. The width of the frequency distribution, the *linewidth*, and its amplitude depend on the gain medium, its temperature, and the magnitude of the population inversion.
Linewidth is determined by plotting gain as a function of the frequency and measuring the width of the curve where the gain has fallen to one half maximum (FWHM) as shown in Figure C.2 [99].

The output of the laser is discontinuous within this line profile. A standing wave propagates within the optical cavity, and any frequency that satisfies the resonance condition

$$\nu_m = \frac{mc}{2L} \tag{C.2}$$

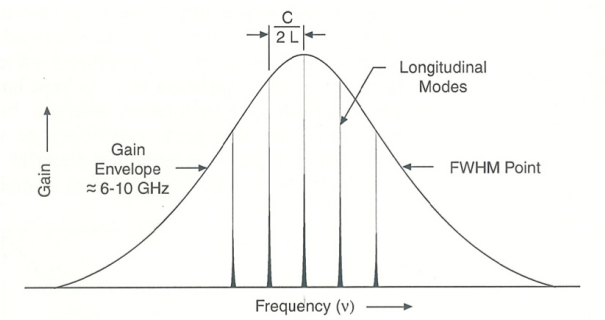

FIGURE C.2: Frequency distribution of longitudinal modes for a single line

will propagates. Here ν_m is the frequency, c is the speed of light, L is the optical cavity length, and m is an integer. Thus, the output of a given line is a set of discrete frequencies, called *longitudinal modes*, that are spaced such that

$$\Delta\nu = \frac{c}{2L} \tag{C.3}$$

C.1.2 Laser Sources in Our Setup

As mentioned before for our proposes, two laser sources are used and are generated by completely different lasers.
The pump beam, employed to excite the chromophore molecules, is generated by a CW laser source based on Ar gas as active media.
The probe beam, triggering the chromophore photodynamics, is a pulsed laser beam arising from a resonant cavity with a crystal of Titanium-Sapphire as the active media. This beam generated in the IR region is then converted to the correct wavelength by means of a frequency doubler crystal.

C.1.3 Pump Source: an Ar CW laser

For the pump beam, triggering the excitation of the chromophore, a continuous wave ion gas laser has been employed. The Argon laser is by far the most employed in the category of the, so called, ion lasers. The active medium is a volume of Argon gas ionized by means of an electrostatic discharge.
The energetic structure of $Ar+$ (see Figure C.4 shows nine different excited levels ($E \approx$ 36eV) and two ground states ($E \approx$ 33eV). Ten different electronic transition are then possible for stimulated emission in this active medium, corresponding to wavelength of

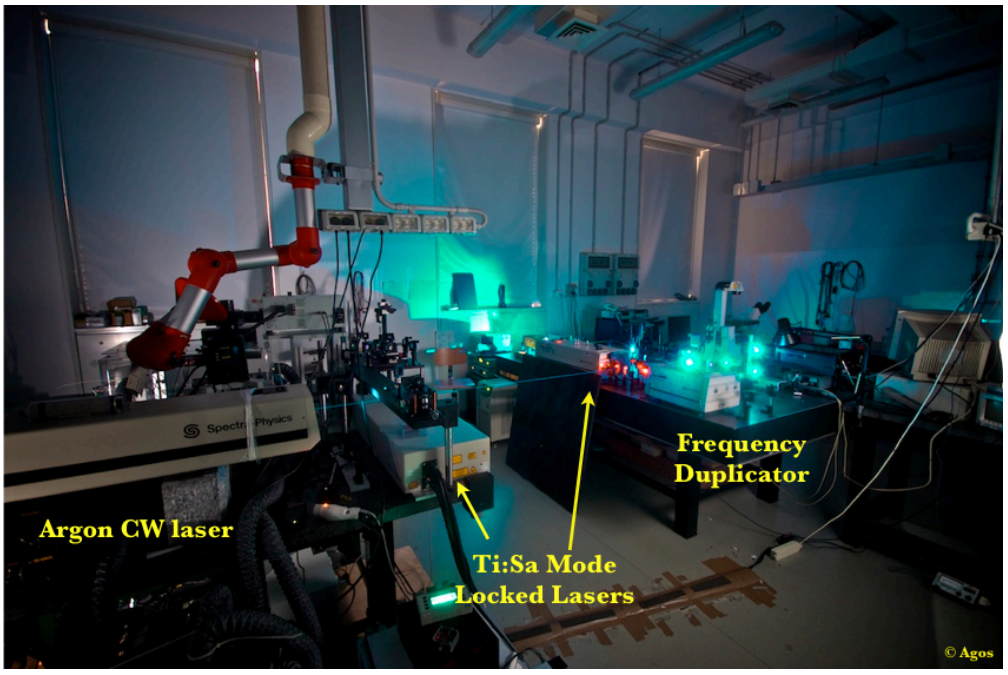

FIGURE C.3: Laser sources at work in the laboratory.

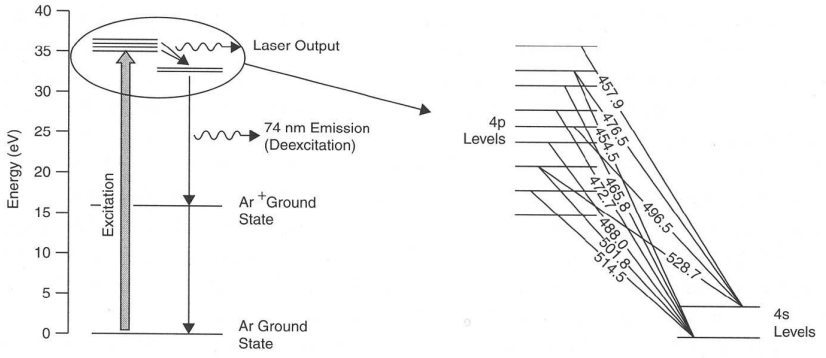

FIGURE C.4: Energy level for ionized Argon gas.

the outgoing radiation comprehended between the ultra-violet and the green[5]. For GFP excitation purposes, the 488nm line suits perfectly.

The effective yield of laser light generation for an *Ar* gas laser is influenced by various factors, the most important of which is the intensity of the electrostatic discharge that has to be high enough to keep the greater part of the gas in the ionized state. For this reason it is extremely important for the laser to be equipped with a extremely powerful cooling device, usually water-based.

In Figure C.5 is reported the internal structure of a typical Argon laser. To be noted are the solenoid (water-cooled) that creates an axial magnetic field in the discharge region,

[5]351.1 nm, 363.8 nm, 454.6 nm, 457.9 nm, 465.8 nm, 476.5 nm, **488.0 nm**, 496.5 nm, 501.7 nm, **514.5 nm**, 528.7 nm. In bold the wavelength with greater yield.

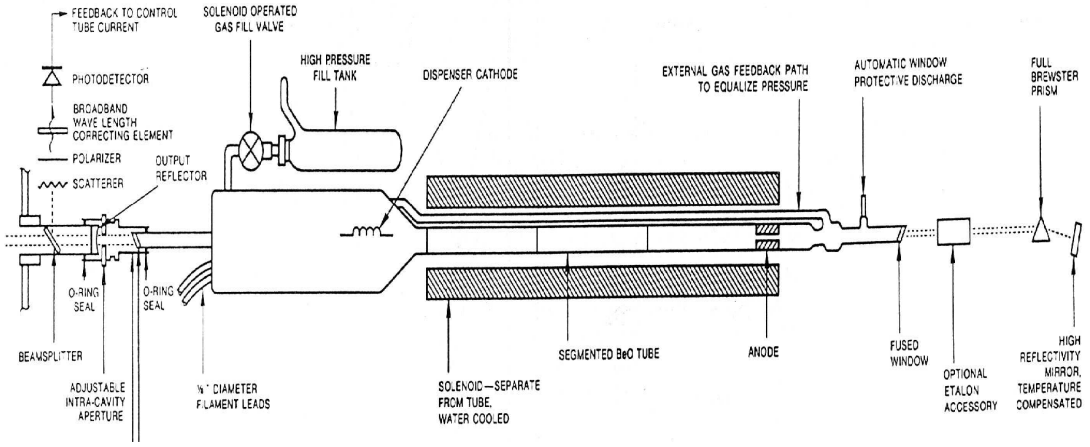

FIGURE C.5: Inside structure of a Argon laser.

in order to localize the $Ar+$ ions along the tube axis, the cathode (larger than the anode) and the system that periodically pumps new argon inside the tube. Finally a prism and a slit allows the output wavelength selection.

C.1.4 Probe Source: a Ti:Sa Resonant Cavity

As previously mentioned, the probe beam generation system consists of a $Ti:Sa$ resonant cavity system. This system, purchased from Spectra Physics, allows the production of a pulsed light beam[6] in the range of wavelength between 690 and 1020nm.

The laser head is made up of the following stages:

- The CW pump laser (engineered following the model of the Spectra Physics' *Millennia*)
- The Titanium-Sapphire resonant cavity (engineered following the model of the Spectra Physics' *Tsunami*)

C.1.4.1 The Pump Laser

The pump laser is based on two diode lasers whose emission is used to pump a solid state laser based on Nd^{3+} ions crystalline matrix doped with yttrium vanadate (Nd:YVO4)[7]. The output wavelength is 1064nm and is converted to a 532nm green beam by means of a second harmonic generation process that takes place in a lithium triborate (LBO) non-linear crystal.
The output is composed by a unique transverse mode (equivalent to the TEM_{00} of a conventional laser) with a pseudo-Gaussian intensity profile characterized by a high ellipticity that has to be corrected before entering the IR mode-locked cavity. This is made by means of a pair of anamorphic prisms mounted to an angle near to the Brewster angle with respect to the incident beam (Figure C.6).

The emission from the diode laser is perfectly superimposed to the absorption band of the Nd^{3+} ion allowing a good coupling between the pump and the active medium (Figure C.7). The active medium, neodymium, has the principal absorption band in the red and near infra-red region of the electromagnetic spectrum.

The generation of the 532nm green pump beam is made by means of the second harmonic generation process that takes place in a LBO crystal. This material is preferred to others with higher non-linear coefficient, because it is possible to optimize the conversion efficiency of LBO simply by varying the working temperature. A dichroic mirror reflects back in the cavity the first harmonic from the solid state laser and allows the 532 nm

[6] the pulsed beam is characterized by a pulse duration of some 100ps, a frequency of repetition $\nu = 80MHz$

[7] This active medium behave as a standard four-levels system described in Section C.1.1.2 and that is the way the light amplification is obtained

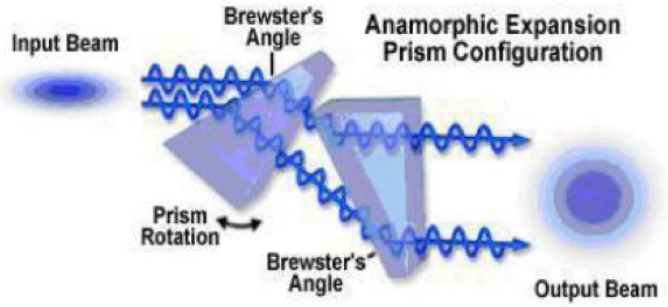

FIGURE C.6: Correction of the beam ellipticity by means of two prism at the Brewster angle.

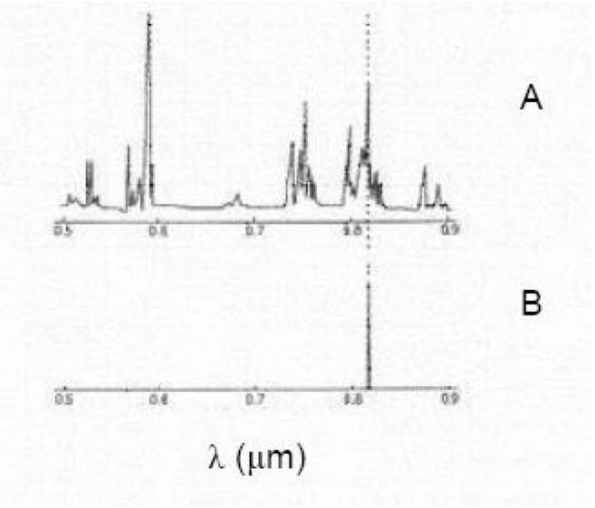

FIGURE C.7: Panel **A**: Absorption spectrum for the Nd^{3+} ion. Panel **B**: Emission spectrum of the diode pump laser.

beam to be sent to the resonant optical cavity.

Since the intensity of the second harmonic radiation depends on the square of the first harmonic power, it is possible to obtain a high conversion efficiency increasing the power of the pump. Unluckily, a solid state laser pumped by a diode laser gives rise to a chaotic emission characterized by high intensity fluctuations preventing its application to scientific experiments. These instabilities are mainly due to the non-linear coupling of the axial modes in the sum frequency (i.e. second harmonic generation) process. In the *Mai-Tai* the problem is overcome by adopting the so called QMAD (Quiet Multi Axial mode Doubling) solution: this employs many axial modes allowing the oscillation of more than 100 longitudinal modes; in this way the power of each axial mode is so low that none of them reaches the peak power needed to induce high non-linear loses. The

non-linear coupling terms are therefore mediated in such way that the second harmonic emission presents a very low noise (Figure C.8). (Caccia[100])

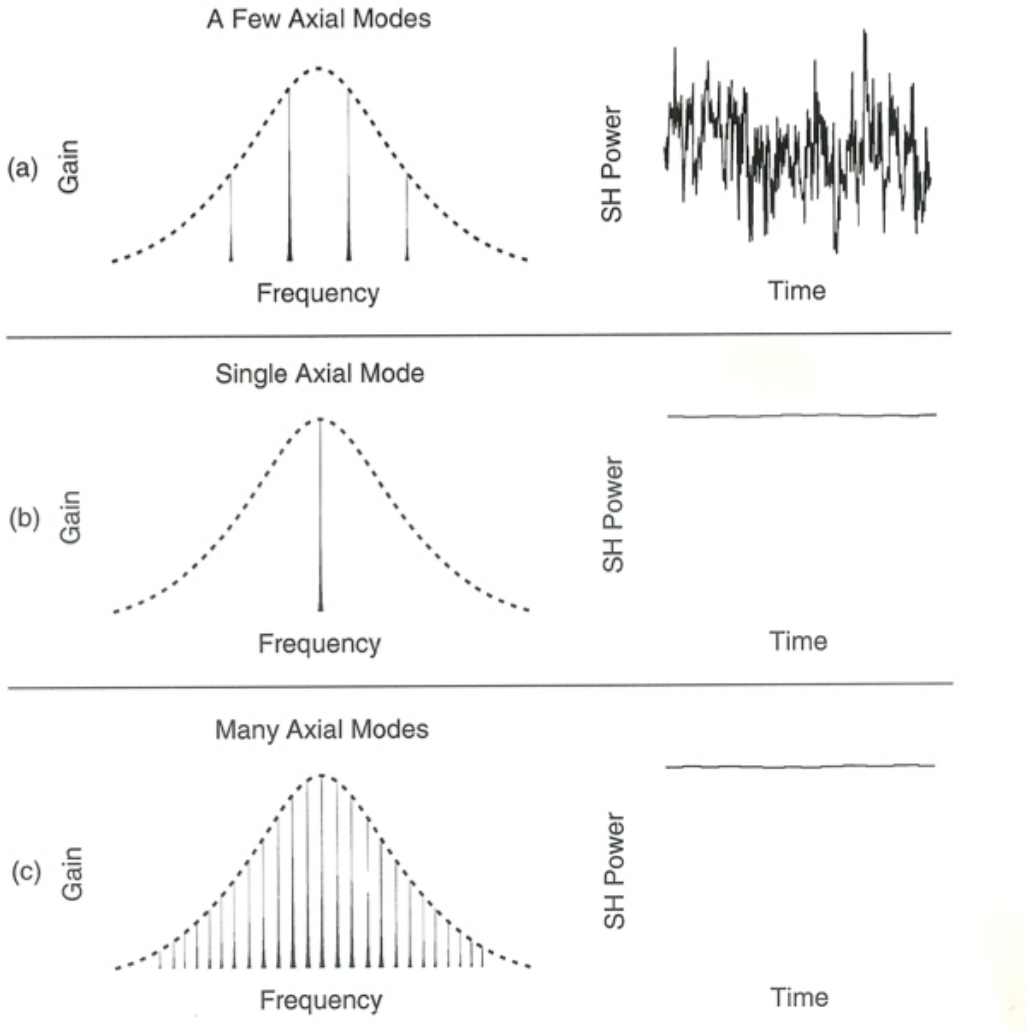

FIGURE C.8: Quiet Multi-Axial mode-Doubling (QMAD). Panel **(a)**: intracavity frequency doubling in a laser with a few axial modes produces large amplitude fluctuations in the second harmonic output resulting from non-linear coupling of the modes through sum frequency mixing. Panel **(b)**: single frequency solution forces oscillation on a single axis mode to eliminate mode coupling. Panel **(c)**: QMAD solution produces oscillation on many axial modes, effectively averaging the non-linear coupling terms to provide highly stable second harmonic output.

C.1.4.2 The Optical Resonant Cavity

The $532nm$ beam from the Nd^{3+} laser is used to pump a Titanium-Sapphire (Ti-Sa) rod that gives rise to the IR output of the laser system. The Ti-Sa is a crystalline solid obtained introducing Ti_2O_3 into a solution of Al_2O_3 allowing the substitution of

a little amount of Al^{3+} ions with Ti^{3+} ions. The Ti^{3+} electronic configuration can be represented as two distinct energy levels with a large broadening caused by the presence of many vibrational levels (Figure C.9). The result is a broadened absorption band between 400 and 600 nm. The fluorescence emission is within 600 and 1000 nm and is due to the fact that the transition occurs between vibrational levels whose energies lie between that of the excited and that of the ground state.

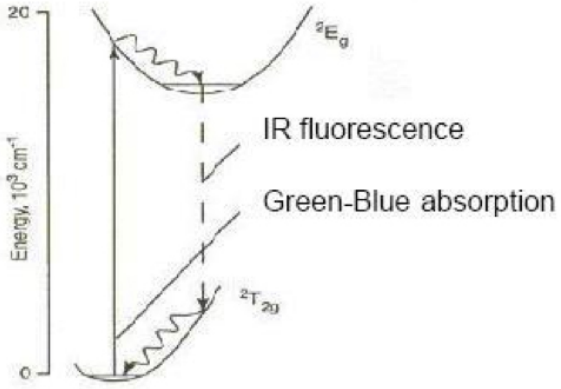

FIGURE C.9: Energy level structure for Ti^{3+} ion in Sapphire.

However coherent laser emission is possible only for wavelengths $\lambda > 670nm$ since for $\lambda < 670nm$ the emission band is superimposed on the absorption band giving rise to auto-absorption processes that reduces the efficiency of the fluorescence emission (Figure C.10).

Wavelength Selection Since the Ti-Sa rod is birefringent, lasing is obtained when the c-axis of the rod is aligned coplanar to the polarization of the electric field in the cavity. The chamber that hosts the rod orients the rod surfaces at Brewster's angle and allows the c-axis to be coplanar to the electric field vector. The output λ is variable within $690 - 1000nm$ by means of a system of four prisms and a slit (Figure C.11). The prisms create a region in the cavity where the different λ are separated and provide also the compensation of the group velocity dispersion. The slit, located in the central part of the four prisms arrangement, allows selection of the desired λ and bandwidth related to the pulse duration of the pulsed output[100].

The Mode-Locking The mode-locked laser is a laser that oscillates in a number N of wavelengths called spectral modes. The electric field inside the laser cavity is described

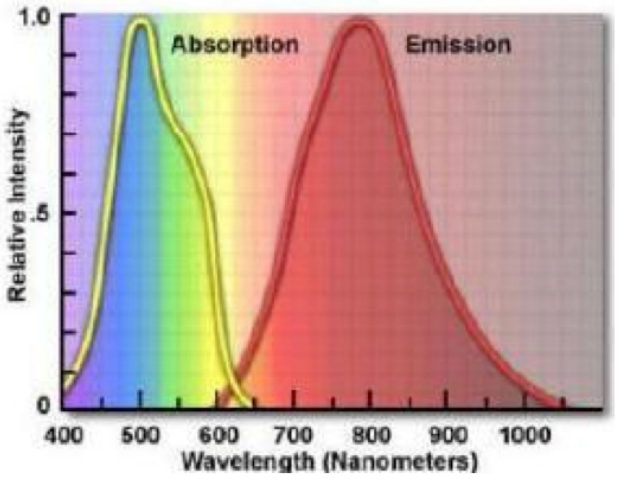

FIGURE C.10: Normalized absorption and emission spectra of Ti-Sa.

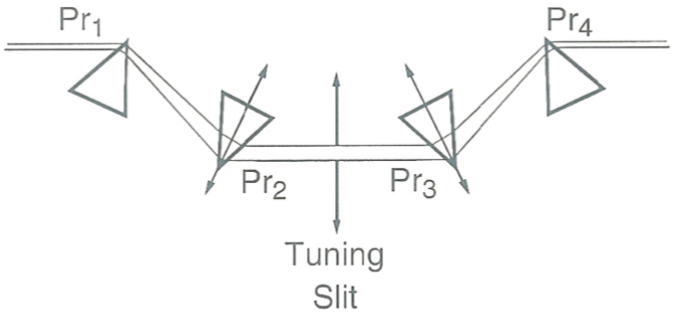

FIGURE C.11: Four prism arrangements and the slit allows to select the wavelength and the bandwidth.

by the equation:

$$E(t) = A \sum_{n=0}^{N-1} e^{i(\omega_n + \delta_n)t} \tag{C.4}$$

where A is the greatest value of the electric field of a single spectral mode, ω_n are the frequencies, that depend on the cavity size L, and δ_n is the phase shift with respect to the nth vibrational normal mode. Usually the output of such system is the incoherent summation of the modes since they do not have correlated phases. In a mode-locked laser the longitudinal modes are forced to stay in phase so that they interfere constructively in some spots of the cavity and destructively in others; in this way it is possible to create a series of single pulses traveling in the cavity. Every time a pulse hits the partial reflective mirror at the end of the cavity the laser has an output.

In this way it is possible to obtain, with frequency $c/2L$, short pulses, whose FWHM is $2L/Nc$ and whose intensity can be demonstrated to be proportional to N^2 and A^2.

FIGURE C.12: Nikon TE300 Microscope

C.2 Focusing Stage

C.2.0.3 Epifluorescence Microscopy

The inverted Nikon TE300 microscope is set in an epifluorescence setup: the same objective that focus the exciting light on the sample, collects the fluorescence signal arising from the sample (see Figure 2.1.
The choice of a single objective is good not only for economic reasons, but also from the experimental point of view (one single focus to be set). The different diffraction, by the objective, between the excitation and the emission light does not cause problem in the image reconstruction. In this setup the exciting light entering the rear of the microscope is deviated towards the objective by the same dichroic mirrors that transmit the emission fluorescence signal in direction of the lateral or frontal output windows where the APD or the CCD camera are respectively positioned.

The Objectives The choice of the objective is very important because it has to provide:

- an appropriate focal length
- a high aperture number

a right choice of these two parameters allows one to work with a very tiny excitation volume ($\approx 0.1\mu m^3$), obtaining at the same time a good yield in collecting the emitted photons.
The numerical aperture is the measure of the solid angle subdued from the objective and gives an estimate of the efficiency of the objective in collecting the light emitted by the sample. It is defined as:

$$\text{N.A.} = n \sin\theta \tag{C.5}$$

where θ is the semi-angle subdued by the last lens of the objective and n is the refractive index of the medium between the objective and the sample.

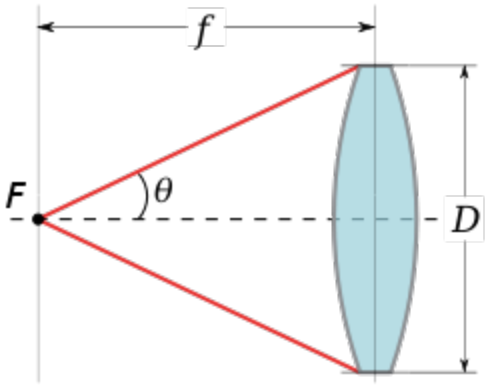

FIGURE C.13: Numerical aperture: N.A. $= n \sin\theta$.

It is necessary to choose a high aperture number because:

- the intensity of the transmitted light is proportional to $(\text{N.A.})^2$
- the maximum resolution is proportional to $(\lambda/\text{N.A.})$

Generally, immersion objectives ensure good performance since the liquid, interposed between the objective and the sample, has a index of refraction very close to that of the glass of the coverslip, the objective and the sample themselves. In this way it is possible to limit reflection and scattering processes of the light[8] [101], [102], [103].

During the work described in the following chapters different objectives were used:

- a water immersion Olympus XLUMPlanFI, M=20X, N.A. = 0.95 and working distance ($\approx 2mm$).

[8] phenomena also known as *index mismatch*.

- a water immersion Nikon Plan Apo, M=60X, N.A. = 1.2 and working distance ($\approx 0.22mm$).
- a oil immersion Nikon Plan Apo, M=100X, N.A. = 1.3 and working distance ($\approx 0.17mm$).

C.3 Signal Acquisition Stage

For detecting the signal, two different devices have been used during the work:

- A **CCD Camera** has been used during setup alignment procedures in order to evaluate the degree of overlap on the sample of the different excitation volumes created by the pump and probe beams.
  This checking was done by putting on the microscope stage a slide with dried up Rodhamine 6G. This chromophore, having a very high absorption coefficient for a broad spectrum of wavelength, emits fluorescence photons we excited with both the pump and probe wavelength. Through the CCD camera it was, then, possible to see the two fluorescence volumes[9] and hence verify their respective overlap.
- For both the FCS measurements and the image acquisitions, the photon count was done via an Avalance PhotoDiode positioned after the confocal pin-hole.

For a complete description of the operating principle of both the detectors we refer to specific literature: for CCD camera see Lasser-Ross et al. [104], [105] and [106], while for the APD see Yagyu et al. [107], [108] and [109].

C.3.1 Image acquisition: Scanning Microscopy

For the purpose of image acquisition a computer software induce a relative motion between the exciting laser beam and the sample, while it reads from the APD the instant photon count and stores it in the i, j matrix element correspondent to the position of the beam on the sample, i.e. the actual imaged pixel.
Being the relative velocity between the beam and the sample much slower than the velocity of light no distortion in the image are induced.

C.3.1.1 Two Possible Setup

There are two possible experimental solution to obtain the movement needed to acquire images.

[9] the shape of this volume is actually the convolution of the excitation volume and the PSF of the optical setup (see Section 2.1.2.

Pietzo This solution, that is the one implemented in our experimental setup; the sample is moved, via pietzo-electric micro motors, along the fixed laser beam.
This solution is cheap and easily homemadable[10], but it presents certain disadvantages such as the slowness of the acquisition and the not completely repeatability of the acquisition. These are due to the natural response time of the pietzo, which limits the scanning frequency to few thousands of pixel per second: the acquisition of a normally large image can take up to several minutes to be completed.

These disadvantages cause **huge** limitations in the application of the Beating Mode developed and presented in this work (see following Chapters)

Galvos The commercial alternative to the pietzo is the galvanometric mirror scanning head: a couple of salvos move the beam on the fixed sample. This solution is certainly faster (also due to the raster pattern path of the beam along the plane of the sample) in terms of acquisition rate and is better in terms of repeatability and adaptability for imaging applications.
For a better description of this solution we refer to Bille and Brown [110], [111], [112], Diaspro et al. [113], [114]

[10] both in terms of setup mounting and software writing

Bibliography

[1] G. Chirico, M. Collini, L. DAlfonso, M. Caccia, **S. C. Daglio**, and B. Campanini. *Green Fluorescent Protein Photodynamics as a Tool for Fluorescence Correlative Studies and Applications*, volume Springer Series in Fluorescence. Springler, 2011.

[2] V. Quercioli, C. Bosisio, **Daglio, S.C.**, F. Rocca, L. D'Alfonso, M. Collini, G. Baldini, G. Chirico, S. Bettati, S. Raboni, et al. Photoinduced Millisecond Switching Kinetics in the GFPMut2 E222Q Mutant. *The Journal of Physical Chemistry B*, 114(13):4664–4677, 2010. ISSN 1520-6106.

[3] **Daglio, S.C.**, N. Banterle, L. D'Alfonso, M. Collini, and G. Chirico. Diffusion-photodynamics coupling in fcs studies of photo-switchable gfp proteins: An analytical and simulative study. *The Journal of Physical Chemistry B*, 2011.

[4] J. Widengren, Ü. Mets, and R. Rigler. Photodynamic properties of green fluorescent proteins investigated by fluorescence correlation spectroscopy. *Chemical Physics*, 250(2):171–186, 1999.

[5] C. Hirlimann. *Laser Basics*, volume Femtosecond Laser Pulses, chapter 1. Springler, 2005.

[6] G.G. Stokes. *On the change of refrangibility of light.* Phil. Trans. R. Soc. London 142: 463-562, 1852.

[7] M. Kasha. Characterization of electronic transition in complex molecules. *Disc. Faraday Soc. 9: 14-19*, 1950.

[8] D.A. Agard, Y. Hiraoka, P. Shaw, and J.W. Sedat. Fluorescence microscopy in three dimensions. *Methods Cell Biol*, 30(353-377):192, 1989.

[9] A. Diaspro, M. Schneider, P. Bianchini, V. Caorsi, D. Mazza, M. Pesce, I. Testa, G. Vicidomini, C. Usai, and A. Bos. Two-photon excitation fluorescence microscopy. *Science of microscopy*, pages 751–789, 2007.

[10] W. Denk, J.P. Strickler, and W.W. Webb. Two-photon laser microscopy, July 23 1991. US Patent 5,034,613.

[11] W. Denk, J.H. Strickler, and W.W. Webb. Two-photon laser scanning fluorescence microscopy. *Science*, 248(4951):73, 1990.

[12] P.T.C. So, C.Y. Dong, B.R. Masters, and K.M. Berland. Two-photon excitation fluorescence microscopy. *Annual Review of Biomedical Engineering*, 2(1):399–429, 2000.

[13] C.Y. Dong, K. Koenig, and P. So. Characterizing point spread functions of two-photon fluorescence microscopy in turbid medium. *Journal of biomedical optics*, 8:450, 2003.

[14] A. Periasamy, P. Skoglund, C. Noakes, and R. Keller. An evaluation of two-photon excitation versus confocal and digital deconvolution fluorescence microscopy imaging in xenopus morphogenesis. *Microscopy research and technique*, 47(3):172–181, 1999.

[15] Alberto Diaspro. *Confocal and Two-Photon Microscopy. Foundations, Applications and Advances*. Wiley-Liss, 2002.

[16] F. Bestvater, E. Spiess, G. Stobrawa, M. Hacker, T. Feurer, T. Porwol, U. Berchner-Pfannschmidt, C. Wotzlaw, and H. Acker. Two-photon fluorescence absorption and emission spectra of dyes relevant for cell imaging. *Journal of microscopy*, 208(2):108–115, 2002.

[17] BR Masters, PTC So, and E. Gratton. Optical biopsy of in vivo human skin: Multi-photon excitation microscopy. *Lasers in medical science*, 13(3):196–203, 1998.

[18] B.R. Masters and P.T.C. So. Confocal microscopy and multi-photon excitation microscopy of human skin in vivo. *Opt. Express*, 8(1):2–10, 2001.

[19] J. Mertz. Molecular photodynamics involved in multi-photon excitation fluorescence microscopy. *The European Physical Journal D-Atomic, Molecular, Optical and Plasma Physics*, 3(1):53–66, 1998.

[20] Eugene Hecht. *Optics*. Addison-Wesley, 3rd edition, 1998.

[21] J.B. Pawley and B.R. Masters. Handbook of biological confocal microscopy. *Journal of Biomedical Optics*, 13:029902, 2008.

[22] D. Magde, E. Elson, and WW Webb. Thermodynamic fluctuations in a reacting systemmeasurement by fluorescence correlation spectroscopy. *Physical Review Letters*, 29(11):705–708, 1972.

[23] M. Ehrenberg and R. Rigler. Rotational brownian motion and fluorescence intensify fluctuations. *Chemical Physics*, 4(3):390–401, 1974.

[24] PF Fahey and WW Webb. Lateral diffusion in phospholipid bilayer membranes and multilamellar liquid crystals. *Biochemistry*, 17(15):3046–3053, 1978.

[25] D.A. Bulseco and D.E. Wolf. Fluorescence correlation spectroscopy: molecular complexing in solution and in living cells. *Methods in cell biology*, 72:465–498, 2003.

[26] J. Widengren, U. Mets, and R. Rigler. Fluorescence correlation spectroscopy of triplet states in solution: a theoretical and experimental study. *The Journal of Physical Chemistry*, 99(36):13368–13379, 1995.

[27] O. Shimomura, F.H. Johnson, and Y. Saiga. Extraction, purification and properties of aequorin, a bioluminescent protein from the luminous hydromedusan, aequorea. *Journal of cellular and comparative physiology*, 59(3):223–239, 1962.

[28] J.G. Morin and JW Hastings. Energy transfer in a bioluminescent system. *Journal of cellular physiology*, 77(3):313–318, 1971.

[29] R.Y. Tsien. The green fluorescent protein. *Annual review of biochemistry*, 67(1): 509–544, 1998.

[30] M. Chalfie, Y. Tu, G. Euskirchen, W.W. Ward, and D.C. Prasher. Green fluorescent protein as a marker for gene expression. *Science*, 263(5148):802, 1994.

[31] R.M. Dickson, A.B. Cubitt, R.Y. Tsien, and WE Moerner. On/off blinking and switching behaviour of single molecules of green fluorescent protein. *Nature*, 388 (6640):355–358, 1997.

[32] G. Jung and A. Zumbusch. Improving autofluorescent proteins: comparative studies of the effective brightness of green fluorescent protein (gfp) mutants. *Microscopy research and technique*, 69(3):175–185, 2006.

[33] F.H.C. Wong, D.S. Banks, A. Abu-Arish, and C. Fradin. A molecular thermometer based on fluorescent protein blinking. *Journal of the American Chemical Society*, 129(34):10302–10303, 2007.

[34] R. Ando, H. Mizuno, and A. Miyawaki. Regulated fast nucleocytoplasmic shuttling observed by reversible protein highlighting. *Science*, 306(5700):1370, 2004.

[35] M. Heilemann, E. Margeat, R. Kasper, M. Sauer, and P. Tinnefeld. Carbocyanine dyes as efficient reversible single-molecule optical switch. *Journal of the American Chemical Society*, 127(11):3801–3806, 2005.

[36] M. Hofmann, C. Eggeling, S. Jakobs, and S.W. Hell. Breaking the diffraction barrier in fluorescence microscopy at low light intensities by using reversibly photoswitchable proteins. *Proceedings of the National Academy of Sciences of the United States of America*, 102(49):17565, 2005.

[37] A.C. Stiel, S. Trowitzsch, G. Weber, M. Andresen, C. Eggeling, S.W. Hell, S. Jakobs, and M.C. Wahl. 1.8 å bright-state structure of the reversibly switchable fluorescent protein dronpa guides the generation of fast switching variants. *Biochemical Journal*, 402(Pt 1):35, 2007.

[38] R. Nifosì and V. Tozzini. Cis-trans photoisomerization of the chromophore in the green fluorescent protein variant e2gfp: A molecular dynamics study. *Chemical physics*, 323(2-3):358–368, 2006.

[39] U. Haupts, S. Maiti, P. Schwille, and W.W. Webb. Dynamics of fluorescence fluctuations in green fluorescent protein observed by fluorescence correlation spectroscopy. *Proceedings of the National Academy of Sciences*, 95(23):13573, 1998.

[40] R. Bizzarri, M. Serresi, S. Luin, and F. Beltram. Green fluorescent protein based ph indicators for in vivo use: a review. *Analytical and Bioanalytical Chemistry*, 393(4):1107–1122, 2009.

[41] M. Andresen, M.C. Wahl, A.C. Stiel, F. Gräter, L.V. Schäfer, S. Trowitzsch, G. Weber, C. Eggeling, H. Grubmüller, S.W. Hell, et al. Structure and mechanism of the reversible photoswitch of a fluorescent protein. *Proceedings of the National Academy of Sciences of the United States of America*, 102(37):13070, 2005.

[42] J. Lippincott-Schwartz and G.H. Patterson. Development and use of fluorescent protein markers in living cells. *Science*, 300(5616):87, 2003.

[43] E. Betzig, G.H. Patterson, R. Sougrat, O.W. Lindwasser, S. Olenych, J.S. Bonifacino, M.W. Davidson, J. Lippincott-Schwartz, and H.F. Hess. Imaging intracellular fluorescent proteins at nanometer resolution. *Science*, 313(5793):1642, 2006.

[44] G. Jung, J. Wiehler, B. Steipe, C. Bräuchle, and A. Zumbusch. Single-molecule microscopy of the green fluorescent protein using simultaneous two-color excitation. *ChemPhysChem*, 2(6):392–396, 2001.

[45] Z. Wang, J.V. Shah, Z. Chen, C.H. Sun, and M.W. Berns. Fluorescence correlation spectroscopy investigation of a gfp mutant-enhanced cyan fluorescent protein and its tubulin fusion in living cells with two-photon excitation. *Journal of Biomedical Optics*, 9:395, 2004.

[46] R. Bizzarri, C. Arcangeli, D. Arosio, F. Ricci, P. Faraci, F. Cardarelli, and F. Beltram. Development of a novel gfp-based ratiometric excitation and emission ph indicator for intracellular studies. *Biophysical journal*, 90(9):3300–3314, 2006.

[47] R.A.G. Cinelli, V. Pellegrini, A. Ferrari, P. Faraci, R. Nifosi, M. Tyagi, M. Giacca, and F. Beltram. Green fluorescent proteins as optically controllable elements in bioelectronics. *Applied Physics Letters*, 79:3353, 2001.

[48] J. Lippincott-Schwartz, N. Altan-Bonnet, GH Patterson, et al. Photobleaching and photoactivation: following protein dynamics in living cells. *Nature cell biology*, page S7, 2003.

[49] M. Andresen, A.C. Stiel, S. Trowitzsch, G. Weber, C. Eggeling, M.C. Wahl, S.W. Hell, and S. Jakobs. Structural basis for reversible photoswitching in dronpa. *Proceedings of the National Academy of Sciences*, 104(32):13005, 2007.

[50] R. Ando, H. Hama, M. Yamamoto-Hino, H. Mizuno, and A. Miyawaki. An optical marker based on the uv-induced green-to-red photoconversion of a fluorescent protein. *Proceedings of the National Academy of Sciences*, 99(20):12651, 2002.

[51] A. Miyawaki, A. Sawano, and T. Kogure. Lighting up cells: labelling proteins with fluorophores. *Nature Cell Biology*, page S1, 2003.

[52] F.V. Subach, G.H. Patterson, S. Manley, J.M. Gillette, J. Lippincott-Schwartz, and V.V. Verkhusha. Photoactivatable mcherry for high-resolution two-color fluorescence microscopy. *Nature methods*, 6(2):153–159, 2009.

[53] J. Lippincott-Schwartz and G.H. Patterson. Photoactivatable fluorescent proteins for diffraction-limited and super-resolution imaging. *Trends in cell biology*, 19(11): 555–565, 2009.

[54] E. Haustein and P. Schwille. Fluorescence correlation spectroscopy: novel variations of an established technique. *Annu. Rev. Biophys. Biomol. Struct.*, 36:151–169, 2007.

[55] O. Griesbeck, G.S. Baird, R.E. Campbell, D.A. Zacharias, and R.Y. Tsien. Reducing the environmental sensitivity of yellow fluorescent protein. *Journal of Biological Chemistry*, 276(31):29188, 2001.

[56] D.F. Reiff, A. Ihring, G. Guerrero, E.Y. Isacoff, M. Joesch, J. Nakai, and A. Borst. In vivo performance of genetically encoded indicators of neural activity in flies. *The Journal of neuroscience*, 25(19):4766–4778, 2005.

[57] A. Paradise, M.K. Levin, G. Korza, and J.H. Carson. Significant proportions of nuclear transport proteins with reduced intracellular mobilities resolved by fluorescence correlation spectroscopy. *Journal of molecular biology*, 365(1):50–65, 2007.

[58] Z. Wang, J.V. Shah, M.W. Berns, and D.W. Cleveland. In vivo quantitative studies of dynamic intracellular processes using fluorescence correlation spectroscopy. *Biophysical journal*, 91(1):343–351, 2006.

[59] M. Chattoraj, B.A. King, G.U. Bublitz, and S.G. Boxer. Ultra-fast excited state dynamics in green fluorescent protein: multiple states and proton transfer. *Proceedings of the National Academy of Sciences*, 93(16):8362, 1996.

[60] H. Lossau, A. Kummer, R. Heinecke, F. Pöllinger-Dammer, C. Kompa, G. Bieser, T. Jonsson, CM Silva, MM Yang, DC Youvan, et al. Time-resolved spectroscopy of wild-type and mutant green fluorescent proteins reveals excited state deprotonation consistent with fluorophore-protein interactions. *Chemical physics*, 213 (1-3):1–16, 1996.

[61] K. Brejc, T.K. Sixma, P.A. Kitts, S.R. Kain, R.Y. Tsien, M. Ormö, and S.J. Remington. Structural basis for dual excitation and photoisomerization of the aequorea victoria green fluorescent protein. *Proceedings of the National Academy of Sciences*, 94(6):2306, 1997.

[62] G. Jung, M. Werner, and M. Schneider. Efficient photoconversion distorts the fluorescence lifetime of gfp in confocal microscopy: a model kinetic study on mutant thr203val. *ChemPhysChem*, 9(13):1867–1874, 2008.

[63] S.T.D. Hsu, G. Blaser, and S.E. Jackson. Cheminform abstract: The folding, stability and conformational dynamics of β-barrel fluorescent proteins. *ChemInform*, 40(51):no–no, 2009.

[64] G. Chirico, F. Cannone, G. Baldini, and A. Diaspro. Two-photon thermal bleaching of single fluorescent molecules. *Biophysical journal*, 84(1):588–598, 2003.

[65] C. Bosisio, V. Quercioli, M. Collini, L. DAlfonso, G. Baldini, S. Bettati, B. Campanini, S. Raboni, and G. Chirico. Protonation and conformational dynamics of gfp mutants by two-photon excitation fluorescence correlation spectroscopy. *The Journal of Physical Chemistry B*, 112(29):8806–8814, 2008.

[66] S. Abbruzzetti, E. Grandi, C. Viappiani, S. Bologna, B. Campanini, S. Raboni, S. Bettati, and A. Mozzarelli. Kinetics of acid-induced spectral changes in the gfpmut2 chromophore. *Journal of the American Chemical Society*, 127(2):626–635, 2005.

[67] R.W. Redmond, I.E. Kochevar, M. Krieg, G. Smith, and W.G. McGimpsey. Excited state relaxation in cyanine dyes: a remarkably efficient reverse intersystem crossing from upper triplet levels. *The Journal of Physical Chemistry A*, 101(15): 2773–2777, 1997.

[68] J. Widengren and C.A.M. Seidel. Manipulation and characterization of photo-induced transient states of merocyanine 540 by fluorescence correlation spectroscopy. *Phys. Chem. Chem. Phys.*, 2(15):3435–3441, 2000.

[69] R. Bizzarri, M. Serresi, F. Cardarelli, S. Abbruzzetti, B. Campanini, C. Viappiani, and F. Beltram. Single amino acid replacement makes aequorea victoria fluorescent proteins reversibly photoswitchable. *Journal of the American Chemical Society*, 132(1):85–95, 2009.

[70] G. Jung, S. Mais, A. Zumbusch, and C. Br
"auchle. The role of dark states in the photodynamics of the green fluorescent protein examined with two-color fluorescence excitation spectroscopy. *The Journal of Physical Chemistry A*, 104(5):873–877, 2000.

[71] G. Jung, C. Br
"auchle, and A. Zumbusch. Two-color fluorescence correlation spectroscopy of one chromophore: Application to the E222Q mutant of the green fluorescent protein. *The Journal of Chemical Physics*, 114:3149, 2001.

[72] G. Jung, J. Wiehler, and A. Zumbusch. The photophysics of green fluorescent protein: influence of the key amino acids at positions 65, 203, and 222. *Biophysical journal*, 88(3):1932–1947, 2005.

[73] G.A. Blab, P.H.M. Lommerse, L. Cognet, G.S. Harms, and T. Schmidt. Two-photon excitation action cross-sections of the autofluorescent proteins. *Chemical Physics Letters*, 350(1):71–77, 2001.

[74] M.A. Albota, C. Xu, and W.W. Webb. Two-photon fluorescence excitation cross sections of biomolecular probes from 690 to 960 nm. *Applied optics*, 37(31):7352–7356, 1998.

[75] C. Eggeling, J. Widengren, R. Rigler, and CAM Seidel. Photobleaching of fluorescent dyes under conditions used for single-molecule detection: evidence of two-step photolysis. *Analytical Chemistry*, 70(13):2651–2659, 1998.

[76] N.S. Cheng. Formula for the viscosity of a glycerol-water mixture. *Industrial & Engineering Chemistry Research*, 47(9):3285–3288, 2008.

[77] T. Ando, T. Meguro, and I. Yamato. Multiple time step Brownian dynamics for long time simulation of biomolecules. *Molecular Simulation*, 29(8):471–478, 2003. ISSN 0892-7022.

[78] D.L. Ermak and JA McCammon. Brownian dynamics with hydrodynamic interactions. *The Journal of chemical physics*, 69:1352, 1978.

[79] M. Doi and SF Edwards. The Theory of Polymer Dynamics (Clarendon, Oxford, 1986). *Bird RB., Hassager O., Armstrong RC and Curtiss CF, Dynamics of Polymeric Liquids*, 1:2.

[80] D.L. Ermak and JA McCammon. Brownian dynamics with hydrodynamic interactions. *The Journal of chemical physics*, 69:1352, 1978.

[81] W.H. Press, S.A. Teukolsky, W.T. Vetterling, and B.P. Flannery. Numerical recipes 3rd edition: The art of scientific computing. 2007.

[82] G. Chirico and J. Langowski. Calculating hydrodynamic properties of DNA through a second-order Brownian dynamics algorithm. *Macromolecules*, 25(2): 769–775, 1992. ISSN 0024-9297.

[83] D.T. Gillespie. Exact stochastic simulation of coupled chemical reactions. *The journal of physical chemistry*, 81(25):2340–2361, 1977.

[84] U. Haupts, S. Maiti, P. Schwille, and W.W. Webb. Dynamics of fluorescence fluctuations in green fluorescent protein observed by fluorescence correlation spectroscopy. *Proceedings of the National Academy of Sciences of the United States of America*, 95(23):13573, 1998.

[85] E. Haustein and P. Schwille. Single-molecule spectroscopic methods. *Current Opinion in Structural Biology*, 14(5):531–540, 2004.

[86] J. Widengren, U. Mets, and R. Rigler. Fluorescence correlation spectroscopy of triplet states in solution: a theoretical and experimental study. *The Journal of Physical Chemistry*, 99(36):13368–13379, 1995.

[87] J. Widengren, U. Mets, and R. Rigler. Fluorescence correlation spectroscopy of triplet states in solution: a theoretical and experimental study. *The Journal of Physical Chemistry*, 99(36):13368–13379, 1995.

[88] J. White and E. Stelzer. Photobleaching gfp reveals protein dynamics inside live cells. *Trends in cell biology*, 9(2):61–65, 1999.

[89] N.C. Shaner, P.A. Steinbach, and R.Y. Tsien. A guide to choosing fluorescent proteins. *Nature Methods*, 2(12):905–909, 2005.

[90] R.J. Leslie, W.M. Saxton, T.J. Mitchison, B. Neighbors, E.D. Salmon, and J.R. McIntosh. Assembly properties of fluorescein-labeled tubulin in vitro before and after fluorescence bleaching. *The Journal of cell biology*, 99(6):2146–2156, 1984.

[91] E.M. Judd, K.R. Ryan, WE Moerner, L. Shapiro, and H.H. McAdams. Fluorescence bleaching reveals asymmetric compartment formation prior to cell division in caulobacter. *Proceedings of the National Academy of Sciences*, 100(14):8235, 2003.

[92] J.R. Lakowicz and B.R. Masters. Principles of fluorescence spectroscopy. *Journal of Biomedical Optics*, 13:029901, 2008.

[93] Y. Garini, A. Gil, I. Bar-Am, D. Cabib, and N. Katzir. Signal to noise analysis of multiple color fluorescence imaging microscopy. *Cytometry*, 35(3):214–226, 1999.

[94] V. Ntziachristos, G. Turner, J. Dunham, S. Windsor, A. Soubret, J. Ripoll, and H.A. Shih. Planar fluorescence imaging using normalized data. *Journal of biomedical optics*, 10:064007, 2005.

[95] SR Aragon and R. Pecora. Fluorescence correlation spectroscopy as a probe of molecular dynamics. *The Journal of Chemical Physics*, 64:1791, 1976.

[96] MV Klein and TE Furtak. Optics Wiley. *New York*, pages 519–522, 1986.

[97] M. Marrocco. Two-Photon Excitation Fluorescence Correlation Spectroscopy of Diffusion for Gaussian- Lorentzian Volumes. *J. Phys. Chem. A*, 112(17):3831–3836, 2008.

[98] Laura Sironi. Studi di polarizzazione di seconda armonica in tessuti biologici. Master's thesis, 2007.

[99] *Mai-Tai Manual*. Spectra Physics.

[100] M. Caccia. *Non-Linear Micro-Spectroscopy of Biological Tissue*. PhD thesis, 2007.

[101] J. Ripoll and M. Nieto-Vesperinas. Index mismatch for diffuse photon density waves at both flat and rough diffuse–diffuse interfaces. *JOSA A*, 16(8):1947–1957, 1999.

[102] A. Diaspro, F. Federici, and M. Robello. Influence of refractive-index mismatch in high-resolution three-dimensional confocal microscopy. *Applied optics*, 41(4): 685–690, 2002.

[103] D. Day and M. Gu. Effects of refractive-index mismatch on three-dimensional optical data-storage density in a two-photon bleaching polymer. *Applied optics*, 37(26):6299–6304, 1998.

[104] N. Lasser-Ross, H. Miyakawa, V. Lev-Ram, S.R. Young, and W.N. Ross. High time resolution fluorescence imaging with a ccd camera. *Journal of neuroscience methods*, 36(2-3):253–261, 1991.

[105] AC Mitchell, JE Wall, JG Murray, and CG Morgan. Measurement of nanosecond time-resolved fluorescence with a directly gated interline ccd camera. *Journal of microscopy*, 206(3):233–238, 2002.

[106] M. Straub and SW Hell. Fluorescence lifetime three-dimensional microscopy with picosecond precision using a multifocal multiphoton microscope. *Applied physics letters*, 73:1769, 1998.

[107] E. Yagyu, E. Ishimura, and M. Nakaji. Avalanche photo diode, May 18 2005. US Patent App. 11/914,871.

[108] E. YAGYU, E.M.D.K.K. ISHIMURA, M.M.D.K.K. NAKAJI, et al. Avalanche photo diode, March 12 2008. EP Patent 1,898,471.

[109] M.R. Bruce, V.J. Bruce, J.D. Birdsley, R.M. Ring, R.R. Goruganthu, and B.V. Davis. Quadrant avalanche photodiode time-resolved detection, November 19 2002. US Patent 6,483,327.

[110] J.F. Bille and S.I. Brown. 3-dimensional laser beam guidance system, February 20 1990. US Patent 4,901,718.

[111] I. Sawamura, M. Aihara, K. Nakamura, and Y. Kondo. Fluorescence determining microscope utilizing laser light, August 18 1981. US Patent 4,284,897.

[112] R.C. Kain. Fluorescence imaging system employing a macro scanning objective, February 17 1998. US Patent 5,719,391.

[113] A. Diaspro, M. Corosu, P. Ramoino, M. Robello, et al. Adapting a compact confocal microscope system to a two-photon excitation fluorescence imaging architecture. *Microscopy research and technique*, 47(3):196–205, 1999.

[114] R.C. Kain. Fluoresecence imaging system, September 30 1997. US Patent 5,672,880.

Acknowledgements

The writing of this thesis marks the definitive end of the *educational* part of my life. It is actually impossible for me to be able to thank every person that I felt, or actually was, important for my life, my career and my personal development, in these years. Some of those will be deliberately dodged for more than a reason, not last the space availability...
For the lucky ones, knowing me, they will know that any trace of irony will be the sign that this acknowledgments are sincere and absolutely non rhetorical.

Giberto Chirico was my advisor and doctorate coordinator. He, **Maddalena Collini** and **Laura D'Alfonso**, were all of great help for my PhD work, also showing me full support, in the last year and half, to bring this work to an end.

Talking about undergrads I worked with, the first huge *thank you* must be for **Cecco** *the Wall* **Rocca**, simply the best man for the job! Working with him has been so much funny, stimulating and surely never boring. I really miss the hours spent with him in the laboratory building equipments, making stuff work and throwing things around. Toward him, probably because none of us has the faintest idea what it is like, I felt the closest thing to a brotherhood I've ever felt with anyone...
Niccoló Banterle has been a precious help in the theoretical and simulative part of the work. I'm real proud of the fine job we did together on the GFP photoactive modeling; I taught him some simulative tricks while he (re)taught me some math...
What to say about **Agostino Carandente**?? Not only he was my friend before becoming my *assistant*, but his support and competence as a *computer scientist* were simply invaluable for my work. Alone, I would have not been able to develop such a fine software for the B.M. raw data analysis. He is the living proof that also crazy girls may, sometimes, be useful...
Last but certainly not least **Sara** *Sarétta* **Carozza**. She inherited my experimental activity for her master thesis and she was quite helpful to me too for the conclusion of this work. The calculation of the divergency of chaos[11] around her volume would certainly diverge, but that's why she is who she is...

In the vortex of people and madness that is the LABS[12], I feel the need to thank someone in particular.
Stefano Freddi, thanks for having been my desk mate for over two years and for having shared with me numberless jokes and most of the road trips...
Syrons, really, no words, in any language, can be found about you: thank you! :P

[11] She will always be remembered by Ago and me for her *Eh!! Giá fatto!* that enlightened our afternoon :P
[12] Laboratory of Advanced BioSpectroscopy

Michele Caccia, working with you was very funny: I will always remember you for your cynicism, I'll never be able to match and your secret poetic production...
Alberto Lombardini, we worked together only briefly, but I was really impressed by your interest and dedication in what we were doing...
Margaux Bouzin, it was probably due to your venetian heritages that you always considered my jokes as they were intended. I deeply respect the fact the you never took offense at my bastardness.
All of those[13], whom are not directly addressed, it is not because they don't matter: it is just a mere question of space and timing. To you, Unknown Soldier of my Bicocca life: thank you!

I also feel the sincere need to thank my *new* colleagues at ST. **Enrico** welcomed me in his group and showed me full support for the completion of this work. **Silvia**, **Davide**, **Daniela**, **Gianluca**, **Nicoletta** (or was it Stefania...) and **Marta** contribute to form the be*st* environment I've ever worked in. Each one of them combines in him/herself an extraordinary sense of humor, a keen intelligence and an extraordinary skill set in the noble art of the *supercazzola*. It gives me real pleasure to work with them and if I wake up every morning, eager to go to work, they certainly have to be accounted responsible!

Talking about the non-professional sphere, **Doraz** deserves the first thank you for being my oldest friend, still enduring in the task against all odds... He still is the best unintended entertainer ever :D

Bard, **Birdack** and **Giak**, even if life is carrying us on separate paths, I know that you'll always be there for a beer and a talk, resuming exactly from where we left, with no awkwardness nor embarrassment. Moreover, we'll always have *il nostro paradiso su misura*...
Alberto and your always dark mood, I'll make a matter of pride to find the right wavelength to switch you on a brighter state.. But please... cooperate a little!!! :D
Cecilia, thanks for being my best[14] model for photo shootings, actually posing when asked to! :D
Camilla and **Carmen**, the great deal of our friendship is that I don't actually need to say you anything: so I won't :D...

If I have to say, right now in this moment, who is my dearest friend, I'd say that it ain't fair as a choice, but then I would certainly say you, **Giulia**, with your way of making you feel close even if 800 km away... I'm really thankful for your being here or there or whatever...

[13] And it'a really a lot of people!
[14] And to be fair, with the Doraz, the only

Quasi nel finale vorrei ringraziare una persona che non c'é piú. Se ci fosse ancora sono sicuro che, anche senza capire nulla di quello che ho scritto e anche senza lasciarsi troppo intortare sulla vera necessitá del traguardo (*e adess' che te ghee el duturat, se'l cambia?*), sarebbe stato contento e basta! Con lui ho i piú bei ricordi di bambino e ragazzo, e, a modo suo (o forse mio), riesce ancora a mancarmi in maniera sorda ma continua...

Being parents can[15] certainly be an ungrateful job: no matter how hard you try, you'll always seem to find something you've done wrong, but still there are also plenty of things that my **mum** and **dad** had got right!! I'm not really sure in what range it falls, but I, sure as hell, owe to them the work ethics and the fear of boredom, that[16] merges in a target-orientated mind and the constant search for new challenges and new things to learn...

Kira simply was always there with me, in the good and in the bad that happened to me in the last 11 years, with the kind of tenderness that only a dog can give you. I won't spend any more words, she'll surely refuse to read, I touch her nose with mine and I'll keep enjoying every new moment I get to spend with her...

Elena, what can I say to you? I love you. Simply as that, and I can't stop doing that, no matter how mad you are actually able to drive me sometimes :P.
The more I am with you, the more I look forward for more: I really hope we will have some kind of (possibly long) future together.

Quello che io ora provo per quell'uomo é una comprensione diretta, senza impegno, senza ideologie sociali. Attraverso quest'uomo li posso vedere tutti. Nessuno sa quello che fa, nessuno sa quello che vuole, nessuno sa quello che sa.
Intelligenti, stupidi... che differenza c'é?... Vecchi, giovani... certo, tutti della stessa etá. Uomini, donne... Che vuoi che conti?... Tentativi di persone che comunque... esistono.
Si, quell'uomo é tutto. Bisognerebbe essere capaci di trovare... la consapevolezza e l'amore che dovrebbe avere un Dio che guarda.

- Giorgio Gaber [Il Grigio, 1990]

Stefano C. Daglio, Settimo Milanese, 2012

[15] But should not!
[16] when doesn't border in anxiety :P